POLYETHER AMIDE MIXED MATRIX MEMBRANES CONTAINING SULFONATED GRAPHENE OXIDE FOR AIR- DEHUMIDIFICATION

A Thesis

by

ABDUL REHMAN

Submitted to the Graduate and Professional School of
Texas A&M University
in partial fulfillment of the requirements for the degree of
MASTER OF SCIENCE

Chair of Committee,	Ahmed Abdala
Committee Members,	Ioannis Economou
	Mohammed Al-Hashimi
Head of Department,	Patrick Linke

December 2021

Major Subject: Chemical Engineering

ABSTRACT

An increase in demand for air-conditioning is evident due to the rise in global temperatures through the advent of global warming, coupled with Earth's growing population. An estimation of about 65% of the worldwide population in 2050 will require an air conditioner for the comfort of life and survival. Current air conditions are too energy and resource extensive. Membrane-based air-dehumidification air-cooling has been proposed as a solution in the form of disruptive technology. The importance of the membrane in membrane-based air-dehumidification air-cooling cannot be understated. Therefore, the thesis aims to fabricate novel membranes incorporating nanofillers. In this thesis, polyether block amide (Pebax) membranes are manufactured in freestanding and supported membranes. Pebax has shown good performance in gas separation, especially water permeance. However, the restraints of the transport properties remain. Sulfonated GO (SGO) was targeted as the nanofiller of choice to be incorporated into the Pebax-MMM and supported Pebax membranes. The supported membranes are supported on an ultrafiltration PES membrane and its MMM containing SGO. The synthesis of SGO occurs with the grafting of sulfanilic salt on GO with oxygen-based functional groups, which was synthesized using Tour’s method. GO and SGO was characterized by wettability, crystal structure, and elemental analysis to incorporate the best performing nanofiller in the mixed matrix membranes. SGO retained a contact angle of 26°, making it an ideal candidate for a nanofiller in water/nitrogen separation. The support of PES membranes was fabricated incorporating SGO at 0.05, 0.10, 0.20, and 0.40 wt.% loadings, and they were characterized to determine the most favorable support. PES-0.2%SGO showed the lowest contact angle in relation to the loading amount with a water contact angle of 60.6°, a 10° decrease from 70.6° attained from the PES control membrane. The supported Pebax membrane used the PES-0.2%SGO support. The N_2 permeance was measured to study the effect of the number of coating layers, the substrate type, and the thickness of the active layer. The substrates used to fabricate the active Pebax layer were 0.5 wt.% Pebax and 0.5 wt.% Pebax-0.5%SGO-0.5%SGO. These membranes were characterized by studies regarding wettability, topography, and surface imaging—the active layer of each coat of 0.5 wt.% Pebax yielded around 200 nm, with a surface roughness of 11 and 12 nm for the coating substrates of 0.5 wt.% Pebax and 0.5 wt.% Pebax-0.5 wt.% SGO. Furthermore, freestanding Pebax membranes incorporating SGO in a mixed matrix were fabricated and characterized with wettability, topography, and surface imaging, where the incorporation of SGO in the 12 µm thick membranes resulted in a twice fold increase in average roughness to 18 nm with a 2° decrease in the contact angle to 72°. In the nitrogen permeance performance tests, asymmetric Pebax membranes were governed by the active layer coating thickness. One layer of coats (200 nm) gave N_2 permeance of 84 GPU, and the 2 layers membrane (400 nm) gave 34 GPU. In contrast, the free-standing Pebax membranes permeance increased five-fold from 176 GPU to 555 GPU with 0.5 wt.% SGO.

DEDICATION

This thesis is dedicated to my parents. Without their unconditional love, consistent support, and everlasting prayers, none of this would have been possible.

ACKNOWLEDGEMENTS

At first, I would like to acknowledge my committee chair, Dr. Ahmed Abdalla for his continuous support, guidance, and everlasting patience with my research work for my thesis. His role as a supervisor was critical in the growth I have had as a person and as a researcher during my time.

In addition to Dr. Abdalla, I would like to thank the rest of my committee membranes, Dr. Ioannis Economou and Dr. Mohammed Al-Hashimi for their insightful comments, inspiration, and encouragement.

In addition, I would like to thank Dr. Kasim Yiming Wubulikasimu at the Central Materials Facility at TAMUQ for his patience and effort contributed by training and running multiple analysis for all the characterization studies carried out in this thesis.

Furthermore, I would like to thank my research group for the rest of the research group for their cooperation and understanding during my time there. Although I would like to thank Ms. Omnya Abdalla especially, who guided me in countless situations whilst I was carrying on my practical lab work.

I would also like to thank all the TAMUQ staff and faculty, as well as my peers for consistently being an endless source of support and encouragement which has led me to where I am.

I would like to thank my siblings, Amad Ur Rehman, Qirrat Habib, Anum Ashraf & Usama Khalid, for their constant support and encouragement, with the help my niece Ranya and nephews Eesa & Ismail, their constant reassurances in tough times have been a great support for me to carry on and have enabled me to attain my goals. Next, I would

like to thank my wife, Ayman Arif, for her love and support throughout the numerous years have been a source of energy and inspiration. She has always helped me to see the bigger picture in attaining future goals and has always pushed me to do my best. Furthermore, I would like to acknowledge my parents, Habib Ur Rehman and Kausar, for their unconditional love, support, and prayers. For without their unwavering belief in me and their constant support has led me to attain my goals.

Lastly, I would like to thank God, for his countless blessings that he has bestowed on me, regardless of how ungrateful I have been. For indeed, he is the most merciful, the most compassionate.

FUNDING SOURCES AND CONTRIBUTORS

Funding Sources

The project for developing novel air-dehumidification membranes was funded by the Qatar National Research Fund (QNRF) in Qatar Foundation through the National Priorities Research Program (NPRP12S-0128-190016.)

Contributors

This thesis was supervised by a committee consisting of Dr. Ahmed Abdala as chair and Dr. Ioannis Economou as a committee member from the Department of Chemical Engineering, and Dr. Mohammed Al-Hashimi as the external committee member from the Department of Chemistry. All characterization tests and lab analysis were done at the technological facilities present at Texas A&M University at Qatar, namely, X-ray Photoelectron Spectroscopy (XPS), Energy Dispersive X-ray Spectroscopy (EDAX), Scanning Electron Microscopy (SEM), X-Ray Diffraction (XRD), Atomic Force Microscopy (AFM), Contact Angle and Nitrogen Permeance testing.

NOMENCLATURE

2D	Two Dimensional
3D	Three Dimensional
AFM	Atomic Force Microscopy
CA	Contact Angle
DI	Deionized water
EDS	Energy Dispersive Spectroscopy
f-GO	Functionalized Graphene Oxide
GO	Graphene Oxide (GO)
HCl	Hydrochloric Acid
MMM	Mixed Matrix Membrane(s)
NF	Nanofiltration
PES	Polyether sulfone
Pebax	Polyether block amide
PS	Polysulfone
PVDF	Poly (vinylidene fluoride)
PVP	Polyvinylpyrrolidone
RSQ/R_q	Mean root-square
R_{max}	Maximum Roughness
SEM	Scanning Electron Microscopy
SGO	Sulfonated Graphene Oxide
SRGO	Sulfonated Reduced Graphene Oxide

TEM	Transmission Electron Microscopy
UF	Ultrafiltration
XPS	X-ray Photoelectron Spectroscopy
XRD	X-ray Diffraction

TABLE OF CONTENTS

ABSTRACT ii

DEDICATION iv

ACKNOWLEDGEMENTS v

FUNDING SOURCES AND CONTRIBUTORS vii

NOMENCLATURE viii

1. Introduction 1

2. Literature Review 10

  2.1 Membrane-Based Air-Dehumidification for Air Cooling 10

  2.2 Liquid Desiccant Air-Dehumidification Cooling 11

    2.2.1 Proton Electrolyte Membrane Based Air-Dehumidification Cooling 13

    2.2.2 Vacuum Based Air-Dehumidification Cooling 14

  2.3 Introduction to Gas Separation Membranes 16

    2.3.1 Gas Separation Membranes 16

  2.4 Membrane Materials 18

    2.4.1 Metal Membranes 18

    2.4.2 Ceramic Membranes 19

    2.4.3 Polymeric Membranes 19

    2.4.4 Metal-Organic Framework-based Membranes 20

2.5 Membrane Fabrication Techniques 21

2.6 Air-Dehumidification Membranes 25

  2.6.1 Inorganic Membranes 26

  2.6.2 Organic Membranes 27

  2.6.3 Organic-Inorganic Hybrid Membranes 33

2.7 Polyether amide Membranes 37

2.8 Graphene-Based Membranes 43

2.9 Graphene Oxide (GO) 47

  2.9.1 Synthesis of GO 48

  2.9.2 Functionalization of GO 50

  2.9.3 Sulfonation of GO 50

  2.9.4 Amine functionalization of GO 54

2.10 Conclusions 56

3. Research Objectives and Methodology 58

3.1 Research Objectives 58

3.2 Research Methodology 58

3.3 Materials 59

3.4 Synthesis of GO 59

3.5 Functionalization of GO 60

3.6 Material Characterization 61
  3.6.1 Crystal Structure of GO....61
  3.6.2 Elemental Analysis of GO....62
  3.6.3 Surface and Cross-Sectional Imaging 63
3.7 Fabrication of PES Mixed Matrix Membranes....63
3.8 Fabrication of Free Standing and Supported Pebax Membranes 64
  3.8.1 Fabrication of Free Standing Pebax Membranes 64
  3.8.2 Fabrication of Asymmetric Pebax Membranes....65
3.9 Membrane Characterization 66
  3.9.1 Membrane hydrophilicity and wettability 67
  3.9.2 Membrane Topography and Surface Roughness....67
3.10 Performance Testing....67
  3.10.1 Water Permeance and Selectivity....67
  3.10.2 Nitrogen Permeance 69
4. Results and Discussion....70
4.1 Characterization of GO and Functionalization of GO....70
  4.1.1 Elemental and Chemical Composition Analysis....70
  4.1.2 Crystal Structure of GO and f-GO 73
  4.1.3 Wettability Analysis....75

4.2 The Effect of Sulfonated GO on PES Mixed Matrix Membranes 77
  4.2.1 Surface and Cross-Sectional Imaging 77
  4.2.2 Topography and Roughness 78
  4.2.3 Wettability 80
4.3 Characterization of Free-Standing Pebax Membranes 82
  4.3.1 Surface and Cross-Sectional Imaging 82
  4.3.2 Topography and Roughness 84
  4.3.3 Wettability 86
4.4 Characterization of Asymmetric Pebax Membranes Supported on PES-SGO MMM 87
  4.4.1 Cross-sectional Imaging 87
  4.4.2 Topography and Roughness 88
  4.4.3 Wettability 91
4.5 Performance Testing 93
5. Conclusions and Future Recommendations 98
5.1 Conclusions 98
5.2 Recommendation and Future Work 101
6. References 102

LIST OF FIGURES

Figure 1 - Reproduced air dehumidification air-cooling process as per Calridge-Culp-Liu's patent [8] 3

Figure 2 - Psychometric chart comparison showing the pathway of conventional air-cooling processes compared to a novel vacuum membrane-based process, adapted from Culp [8] 4

Figure 3 - Flat sheet membrane module displaying each part adapted from Ham et [9] ... 6

Figure 4 - Liquid desiccant assisted membrane-based air-dehumidification in a) parallel plates and b) HF membranes adapted from Chen et al. [22] 12

Figure 5 - Schematic of proton electrolyte membrane air-dehumidification adapted from Qi et al. [25] 14

Figure 6 - Energy efficient dehumidification using vacuum pump - patented by Culp [8]. 15

Figure 7 - Interfacial polymerization of a polysulfone membrane to fabricate a thin film composite membrane [49] 23

Figure 8 - Fabrication of a) flat sheet and b) hollow fiber membranes through non-solvent induced phase inversion (NIPS) [55] 25

Figure 9 - PDMS/PAN HF membrane composition [60] 29

Figure 10 - PDMS/PAN HF membrane performance with varying relative humidity and sweep flow rate [60] 29

Figure 11 - Permeance and selectivity of TFV-HF at varying treatment times [61] 31

Figure 12 - PES/PVA TFC surface morphology captured by SEM [62] 32

Figure 13 - Zeolite crystal growth on porous nickel support SEM image [65]................33

Figure 14 - Cross-section imaging of hollow HZIF-8 membrane [17]............................34

Figure 15 - Selectivity and water permeability performance of commercial polymer adapted from Sijbesma et al. [20]..38

Figure 16 - Effect of PEG-POSS in Pebax matric for carbon dioxide separation [71]....39

Figure 17 - AFM analysis for roughness on a&b) 3D and 2D scans on pristine Pebax, c&d) 3D and 2D scans on 30 wt.% PEG-POSS/Pebax MMM [71]...40

Figure 18 - Permeability of carbon dioxide with the loading of various nanoparticles [72] 41

Figure 19 - Cross-section imaging of Pebax mixed matrix membranes with 2, 4, 6 & 8 wt.% loading [72]..42

Figure 20 - Schematic drawing of GO dispersion on porous anodic aluminum oxide via spin coating [74]...43

Figure 21 - Cross-sectional imaging via SEM of GO spin-coated membrane on porous aluminum oxide..44

Figure 22 - Nanomaterial filler concentration of GO and TiO_2 in the membrane impacting water permeance [67]...45

Figure 23: Effect of GO loading on permeance and water/nitrogen selectivity in single and five layers GO coating [75]..46

Figure 24 – High-resolution C1s and O1s scans of successfully synthesized GO [76]...49

Figure 25 - Size of GO sheets produced by A) Hummer's Method B) Modified Hummer's Method and C) Improved Hummer's Method (Tour's) [83]..49

Figure 26 - Grafting of sulfanilic diazonium salt on GO adapted from Oger [76] 51

Figure 27 - Typical XRD result for GO, Functionalized GO, and Graphite [76] 54

Figure 28 - Chemical Reaction of GO Reaction to form Amine-Functionalized GO, adapted from Naser et al. [89] 55

Figure 29 - Flow diagram of research methodology 59

Figure 30 - Simplified process diagram of sulfonation of GO 61

Figure 31 - Simplified process of making PES membrane. 64

Figure 32 - Process diagram of applying Pebax 1074 on PES support to produce the TFC membrane. 66

Figure 33 - Vacuum-Dehumidification set up flow diagram adapted from Bui et al [11] 68

Figure 34 - Carbon and Oxygen high-resolution XPS scan deconvoluted for GO 71

Figure 35 - Carbon, Oxygen, Nitrogen, and Sulfur high-resolution XPS scans deconvoluted for sulfonated GO 73

Figure 36 - XRD analysis on GO, sulfonated, and sulfonated reduced GO 74

Figure 37 - Contact angle analysis for variants of GO 76

Figure 38 - Contact angle imaging of GO and functionalized GO variants 77

Figure 39 – Surface SEM imaging of PES mixed matrix membranes containing a) PES Control, b) 0.05 wt.% SGO, c) 0.10 wt.% SGO, d) 0.20 wt.% SGO and e) 0.40 wt.% SGO 77

Figure 40 - Cross section SEM imaging of PES mixed matrix membranes containing a) PES control, b) 0.05 wt.% SGO, c) 0.10 wt.% SGO, d) 0.20 wt.% SGO and e) 0.40 wt.%

SGO 78

Figure 41 - 3D AFM imaging of PES mixed matrix membranes including a) PES control, b) 0.05 wt.% SGO, c) 0.10 wt.% SGO, d) 0.20 wt.% SGO and e) 0.40 wt.% SGO........79

Figure 42 - AFM of polyether sulfone mixed matrix membranes 79

Figure 43 - Contact angle analysis graph for PES mixed matrix membranes.................81

Figure 44 - Contact angle analysis imaging for PES mixed including a) PES Control, b) 0.05 wt.% SGO, c) 0.10 wt.% SGO, d) 0.20 wt.% SGO and e) 0.40 wt.% SGO 82

Figure 45 – SEM surface images of the free-standing Pebax membranes.......................83

Figure 46 - Cross-sectional imaging of free-standing Pebax membranes........................84

Figure 47 - Topography of a) free standing Pebax membrane and b) 0.5wt% SGO-Pebax MMM 85

Figure 48 - AFM analysis data for free standing Pebax membranes 86

Figure 49 - Contact angle data of Pebax and SGO-Pebax free-standing membranes......87

Figure 50 - Cross-section SEM of a) PES coated using 0.5 wt.% Pebax with b) one coating layer and c) two coating layers...88

Figure 51: 3D AFM image of a) PES support, coated twice with b) 0.5 wt.% Pebax and c) 0.5 wt.% Pebax-0.5%SGO on PES and d) PES-0.20 sGO coated with twice with e) 0.5 wt.% and f) 0.5 wt.% Pebax-0.5%SGO 89

Figure 52 - AFM roughness analysis for Pebax supported membranes with active layers fabricated with different coatings methods on PES 90

Figure 53 - AFM roughness analysis for Pebax supported membranes with active layers fabricated with different coatings methods on PES-0.2SGO MMM 91

Figure 54 - Contact angle imaging of supported Pebax membranes fabricated on a) PES Control support with coatings of 0.5 wt.% Pebax and 2x 0.5 wt.% Pebax (b,c) and on a PES-0.2%SGO support d), coated with 0.5 wt.% Pebax and 2x 0.5 wt.% Pebax (e,f)....92

Figure 55 - Contact angle data for asymmetric Pebax membranes..................................93

Figure 56 - Nitrogen permeance performance testing for PES-SGO MMM 94

Figure 57 - Nitrogen permeance on asymmetric Pebax membranes on PES Control support 95

Figure 58 - Nitrogen permeance on asymmetric Pebax membranes on PES-0.2%SGO support..96

Figure 59 - Nitrogen permeance on free-standing Pebax and its mixed matrix membrane 97

LIST OF TABLES

Table 1 – Summary table for liquid desiccant assisted membrane air-dehumidification module performance. 13

Table 2 – Performance of vacuum Based-Air dehumidification cooling modules 15

Table 3 - Commercial manufacturers and membrane materials used [29]....................... 17

Table 4 – Performance of organic air-dehumidification membrane 32

Table 5 - Organic-inorganic hybrid air-dehumidification membrane summary table 36

Table 6 - Polyether and polyamide content in various grades of breathable Pebax......... 37

Table 7 - Summary table of polyether amide membranes used for gas separation.......... 42

Table 8 - Graphene-based air-dehumidification membranes summary table. 47

Table 9 - Atomic Composition of GO, SRGO, SGO determined by EDAX 71

Table 10: The crystal structure parameters for GO and f-GO.. 75

CHAPTER I

1. Introduction

The population on our planet is increasing rapidly and is estimated to grow up to 9.74 billion by 2050. due to global warming, the earth's average temperature is expected to increase by at least 1.5 °C [1], which is predicted to increase demand for energy and space cooling requirements for survival and comfort. Moreover, two-third of the global population is expected to require access to air conditioning by 2050, as reported by the International Energy Agency, stressing the global electricity demand and necessitating an imminent solution [2]. On average, cooling devices such as traditional air conditioning systems and electrical fans consume 10% of the global electrical demand [2]. The targeted optimum room temperature for cooling devices ranges between 22 °C and 26 °C.

In humid climates, healthy and comfortable humidity levels are often unmonitored and only treated indirectly through cooling and condensing water vapor, exhausting additional energy [3]. The untreated moisture incoming to the room leads to unpleasant indoor conditions. Moreover, the current air conditioning systems rely on refrigerants such as hydrofluorocarbons, R143a, R404A, R407C, and R410A [4]. These refrigerants have a detrimental impact on the environment in the long term as these refrigerants tend to leak and contribute profoundly to global warming via the greenhouse effect, which will continue to worsen with increasing demands of air-conditioning over the next 30 years [5].

Alternatively, the United States Department of Energy and Dais Analytic suggests that an improvement in energy savings of about 50-89% can be made using membrane-based air cooling technology compared to the traditional mechanical air conditioning systems [6]. Moreover, membrane-based cooling technology reduces or removes the water vapor content of the inlet air, allowing for better thermal comfort and could reduce the spread of viruses such as severe acute respiratory syndrome (SARS) and influenza A virus subtype (H1N1) [7]. Different technological advancements have been proposed under alternative energy or other novel methods, including membrane-based air-dehumidification cooling.

The principle of air-dehumidification air-cooling lies in reducing the temperature of warm air by cooling it down with cool water mist. As seen in Figure 1, the humidified cool air then enters the module housing several selective membranes, which allow water to permeate and be removed from the system. The retentate passes the cool dry air, completing the process for the desired effect [8].

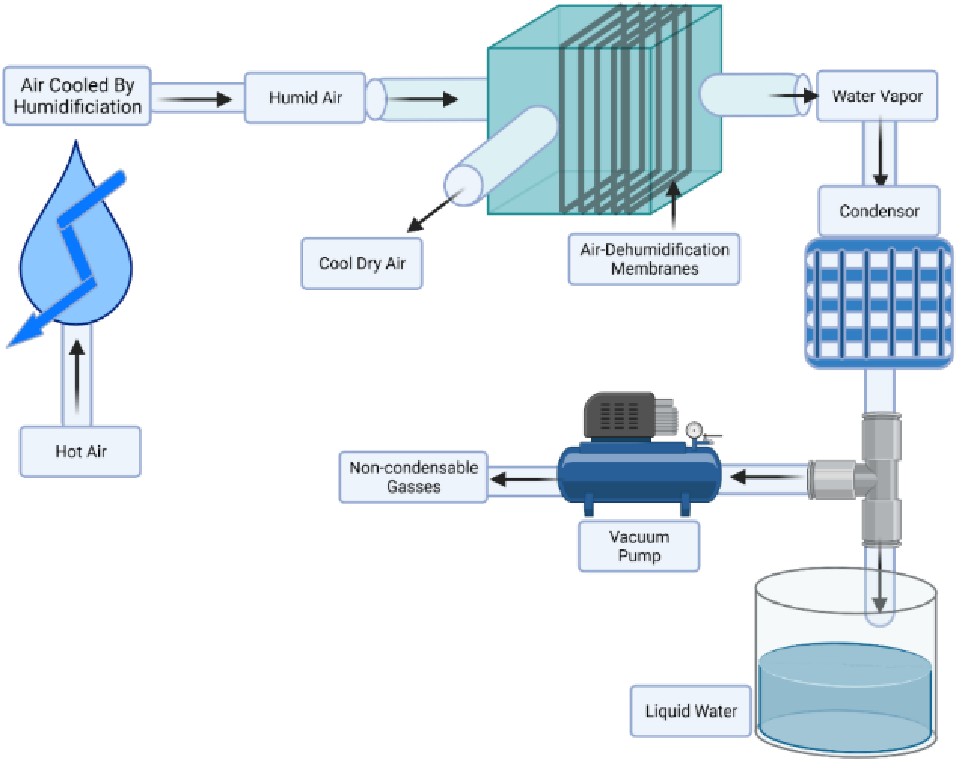

Figure 1 - Reproduced air dehumidification air-cooling process as per Calridge-Culp-Liu's patent [8]

The reduction in the water content via membrane air-dehumidification is more direct and cost-effective than the conventional heating ventilation and air-conditioning systems (HVAC). As seen in Figure 2, the isothermal removal of water is done in a singular step, from point 1 to 3 via point A. This process is much more efficient than the conventional cooling-compression systems used to dehumidify the air. There is no need to cool the air first to condense the water, albeit avoiding the longer, more energy-consuming route [8].

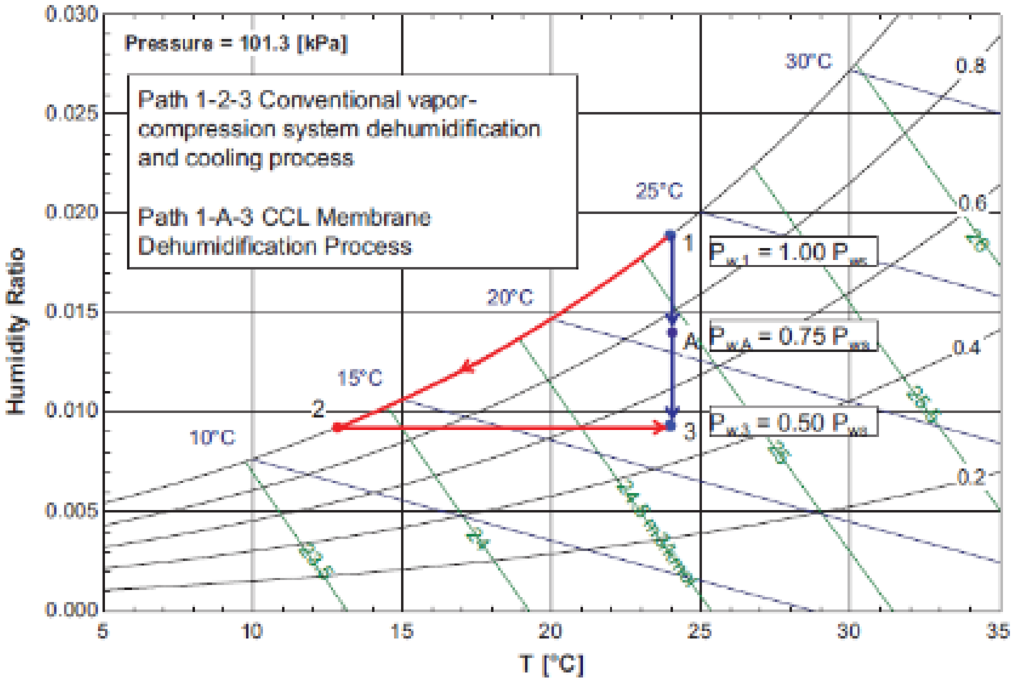

Figure 2 - Psychometric chart comparison showing the pathway of conventional air-cooling processes compared to a novel vacuum membrane-based process, adapted from Culp [8]

Liquid desiccants have been proposed to remove water with membrane filtration to facilitate the removal of water vapor. These systems use hygroscopic liquids, which capture the moisture from the humid air via absorption. Commonly used liquid desiccants are lithium chloride (LiCl), lithium bromide (LiBr), calcium chloride (CaCl), triethylene glycol (TEG), and potassium formate ($KHCO_2$). However, the issue with using liquid desiccant-based air-conditioning is the leakage of liquid desiccants in the dry air over time. The desiccants themselves are of toxic and corrosive nature, cause of concern for human health and material surrounding over long periods [9]. Moreover, these liquid desiccants require regeneration, adding energy, maintenance costs, and complicated operative measures [10]. Therefore, a safer alternative with equal or better cooling and air dehumidification needs to be sought.

The amended solution for air-dehumidification-based cooling can be found in novel membrane-based systems, which rely on a conjecture of optimum combination between the module design and membrane performance. Membrane-based air-dehumidification without desiccants has the advantage of being non-toxic, clean, and energy-efficient as opposed to desiccant-based systems. The modules that house the membranes aim to provide the best environment for air dehumidification by varying inlet flow orientation, membrane(s) orientation, and module dimensions. Also, the module's design with external parameters such as heating outlet streams or vacuum pumping at the permeate side can be performance-enhancing elements [11]. The modules of such cooling devices vary. Membrane modules such as flat sheet modules (Figure 3), crossflow modules, vacuum-based, counter-flow are few different types each enhance specific objectives and outcomes required [9, 11-13]. The dry air itself can be chosen to be cooled via conventional methods by using refrigerants or resort to less alternative measures as cooling water in a heat exchanger format [14].

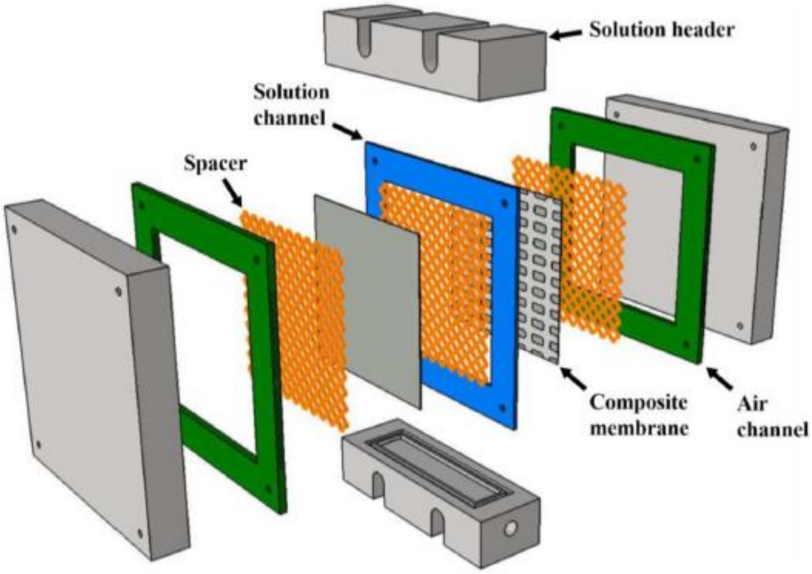

Figure 3 - Flat sheet membrane module displaying each part adapted from Ham et [9]

On the other hand, novel membranes are the second part of the complete system and the heart of the operation. Air-dehumidification can be made possible due to the use of gas separation membranes, which hold the capability of separating several types of species depending on the differences in solubility and diffusivity of different components. For air-dehumidification, the key separation that needs to occur is water vapor from humid air, which is a gas separation process. The types of gas separation membranes are porous polymeric, dense/non-porous, and asymmetric membranes. Where porous polymeric membranes have poor separation properties and good transport properties, dense non-porous membranes perform in vice-versa, with good separation properties and poor transport properties. With a combination of both, asymmetric membranes pose a thin dense, non-porous layer supported on thick, porous support to amplify the benefits of both transport and separation properties in the two structures.

The membrane itself has its variables that are to be investigated and made use of. These variables can differ from materials, fabrication methods, and their end-use. Key characteristics on which its ensured premium performance can be measured are water/air separation and great water permeance and air rejection.

The membrane performance depends on several factors. One of the most important include the water flux, which can be denoted by equation 1

$$J = k\Delta\omega A \tag{1}$$

Where k is the overall mass transfer coefficient (kg m^{-2} s^{1}). $\Delta\omega$ is the ratio of humidity difference (kg/kg dry air), and A is the membrane surface area. The humidity ratio denotes the amount of water in the air at a specific temperature.

$$\text{Humidity ratio at saturation: } \omega_w = \frac{10^6}{e^{\frac{59294}{T}}} \tag{2}$$

$$\text{Humidity ratio for at x\% humidity: } \omega_s = \frac{x10^6}{e^{\frac{59294}{T}}} \tag{3}$$

where *x* donates percentage humidity.

Another factor that determines the wetness of the air's input and output can be determined by relative humidity. The relative humidity is a function of the humidity ratio, ω, and temperature and is dimensionless.

$$\frac{\phi}{\omega} = \frac{e^{\frac{59294}{T}}}{10^6} - 1.61\phi \tag{4}$$

Alternatively, a more common method used to test the performance of the membrane is the measure of permeance. The permeance of water in air-dehumidification can be denoted by equation 5, where permeance, $\dot{J}$ has the units of

$\frac{mol}{m^2sPa}$

$$\dot{J}_{H2O} = \frac{\dot{N}_{\mathrm{H2O}}}{A\cdot(\Delta P_{\mathrm{H2O}})_{lm}} \tag{5}$$

Moreover, another critical parameter that translates a membrane's performance is the separation factor between water and air, comparing the amount of water and air in the permeate side against the retentate side.

$$S = \left(\frac{\dot{N}_{\mathrm{H2O,p}}}{\dot{N}_{\mathrm{H2O},R}}\right)\left(\frac{\dot{N}_{\mathrm{air,R}}}{\dot{N}_{\mathrm{air,P}}}\right) \tag{6}$$

The fabrication process of a membrane is directly correlated with the membrane material. Whereas inorganic membranes such as those made from metals and ceramics show excellent resistance against mechanical and thermal afflictions, their high cost, brittleness, and difficulty for mass production make them unfavorable contenders for air-dehumidification membranes [15]. On the other hand, polymeric membranes are considerably cheap and are relatively easier for upscale production [16]. However, the mechanical properties of polymeric membranes are not up to par with those of inorganic membranes. In recent works, it can be observed that the mixed-matrix form of organic-inorganic membranes remains to be affordable for large-scale production and bode better mechanical properties than the polymeric membranes [17].

Recent research has shown that the performance of homopolymers, such as polysulfone, polyether sulfone (PES), and polyvinyl difluoride has great support membranes for ultrafiltration processes [18]. Moreover, in those studies, the addition of nanofillers such as titanium dioxide, carbon nanotubes, metal-organic frameworks, and graphene-based derivatives has significantly enhanced the properties and performance of those membranes [19]. Moreover, the functionalization of nanofillers and polymers with functional groups, such as sulfone and amine, improves the membrane's properties and performance [20].

The research conducted for this dissertation focuses on incorporating functionalized graphene oxide (GO) in a composite membrane of PES as the support membrane with polyether block amide as the active layer. GO is exceptionally rich with oxygen-based functional groups such as epoxy, carboxyl, and hydroxyl, making chemical modification possible [21]. To improve the hydrophilicity of GO, sulfonation is proposed by grafting sulfanilic diazonium salt in the place of a hydroxyl group on the plane of GO. The study undertaken in this thesis is the proposed fillers added to the support matrix and the active layer.

CHAPTER II

2. Literature Review

2.1 Membrane-Based Air-Dehumidification for Air Cooling

Air-dehumidification cooling can provide up to 89% savings from conventional cooling devices and provide optimum conditions for health and comfort [6]. Different platforms for air-dehumidification-based cooling have been proposed. More popular is the usage of liquid desiccant-based air-dehumidification. However, more recently, vacuum sweep air-dehumidification and isothermal aid-dehumidification systems have been looked upon more favorably due to the ease of maintenance and process simplicity. Different types of membranes, such as proton exchange membranes, have also provided a further look into air-dehumidification cooling possibilities.

The parameters in contention for the performances of said air-dehumidification modules are measured by the energy efficiency, coefficient of performance, and amount of water removed. These, in relation to the amount of water removed, are some indicators to measure the performance of the air-dehumidification modules.

The coefficient of performance is a measure of useful cooling relative to the work input.

$$COP = \frac{\Delta H_t}{W} \tag{5}$$

Where W is the amount of work put in and ΔH_t is the useful cooling provided by the system.

Moreover, the efficiency of is undertaken by the following:

$$Efficieny = \frac{T_{a,in} - T_{a,out}}{T_{a,in} - T_{a,sat}} \tag{6}$$

Where T_a is the temperature of the absorbent compared to the temperature at saturation, similarly, this can also be converted into the mass fraction of the absorbent.

$$Efficieny = \frac{W_{a,in} - W_{a,out}}{W_{a,in} - W_{a,sat}} \tag{7}$$

The third performance parameter is water removal. In simple terms, water removal is the amount of water removed from the humid air. In several cases, the reported numbers were per time at a water removal rate. The more water is removed, or the quicker the water is removed, is better.

$$Water\ Removal\ Rate = m_a(W_{a,in} - W_{a,out}) \tag{8}$$

2.2 Liquid Desiccant Air-Dehumidification Cooling

Some of the more common liquid desiccants used are lithium chloride (LiCl), lithium bromide (LiBr), calcium chloride (CaCl), triethylene glycol (TEG), and potassium formate ($KHCO_2$) [9]. Each of these desiccants possesses an affinity to absorb water molecules, stripping the water content out of air drying it in the process. The desiccants work in cohesion with the selected air-dehumidification membranes. The membranes permeate the water, which is then absorbed by the desiccants, either flowing in a crossflow or a counterflow direction to the humid air inlet [22].

As seen in Figure 4, liquid desiccant-assisted membrane air-dehumidification structure varies depending on the membrane type and orientation. The main challenge posed with liquid desiccants is the regeneration of the hygroscopic liquid. The liquid desiccant needs to be dehumidified to maintain its effectiveness in the process. However, the thermal energy required to dry the hygroscopic liquids of the captured water is high and proves to be counter effective. Therefore, the techniques proposed to regenerate the liquid desiccant that solves this issue are hollow fiber (HF) membrane contactor, electrodialysis regenerator, and vacuum regeneration [22].

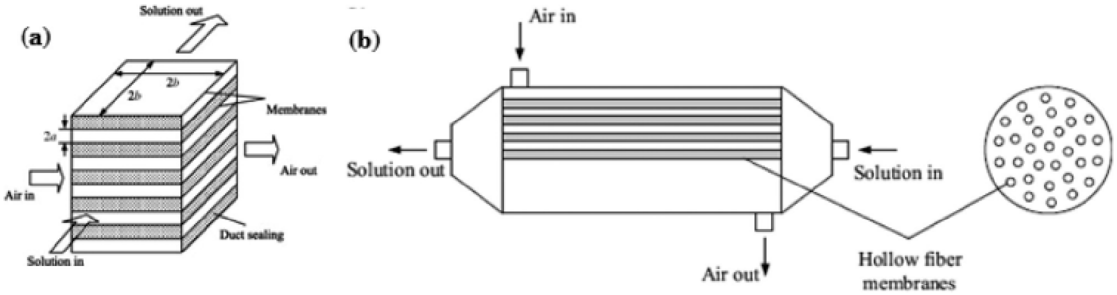

Figure 4 - Liquid desiccant assisted membrane-based air-dehumidification in a) parallel plates and b) HF membranes adapted from Chen et al. [22]

In a review, all liquid desiccant assisted membrane air-dehumidification systems provided a coefficient of performance (COP) less than 1, where the efficiency of each system does not exceed 80%. The water removal rate was excellent at over 1 kg/m^{2}hr. The overall performances of liquid desiccant assisted membranes for air-dehumidification performance are summarized in Table 1.

Table 1 – Summary table for liquid desiccant assisted membrane air-dehumidification module performance.

	Humid Air Inlet			Desiccant			Performance			
Membrane	T (°C)	Humidity (%)	Air Flow	T (°C)	Flow	Conc. (%)	Efficiency	Water Removal	COP	Ref
N/A	22-38	75%	V_s = 1.74 m/s	25	0.081 m/s	36%	70-80 %	1200 - 3200 g/m^2h	N/A	[9]
PVDF	35	5-95%	35 m^3/hour	25	1 L/min	35%	74%	N/A	0.7	[23]
PVDF	36	22.50%	5 kg/hour	25	N/A	35%	20-30%	MRR = 2-10 g/s	N/A	[24]

2.2.1 Proton Electrolyte Membrane Based Air-Dehumidification Cooling

At the heart of the proton electrolyte membrane (PEM) structures exists the proton conductive membrane, sandwiched between two catalytic porous electrodes on either side. Outwards of the catalytic anode and cathode reside diffusive layers for the inlet and outlet contents of the process. In dehumidification using a PEM, the water content of the humid air enters the anode side’s diffusive layer, going under the water-splitting reaction at the anode. The proton conductive membrane attracts the positive hydrogen ions which pass through the membrane. At the cathode, a reaction with free electrons and oxygen forms water once again, which then proceeds to pass through the diffusive layer and to cause water to permeate, this schematic is shown in Figure 5 [25].

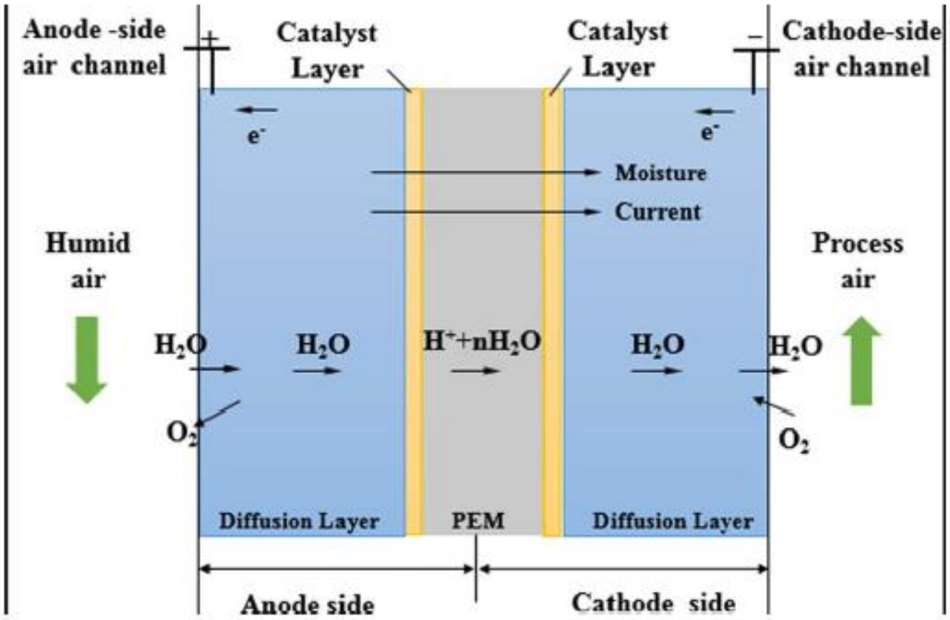

Figure 5 - Schematic of proton electrolyte membrane air-dehumidification adapted from Qi et al. [25]

The water removal rate and separation performance of proton exchange membrane dehumidification are very good. It can reduce a high amount of humidity; however, due to the electrical voltage requirement, the coefficient of performance is low at about 0.33. Moreover, practically the system of catalyst-covered electrodes includes complications and increased maintenance. Despite their excellent performance to dehumidify, the PEM air-dehumidification is still energy inefficient.

2.2.2 Vacuum Based Air-Dehumidification Cooling

The structure of a vacuum-based air-dehumidification cooling system relies on using a vacuum pump on the permeate side of the membrane. The suction pump's draw allows water to be compressed and cooled before passing as liquid water, as shown in Figure 6. On the membrane module side, the rejected air reduces in enthalpy due to the reduced water content. This structure is the simplest; however, it relies on exceptional performance from the membrane at the structure's core.

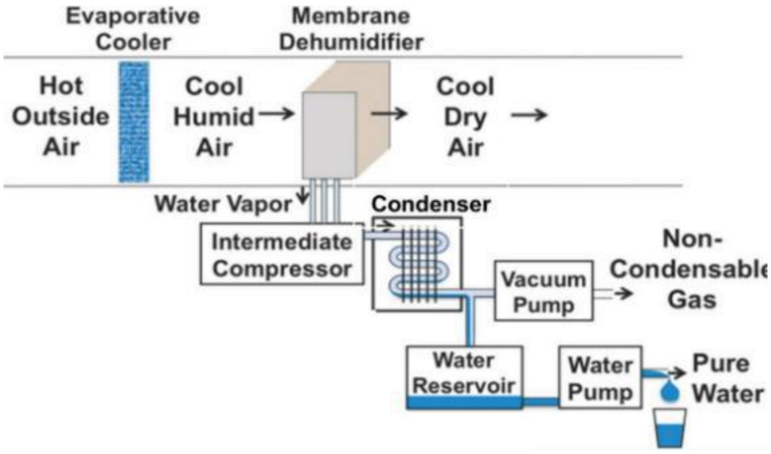

Figure 6 - Energy efficient dehumidification using vacuum pump - patented by Culp [8].

This module structure proves to have the highest COP and frequently has a COP above 1. Whereas in energy comparisons, it shows to use less than 2% energy for the same output as liquid desiccant systems and provides an overall 26.2% energy savings [8]. Its energy efficiency coefficient also near one or more, which is highly encouraging [11] [26].

Table 2 – Performance of vacuum Based-Air dehumidification cooling modules

		Air			Performance			
#	Membrane	T (°C)	Humidity	Air Flow	Efficiency	Water Removal	COP	Ref
1	Several	25	0.011 wt. %	0.17-0.86 m^3s/m^2	Cross Current = 1.15	2.9-5.6 mol/m^2hr	N/A	[26]
2	PVA-TEG	30	RH 90%	N/A	Up to 97%	11900 GPU	2 to 3	[11]
3	N/A	34	0.001795 wt. %	N/A	COP_{Carnot} 1-Stage: 26-56% COP_{Carnot} 5-Stage: 15-30%	N/A	N/A	[8]
4	PAN/PDMS HF	15	60%	N/A	26.2% Energy Savings	5 g/m^3 Reduction	N/A	[3]

2.3 Introduction to Gas Separation Membranes

2.3.1 Gas Separation Membranes

The advancements in membrane technology have increased exponentially ever since the early developmental stages. Membrane technology has come a long way since the early fundamental development stages of Graham's law of diffusion and the first systematic measurement of permeability in the 1950s [27]. The advancements can be credited to the progress in material science, material processing, and the demand for technological innovation in material separation. Over the last century, membranes have been utilized in various processes with their respective driving forces. The main driving forces in membrane operations are pressure, concentration differential, heat, and electrical potential. Apart from the set driving forces, objective-based membrane fabrication can be finetuned on several things, including the material of the membrane, the fabrication technique, and post-fabrication surface modification.

Membrane technology has long been used for gas separation processes, recorded back to the early 19th century. Graham et al. conducted the first recorded experiments of using membranes for gas separation. In their experiments of permeating carbon dioxide through natural rubbers, Graham et al. concluded that there was no correlation between gas diffusion coefficients and the rate of gas permeation [28]. Graham et al. concluded the permeation rate to be a mix of solubility-diffusion and equated it as:

$$P = DS \tag{9}$$

where P, D, and S are permeability, diffusion, and solubility coefficients, respectively, whereas the permeability units are in Barrers. An equally important parameter of gas separation is the selectivity, α_{AB}, which can be presented as:

$$\alpha_{AB} = \frac{P_A}{P_B} \tag{10}$$

Where P_A and P_B are the permeability components of two gasses [28].

Since the advent of synthetic polymers in the 1980s, membrane technology for gas separation has advanced tremendously. Some of the conventional uses of membranes for gas separation are air separation (oxygen/nitrogen), hydrogen separation (hydrogen/nitrogen, hydrogen/flue gas), gas sweetening (carbon dioxide/natural gas), and other vapor/gas separations. Some of the polymers used in commercial processes can be seen in Table 3, where polysulfone, polyimides, silicon rubber, and cellulose acetate are common materials used to fabricate gas separation membranes [29].

Table 3 - Commercial manufacturers and membrane materials used [29]

Commercial Manufacturer	Membrane Material
Permea	Polysulfone
Medal	Polyimides
Generon	Cellulose Acetate
Ube	Polyimide
Helmholtzz Centrum	Silicon Rubber
Grasys	Polyimide, Polysulfone
OPW Vaposaver	Poly (trimethylsilyl propyne)

The three categories of gas separation membranes are porous polymeric membranes, dense non-porous, and asymmetric membranes. The pore size in porous polymeric membranes must be microporous, where the pore sizes are less than 2 nm. These membranes can be fabricated through the same methods as pressure-driven membranes. Porous gas separation membranes usually exhibit poor separation properties, although they boast prominent transport properties. In contrast, dense non-porous membranes can either be fabricated via melt extrusion or solution casting, where the solvent is dried off, leaving a thin non-porous layer behind.

Non-porous membranes exhibit excellent separation properties, although they have poor transport properties, yielding low gasses' permeability. The third type of gas separation membranes is asymmetric membranes that include a thick, porous matrix that provides physical support for a thing coating layer of a dense, nonporous layer. These are generally classified as integrally skinned and thin-film composites. These membranes aim to balance separation at the active layer and transport through the porous media [30].

2.4 Membrane Materials

2.4.1 Metal Membranes

Metallic membranes, like organic membranes, apply to a variety of processes. They are highly liked due to their high chemical, thermal and mechanical resistances. The main reason for these exceptional mechanical features is the metallic-based materials used to fabricate them. Some of the most common materials used are aluminum oxide (Al_2O_3), Titanium oxide (TiO_2), zirconium oxide (ZrO_2), silver, palladium, and various other alloys [31]. The categorization of metal membranes is primarily done into dense metallic membranes and porous membranes. Porous metal membranes are at the forefront of metallic membrane technology, including stainless steel, titanium, nickel, and their alloys [32]. Microfiltration has been one of the critical processes where porous metal membranes were used frequently, especially with the application of drinking water treatment [33].

2.4.2 Ceramic Membranes

Ceramic membranes are an emerging technology and have exponentially grown in the last few decades. Currently, ceramic membranes are one of the leading membranes for water filtration. Like other inorganic membranes, ceramic membranes also boast high thermal, chemical, and mechanical resistances and lower fouling rate and membrane longevity. Like most membranes, the range of operation spans from microfiltration to nanofiltration. The most common type of ceramic membranes is the porous type with asymmetrical structures based on support and the intermediate layer. The shape of the ceramic membranes plays a vital part in the application where flat sheet, flat disc, and tubular membranes are a few of the common structures. The fabrication of these membranes is usually done with extrusion, pressing, slip casting, tape casting, sol-gel, phase inversion, to name a few [34-36].

2.4.3 Polymeric Membranes

Conventionally across the board of all membrane processes, polymeric membranes have taken the forefront. This is due to the fast-maturing nature of polymeric materials and polymeric membrane technology. A good performance criterion of selectivity and permeability at a lower cost also appeals to the heavy use of polymeric materials for membranes [37]. However, a common downside of polymeric membranes tends to be poor surface characteristics with high hydrophobicity resulting in consistent fouling, which consequently shortens the lifecycle of the membrane [38]. Some of the oldest membranes were made of polymers and cellulose-based, such as cellulose acetate (CA) [39]. Another cellulose-based polymer used for membrane synthesis is cellulose nitrate. Polysulfone

(PS) is another commonly used polymer for the fabrication of membranes, especially for the ultrafiltration process due to its good chemical and thermal stability [40, 41].

Other polymer materials such as polyether sulfone (PES), polyacrylonitrile (PAN), polytetrafluorethylene (PTFE), polyvinyl difluoride (PVDF), and polyimide (PI) can also be commonly found in the process of ultrafiltration. In contrast, polymer materials like polyvinyl difluoride (PVDF), polyvinyl alcohol (PVA), and polypropylene (PP) can be applied to microfiltration as well. With advanced synthesis techniques and surface modifications, the range of membrane processes can vary from microfiltration to nanofiltration [42].

2.4.4 Metal-Organic Framework-based Membranes

Metal-Organic Framework (MOF) membranes are a nanopores hybrid of metal ion clusters connected with organic linkers. These ion clusters centered with organic molecules exhibit the best properties of both the pure organic and inorganic membranes. Metal-Organic Framework membranes are produced by growing continuous polycrystalline – MOF layers on porous substrates. These types of structures are called pure MOFs. These porous substrates are more often metallic based, such as Aluminum Oxide (Al_2O_3), Titanium Oxide (TiO_2), and Silicon dioxide (SiO_2). One of the most common pure MOFs is Zeolite Imidazolate Framework (ZIF), which uses crystal growth on inorganic bases using a variance hydrothermal or solvothermal synthesis process. On the other hand, hybrid MOFs also exist where MOF crystals are used as fillers in polymer solutions to result in a mixed matrix membrane of the two [43].

With its outstanding performances due to its dual properties being exhibited, MOFs still carry disadvantages. The main one being the difficulty in upscaling for industrial usage without hindering the performance output of the membranes [44]. Two phenomena simultaneously determine the performances of MOF: the adsorption and kinetic separation, a similar analogy to catalysts providing active sites. Dense metallic structures can cause poor diffusion, therefore, can lead to poor overall performances in permeability and selectivity. Similarly, the solid, consistent pore structure of MOFs can outperform other membrane materials [43].

2.5 Membrane Fabrication Techniques

To enhance the performance of the membrane per the selected criteria, the materials used to fabricate the membranes can undergo a variety of processes. Furthermore, the membranes and the materials can be subjected to modification for better performance. The membranes can be synthesized in various ways; some key decisive factors that play a decisive role in selecting the synthesis method depend on material characteristics and end goal application. Some methods commonly used to synthesize membranes are extrusion, interfacial polymerization, coating techniques, and phase inversion.

Extrusion is a technique to prepare multilayered membranes in one step. Extrusion is more advantageous in fabricating HF membranes, although it is also implemented when making multilayer sheets, blown, or cast films, and wire coatings. However, some of the downsides to this process are the lack of control over selectivity and permeability and the membrane's poor performances in the respective criteria. Moreover, materials with higher volatility and lower viscosity are generally harder to use in this process. On the other hand, its cheap operating cost, repeatability, and mass scaling are its positive sides [45]. Furthermore, the improved adhesion between the membrane layers, its multilayer functionality, reduced likelihood of surface defects, and excellent inclusion of permselective membrane layers, which otherwise would not have been able to form a free-standing membrane by themselves [46]. The process works when dope is extruded through the outer orifice while at the same time an internal coagulant is introduced. Extrusion and co-extrusion can be carried out in a dry-wet phase inversion process to produce dual-channel HF membranes. [45].

Various coating techniques create thin layers of materials by depositing small amounts of material very quickly. The most effective and mainly used to fabricate membranes is the electrospinning method. The fast-spinning technique of the electrospinning process is to create polymer fibers with diameters of 50 to 500 nm. More advantages of the electrospinning process include the highly porous membranes with small porosity, helping permeability to be increased while bolstering the selectivity [47]. Electrospinning is usually done by generating an electrical field by passing a high voltage of 0-30 kV through a copper plate wrapped with aluminum foil. On the positive electrode, the solution and a copper wire reside in a 1-5 mL small syringe with a 0.2-0.5 mm capillary tip [48].

Another technique used to fabricate membranes is interfacial polymerization (IP). In general, interfacial polymerization is used to produce thin-film composite membranes, where ultra or microfiltration membrane is dipped in a prepolymer's aqueous solution of a prepolymer, and the support membrane is then immersed in an aqueous solution acid chloride bath. When these two structures are met, an interfacial polymerization reaction occurs for a dense polymer layer. This is shown Figure 7, where IP on a polysulfone support is conducted where membrane initially is immersed in an amine solution and then left out to environmentally dry. Afterwards, the membrane is immersed in an TMC solution then cured in an oven at 100 °C. IP can produce thin membranes of 100-200 nm thickness. Repeatability for the reproduction of membranes can be an issue due to the inconsistent reaction at the interface. However, if successful, the IP process can produce membranes with excellent permeability and selectivity. The type of membrane mainly influences the pore sizes and support membranes used [49].

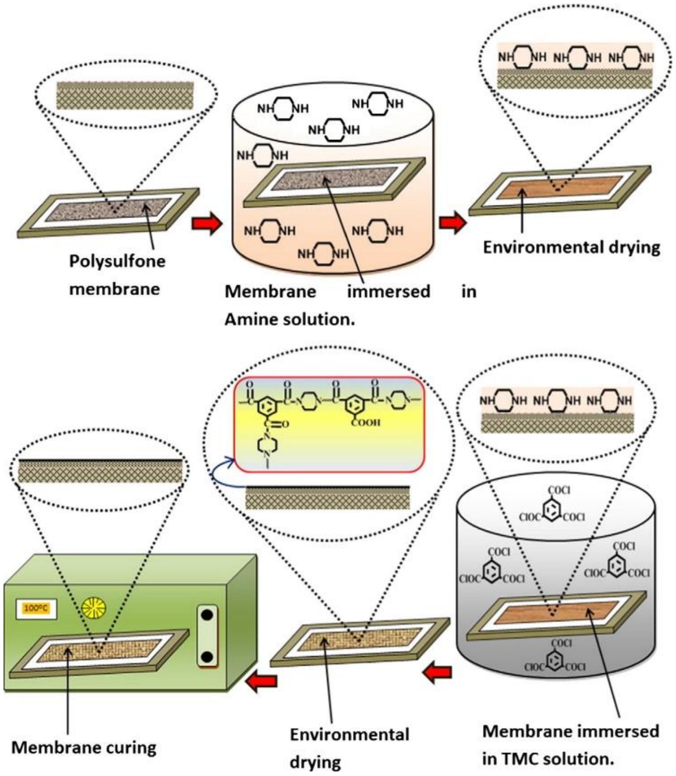

Figure 7 - Interfacial polymerization of a polysulfone membrane to fabricate a thin film composite membrane [49]

Phase inversion is one of the most common methods used primarily for the synthesis of polymeric membranes. Its key strengths are the versatile use of a homogenous solution with a dissolved polymer in a solvent. The scientific principle behind this synthesis technique lies in the miscibility gap between the polymer and solvent. Two main driving forces induce phase inversion: thermally induced phase separation (TIPS) and non-solvent induced phase separation (NIPS). The lowest toxicity should select the solvent for both phase separation, high boiling point, low molecular weight, and as environmentally friendly as possible [50].

Varying the temperature to induce phase separation is mainly done for the fabrication of microporous membranes. This process produces highly porous membranes with a narrow range of pore sizes. TIPS is done by dissolving the polymer in a solvent of a high-boiling point where the polymer solution's crystallization temperature is lower. Then the solution is cooled down after casting. Like most membrane techniques, TIPS has a reputation for producing membranes with low defects, high porosity with a lower pore size range, and repeatable results. It is most suitable for membrane materials that are not commonly soluble in most solvents [51].

Similarly, the homogenous solution is cast using a membrane casting machine for NIPS and then coagulated in a quenching bath. For NIPS, the solvent of use must be a specific kind that may coagulate in the non-solvent bath. A similar method is used to fabricate HF membranes, except the casting technique can be substituted for spinning fiber immersed into the coagulant [52]. The two methods of fabricating hollow fiber and flat sheet membranes through NIPS can be seen in Figure 8. Moreover, NIPS is also a beneficial technique in fabricating membranes with inorganic and organic membranes

[53]. With phase inversion, the concentration of the polymer solution in the solvent is key to pore size and filtration specificity. Where the higher concentration of the polymer solution produces a smaller pore size, typically, a membrane fabricating for ultrafiltration can have a polymer weight percentage of 12-20% in solvent, whereas nanofiltration and reverse osmosis can be greater than 20% [54].

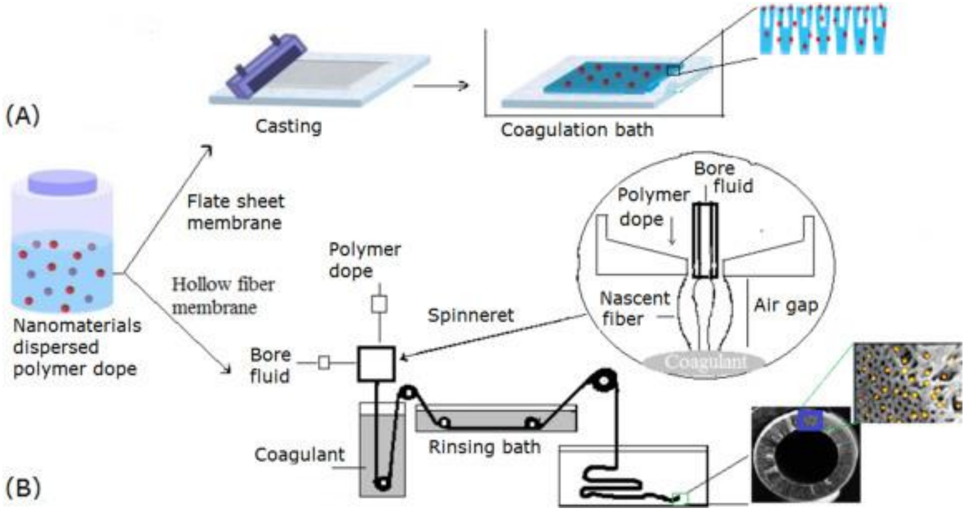

Figure 8 - Fabrication of a) flat sheet and b) hollow fiber membranes through non-solvent induced phase inversion (NIPS) [55]

2.6 Air-Dehumidification Membranes

Many different classes of membranes have been tried and tested for the aspect of gas-liquid or vapor-liquid separations. Although for applying air-water separation or air dehumidification, a wide range and type of membranes are used. These include Zeolite Imidazolate Framework (ZIF), polymeric membranes, composite membranes, HF membranes, and ceramic membranes. In short, these can be divided between organic and inorganic membranes with various support structures.

The key performance criteria for these membranes are water – nitrogen selectivity, water permeate flux, and wettability performance in the literature. These criteria are measured up with the flow rate of air at fixed pressures and temperature. Moreover, the water vapor concentration in humid inlet air or relative humidity is another variable to be sought after. The thermal performance of these membranes is not key, although it is commendable to withstand temperatures above the corresponding saturation temperatures at respective operating pressures for end goal application.

2.6.1 Inorganic Membranes

Other inorganic membranes reported for air dehumidification consisted of ceramic membranes. A study conducted by Asaeda et al. prepared the membranes via dip-coating thin porous alumina in sodium silicate for 10 minutes at 100 ℃ [56]. The resultant ceramic membranes produced a water flux of an average of 35 $\frac{mol}{m^2 * hour}$ at 50% relative humidity and an average of 55 $\frac{mol}{m^2 * hour}$ at 90% relative humidity.

Although these inorganic membranes boasted good water permeability and water flux performance, material characterization of the formed membranes was often left without investigation. Therefore, the whole area of study is left without room for further improvements or advancement. Moreover, the reported values for selectivity resulted in a wide inconsistent range, making it harder to verify its effective performance. On the other hand, a range of testing over 50-90% relative humidity and mildly warm temperatures satisfy its requirement and real-world parameter usage for applying air conditioning on a warm, humid day.

2.6.2 Organic Membranes

Liu (2020) conducted a study on polyvinyl acetate (PVA) and polyvinylidene fluoride (PVDF) HF composite membranes with poly(dopamine) (PDA). The organic HF membranes were fabricated through the dry-wet spinning process. The variation between different membranes was of varying modification times and PDA concentration. The water vapor permeance results that were the most promising were of the HF membranes that had gone through 30 minutes of modification process and had PDA concentrations of 0.1 g/L. The resulting permeance and selectivity for the 0.1 g/L PDA with PVA-PVDF HF composite were 3000 GPU and 2.2 (water/nitrogen), respectively [57]. The final and best-performed membranes had a mean average more size of 9.27. These results presented by Liu (2020) resulted from experiments conducted at 25℃, which can be deemed favorable conditions for real-world applications. Moreover, Liu (2020) does not disclose any other operating parameters of testing, neither the membrane size nor any relative humidity, inlet pressure, or time is taken.

A study regarding 2D stacked GO (GO) membranes was conducted by Shin et al. for air dehumidification. The study utilized GO produced by Hummer's “improved method”, also known as Tour’s method, to form a slurry thinned out to 60 µm sheets. The said sheets are used as membranes, and the tests at 80% relative humidity and 30.8℃ yielded permeability of $1.25x10^5\ Barrer\ \left(6.10x10^{-11}\ \frac{kmol*m}{m^2*s*kPa}\right)$ and selectivity of over 10000 [58]. A wide range of testing was conducted at various relative humidity and temperatures. The results showed sustained results and promising real-world applicability.

Using other processing techniques, Tanhiara et al. investigated Polyimide-based hollow-fiber membranes for air dehumidification. They used Polyimide prepared from biphenyl-tetracarboxylic acid (BPDA) and tested them in dehumidification set up at varying conditions of 0.3 to 1 MPa pressure and 0 to 60℃ temperature. These tests yielded promising results showing water permeance of $1.3x10^{-3}\frac{cm^3}{cm^2*cmHg}$ and a selectivity of 100-700. The layer thickness of the polymers was averaged at 150 nm. The key highlights to this membrane's performance were its good permeability, selectivity, and thermal stability up to 150 ℃ [59].

Liang et al. investigated a polydimethylsiloxane (PDMS)-polyacrylonitrile (PAN) thin-film composite membrane. The dry-wet spinning process led to the composite, prepared by dip-coating the PAN support in the PDMS solution, forming the PAN HF substrates. The resultant membrane was suitable for various dehydration applications, including removing water from the air.

A thorough mechanical analysis was also conducted, allowing a maximum load of 2.28 newtons with a maximum tensile strength of up to 5.85 MPa. Liang et al. attributed the enhanced mechanical properties to the fast-spinning rate to fabricate the HF membrane. The membrane average pore size was 5.6 nm, a 70% reduction from other PAN membranes. Liang et al. also noted that faster spinning led to smaller pores and higher porosity. The overall structure of the PDMS/PAN composite looked like can be seen from Figure 9, where the HF PAN substrate and its coating of PDMS are shown.

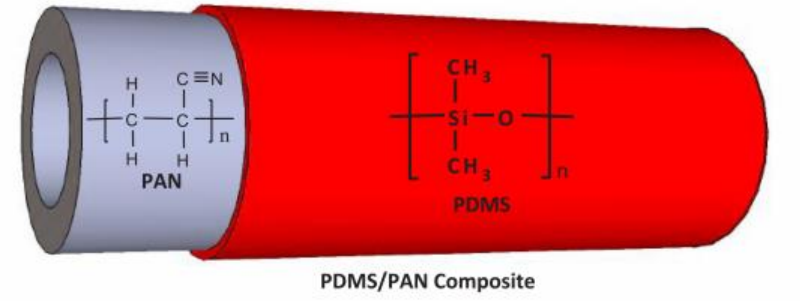

Figure 9 - PDMS/PAN HF membrane composition [60]

Moreover, the selective layer of the PDMS was about 260 nm. As for the main performance aspects, the PDMS-PAN HF membrane yielded water permeance of up to 3700 GPU at 65% relative humidity after 48 hours of stability. As shown in Figure 10, the sweep flow rate started to be less effective in the permeance of water vapor after 600 ml/min [60].

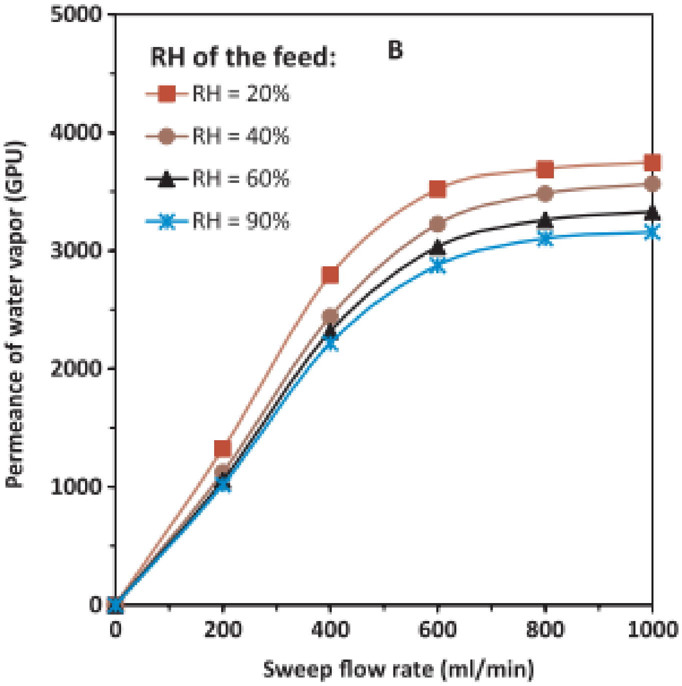

Figure 10 - PDMS/PAN HF membrane performance with varying relative humidity and sweep flow rate [60]

PES (PES) is a polymer that has a good oxygen atomic percentage in its repeated structure, making it ideal for water permeation. A studying conducted by Ingole et al. formed a TFC-PES composite by first preparing the PES via phase inversion in a dry-wet spinning process to form HF membranes. The composite was prepared by interfacial polymerization with the covalent TFC organic chemicals, such as 1,3-benzenedithiol (TFC-HF-1), m-phenylenediamine (TFC-HF-2), piperazine (TFC-HF-3) and 1,3,5-benzenethrithiol (TFC-HF-4). These membranes underwent challenging characterization where they retained a water contract angle of 65.2 to 52.1°. Moreover, they tested the possibility of dehumidification at 30 ℃ and 3 Bar while investigating permeability and selectivity. The best membrane performance in water permeance and selectivity was TFC-HF-1, the PES polymer spun and interfacially polymerized by 1,3-benzenedithiol. The TFC-HF-1 yielded permeance of 2054 GPU with an H_2O/N_2 selectivity of 119. Consistent pore structure was observed by SEM, giving evidence of reliable performance across membrane sheets. Using an economical and hydrophilic base such as PES enhanced the performance to yield high permeance. However, the selectivity was low, requiring increasing the thickness of the TFC layer. The other TFC-HF performances were comparatively less impressive, with TFC-HF-3 yielding performance of 1800 GPU and selectivity around 90. In certain circumstances, TFC-HF-3 could also be another contender in further investigation and development of air-dehumidification membranes. The comparative performances of all membranes polymerized with all the different organic covalent chemicals can be seen in Figure 11 [61].

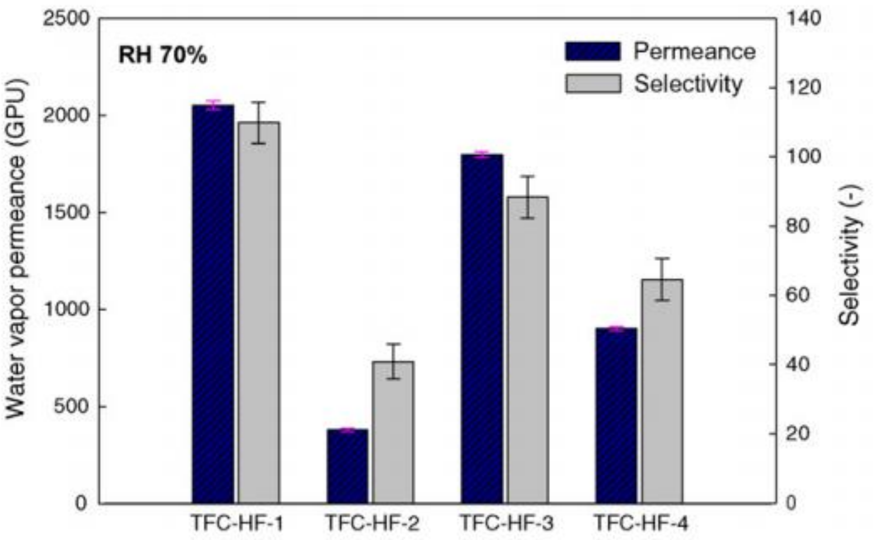

Figure 11 - Permeance and selectivity of TFV-HF at varying treatment times [61]

Another composite formed by coating polyvinyl alcohol (PVA) on PES support was conducted by Zhang et al. for air-dehumidification. They used glacial acid as a catalyst and produced a large area of 100 cm^2. Lithium chloride was also added to enhance hydrophilicity. Moreover, membranes with different LiCl concentrations went through multiple variable cycles with different feed flow rates. The highest concentration of LiCl of 2 g produced the best Peclet number and the lowest contact angle of 53.3°. This study did not report permeability and selectivity results. However, the improvement of PES/PVA composite by adding LiCl was noted. The morphology (Figure 12) of the membrane was atypical for a flat-sheet thin-film composite. Although the size of pores was not reported, the visible large contact area for water to permeate was evident [62].

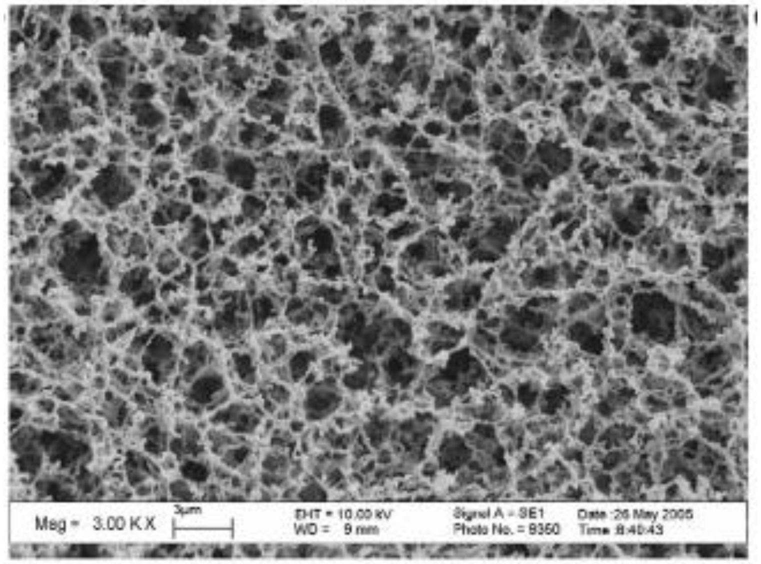

Figure 12 - PES/PVA TFC surface morphology captured by SEM [62]

Table 4 – Performance of organic air-dehumidification membrane

Membrane	**Configuration**	**Testing Details**	**Morphology**	**Fabrication Technique**	**Membrane Performance**		**Ref.**
					Permeance	**Selectivity**	
PVA/PVDF	HF composite membrane	T: 25 °C P: 1 Bar RH: 25-50%	Mean pore size: 9.72 nm	HF Membrane: Dry-wet spinning process. PVA/PVDF membrane: Coating for 30 to 90 minutes	2898 GPU	H_2O/N_2	[57]
PES & Covalent TFN	HF Composite membrane	T: 30 °C P: 3 Bar	Contact Angle: 65.2 to 52.1°	PES: Phase Inversion Composite: Interfacial Polymerization	2054 GPU	H_2O/N_2 119	[61]
PVA/LiCl on PES support	TFC Membrane	RH: 70%	Contact Angle: 53.3°	Coating PVA casting solution on PES support. Glacial acid as catalyst.	N/A	H_2O/N_2	[62]
Polyimide Membrane	HF membrane	T: 0-60 °C P: 1MPaG RH: 70%	OD: 0.2 to 0.8 mm ID: 0.1 to 0.7 mm Layer thickness 50-200 nm	BPDA-Polyimides Dry-wet spinning process	1300 GPU	H_2O/N_2 100-700	[59]
PDMS/PAN	HF Membrane Composite	T: -10 to 60 °C RH: 0 - 100% (Rated: 65%)	Tensile Strength: 5.85 MPa	Dry-wet spinning process Dipcoat PAN HF membrane in PDMS Spun at 60 m/min	800-3700 GPU	H_2O/N_2	[60]

2.6.3 Organic-Inorganic Hybrid Membranes

The organic-inorganic hybrid membranes utilize both organic and inorganic materials either as substrates or as nanofillers.

Zeolite Imidazolate Framework membranes for the air-dehumidification were synthesized using several methods, including solvothermal, hydrothermal, ionothermal, and sonochemical synthesis procedures [63]. Tanskyi investigated the in-situ growth of zeolite crystals on microporous support, resulting in H_2O/N_2 selectivity of over 1500 [64]. Where the minimum effective water permeance through the ZIF membrane was reported to be around $5 \pm 0.2\ x10^{-6} \frac{kmol}{kPa*m^2*s}$ at 50% RH and 40°C.

Another example of the in-situ growth of zeolite crystals was explored by Xing *et al.* The Zeolite-Imidazolate Framework crystals were seeded on top of a 30 μm porous nickel support, creating a three μm thin film layer, as seen Figure 13. This formation resulted in a water/air separation factor of 300 and water permeance of $6.8x10^{-6} \frac{kmol}{kPa*m^2*s}$ at 90% RH and at 32°C [65].

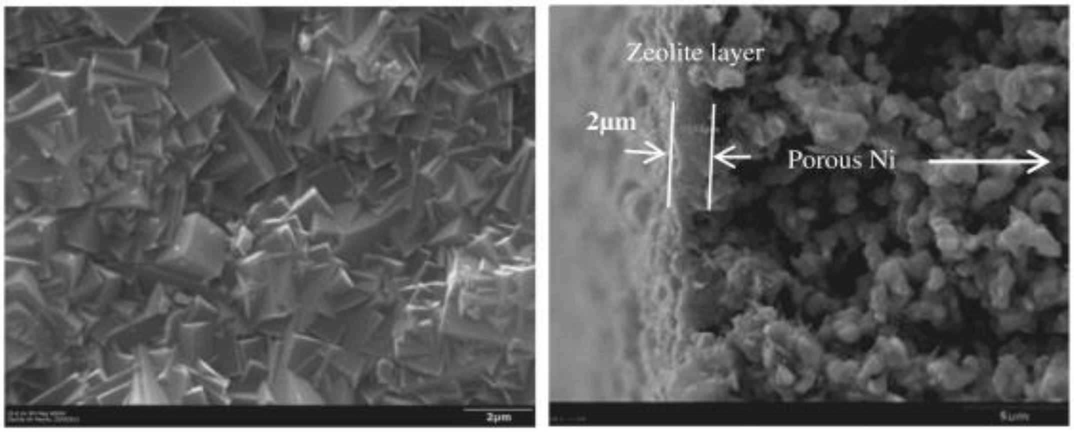

Figure 13 - Zeolite crystal growth on porous nickel support SEM image [65]

Cheng *et al.* incorporated Hollow-ZIF-8 nanospheres into the matrix of sodium alginate for dehydration of ethanol. The HZIF-8 membrane displayed a pristine crystalline structure with a void fraction of 0.705 and a contact angle of 40 to 45°, showcasing strong hydrophilic properties. The flux was measured using 90 wt.% ethanol at 75 ℃. Under these conditions, a water flux of 2136 g/m^{2}h was reported. The thermal stability of the HZIF-8 membrane suggested it as a suitable candidate for hot and humid climates with showcasing the ability to remain thermally stable up to 170 ℃. The HZIF-8 showcased great promise for the application of dehumidification through the promise of ethanol/water separation. With a high void fraction and low contact angle, a commendable permeability is attained. The morphological analysis showed a 450 nm pristine crystalline layer and visible pores, as seen in Figure 14 [17].

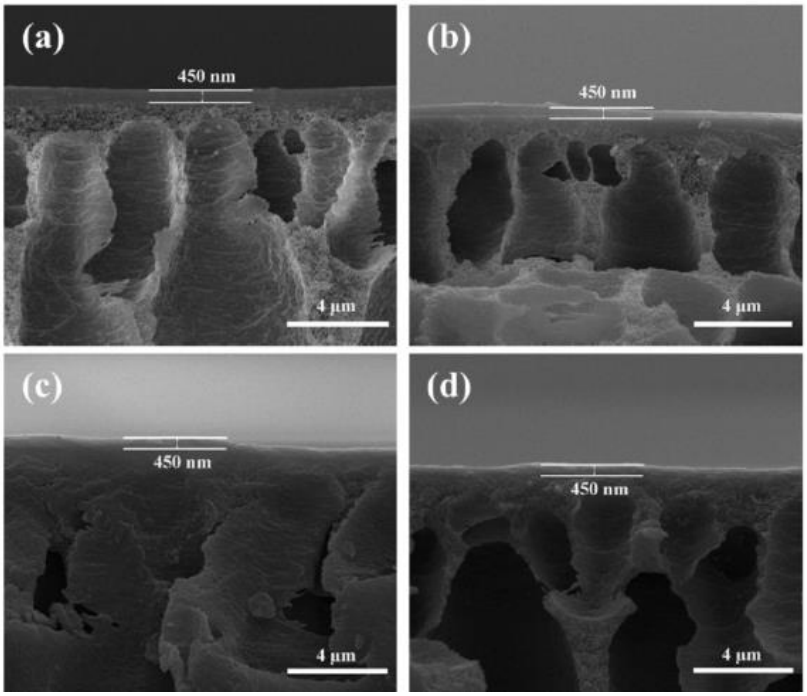

Figure 14 - Cross-section imaging of hollow HZIF-8 membrane [17]

Using TiO_2 nanoparticles as fillers in MMM has been used before and discussed in this literature review. However, Baig et al. investigated using carboxylated TiO_2 in a thin film nanocomposite HF membrane. As this application was not for dehumidification but the dehydration of flue gas, several tests were conducted to remove water from nitrogen. Moreover, the modifications to fillers and their impactful performances on polymeric membranes and their composites can be analogized to other fillers. Baig et al. carboxylated TiO_2 in a reflux condenser and washed the solution with DI water after separation from centrifugation. The carboxylated $TiO2_2$ fillers were mixed in the polyamide membrane, then interfacial polymerized with a PS membrane. The membrane yielded a mean size of 200 nm or 0.2 µm with a contact angle as low as 48 and high as 64. The permeance of the membrane was as high as 1340 GPU, and the selectivity was around 486. These tests were conducted a 30℃ with a feed flow rate of 1 liter per minute.

Where organic-inorganic composites are concerned, Song et al. studied the effect of polyester resin as a surface coating on an alumina membrane for water-air separation. The study was specific to investigating the permeation ratio and permeability of varying concentrations of the surface coating. The membrane performed consistently across 0 to 100% of relative humidity at 30℃. With the peak permeability at 60% relative humidity being about $1.3x10^{-3}$ g/min. The study fails to investigate the morphology or other aspect of the membrane; however, it does provide inside on polymeric coating and its effects. It is to be noted the permeation ratio peaked around 50% relative humidity and then declined. This may be due to the active sites of the coating being covered with the permeate decreasing its effectivity [66].

Table 5 - Organic-inorganic hybrid air-dehumidification membrane summary table

Membrane Details	Configuration	Testing Details	Morphology	Fabrication Technique	Performance			Ref.
					Permeance	Permeability	Selectivity	
ZIF-8 in Silica Alumina Support	Zeolite Imidazolate framework on Support	T: 40 °C P: 1 Bar RH: 50%	N/A	In situ formation Hydrothermal Solvosis Zeolite Crystal growth Silica – Alumina support	N/A	Water: 5x10^{-6} mol/(Pa-m^2-s) Air: 3x10^{-9} mol/(Pa-m^2-s)	H_2O/N_2 >1500	[64]
SA-HZIF-8/PAN & SA-ZIF-8	Metal-Organic Framework – Polymer Composite	T: 75 °C	Crystalline structure Free volume: 0.641-0.705 Contact Angle: About 40-45 ° Thermal Degradation: 170 °C	HZID-8 prepared through ultrasonic treatment. Substrate: Spin-casting SA solution on PAN substrates. Composite: Interfacial Synthesis via Cross-linking	N/A	SA-HZIF-8/PAN: 2458 g/m^2h SA-ZIF-8: 2136 g/m^2 h	H_2O/N_2	[17]
ZIF-8 in Nickel Support	Thin Sheet Zeolite Membrane	T: 32 °C RH: 90%	N/A	In Situ Formation Hydrothermal Solvosis Nickel Support	20042 GPU	6.8x10^{-6} mol m^{-2} Pa^{-1} 0.51 kg/m^2h	H_2O/CH_3OH 300	[65]
Carboxylated TiO_2 filler in TFN on PSF	Mixed Matrix Membrane - Polymer Composite	T: 30 °C P: N/A RH: N/A Flowrate: 1 LPM	Mean pore size: 0.2 µm Thickness: 200 µm Contact Angle: 64 to 48° OD: 1400 µm ID: 1000 µm	Carboxylation of TiO2: Condenser Reflux Composite: Interfacial Polymerization	1340 GPU	N/A	H_2O/N_2: 486	[67]
TFN – ETS - 3 Engelhard titanosilicate-4	Composite Membrane	T: 30 °C P: 2 Bars RH: N/A Flowrate: 1 LPM	Contact angle: 56 to 59°	Interfacial Polymerization	1377 GPU	N/A	H_2O/N_2: 346	[68]
Polyester - Dichloromethane Composite on Alumina Support	Composite Supported on Inorganic Substrate	T: 10-60 °C P: N/A RH: 0-100% Flowrate: N/A	N/A	Composite: Dichloromethane membrane coated with Polyester resin Alumina Membrane used as a substrate	N/A	0.0013 g/min	H_2O/Air	[66]

2.7 Polyether amide Membranes

Poly(ether-block-amide) or PEBAX® are thermoplastic elastomers containing rigid polyamide segments that act as crosslinks to the soft and flexible polyether segments. The polyether segments act as entropic springs, lowering the glass transition temperature below the room temperature. The application of Pebax varies from the different applications based on the chemical composition of the polymer, which determines the physical and chemical properties. These applications can vary from medicine, sporting goods, automotive industry, fragrance carriers, and breathable structures. The hydrophilic Pebax resins, which allow the fabrication of breathable structures, have also been shown to be promising in separating light gasses [69]. A few of these breathable Pebax structures are commonly known as Pebax 1074, 1657, and 2533. The structures and content of hydrophilic functional groups such as ether, amine determine their hydrophilicity [70, 71].

Table 6 - Polyether and polyamide content in various grades of breathable Pebax

Grade of PEBAX®	**Polyether phase**	**Polyether content (wt.%)**	**Polyamide phase**	**Polyamide content (wt.%)**	**Ref.**
PEBAX® MH 1074	$–(CH_2–CH_2–O)_n$-poly(ethylene oxide)	55	$–(NH–(CH_2)_{11}–CO)_n$-polyamide 12	45	[69]
PEBAX® MH 1657	$–(CH_2–CH_2–O)_n$-poly(ethylene oxide)	60	$–(NH–(CH_2)_5–CO)_n$-polyamide 6	40	[70]
PEBAX®2533	$–(CH_2–CH_2–CH_2–CH_2–O)_n$-poly(tetramethylene oxide)	80	$–(NH–(CH_2)_{11}–CO)_n$-polyamide 12	20	[70]

For instance, the use of Pebax membranes in dehydration rather than dehumidification was explored by Sijbesma et al. [20]. They utilized block copolymerization of sulfonated polyether ether ketone (SPEEK) for water removal from flue gas. SPEEK, SPES, and Pebax are commercially available polymeric materials that have shown outstanding performance in selectivity and permeability, as shown in Figure 15. The SPEEK polymer was compared with commercial Pebax 1074 by comparing the permeability of water in both instances and the rejection of nitrogen. The resulting permeability of water reported for SPEEK and Pebax 1074 membranes were $4.9x10^5\ Barrer$ and $2x10^5 Barrer$, respectively. Which translates to $1.45x10^{-10}\ \frac{kmol*m}{KPa*m^2*s}$ and $6.7x10^{-11}\ \frac{kmol*m}{KPa*m^2*s}$ without considering the thickness of the membranes. The 12 cm^2 membranes were tested under 2.5 bars of pressure and at 50°C, with a flowrate of $1.5x10^6\ \frac{m^3}{hour}$ at standard temperature and pressure. Validation with field tests yielded good promising results as well [20].

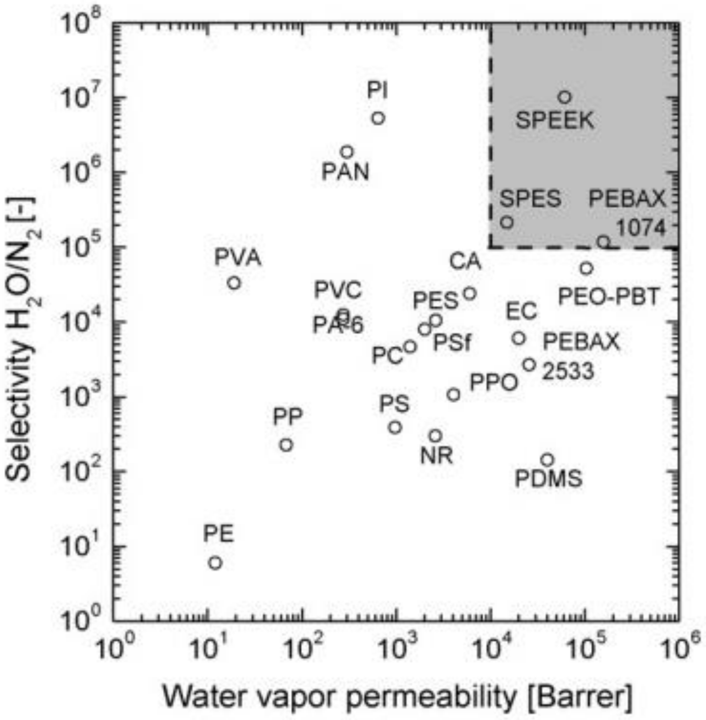

Figure 15 - Selectivity and water permeability performance of commercial polymer adapted from Sijbesma et al. [20]

A study on gas separation undertaken by Rahman et al. focused on the effect of polyethylene glycol-polyoctahedral oligomeric silsesquioxanes (PEG-POSS) in matrices of Pebax 1657 and 2533 for gas separation. The focus component was mainly on carbon dioxide separation from air, oxygen, methane, and hydrogen. Due to the addition of PEG-POSS in the matrix, the diffusion and solubility coefficients for carbon dioxide increased, as seen in Figure 16. As a result, the selectivity of carbon dioxide to nitrogen, oxygen, methane, and hydrogen also increased [71].

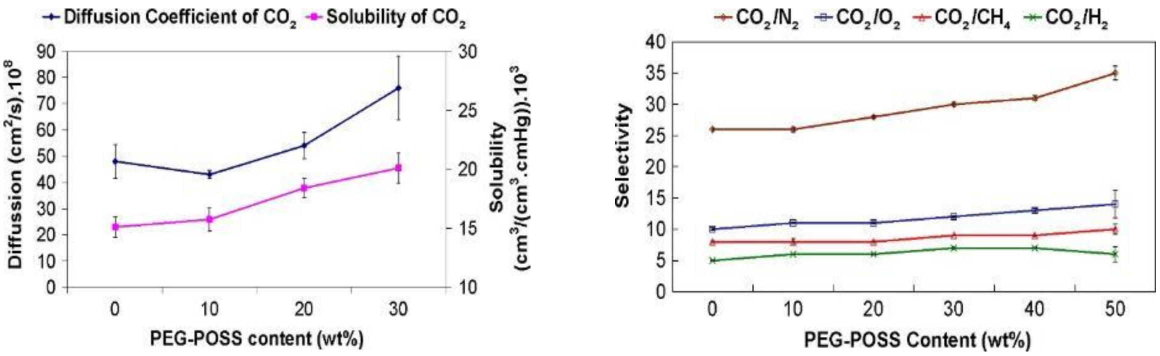

Figure 16 - Effect of PEG-POSS in Pebax matric for carbon dioxide separation [71]

Topography study of pristine Pebax 1657, depicted in Figure 17, showed the maximum roughness to be around 182 nm, with the square root mean roughness around 18.1 nm. Moreover, with the addition of 30 wt.% PEG-POSS, the maximum roughness and square root mean roughness of the mixed matrix increased to 304 and 43.6 nm, respectively [71].

Another gas sweetening study was carried out by Aziz et al., where they used Pebax 1074 as a matrix to incorporate various fillers with a focus on TiO_2, SiO_2, and Al2O3. The membranes were fabricated via solution casting using a 6 wt.% Pebax concentration. The permeability of CO_2 increased from 110 Barrer to 147, 152, and 162 for the 8 wt.% nanoparticle loading of TiO_2, SiO_2, and Al2O3, respectively. The general increase in loading led to an increase in the permeability of CO_2. Similarly, the selectivity of CO_2/CH_4 also increased from 11.09 for neat Pebax to 13.18, 12.28, and 14.24 for 8 wt.% loadings of TiO_2, SiO_2, and Al_2O_3, respectively [72].

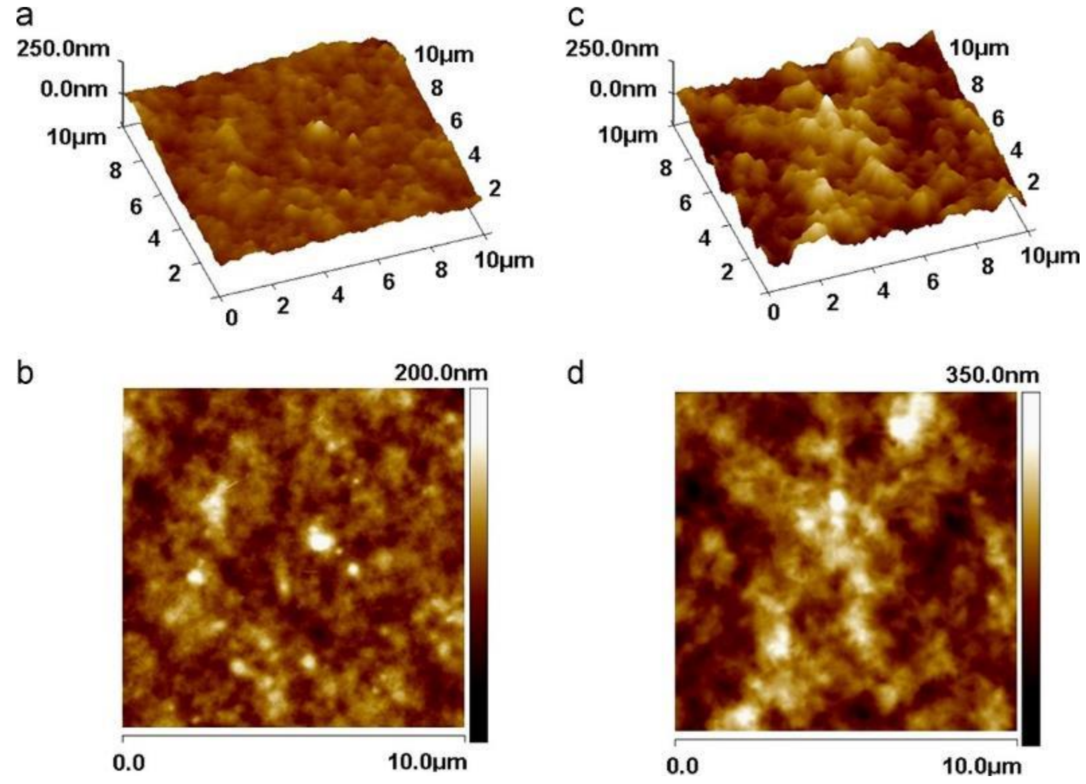

Figure 17 - AFM analysis for roughness on a&b) 3D and 2D scans on pristine Pebax, c&d) 3D and 2D scans on 30 wt.% PEG-POSS/Pebax MMM [71]

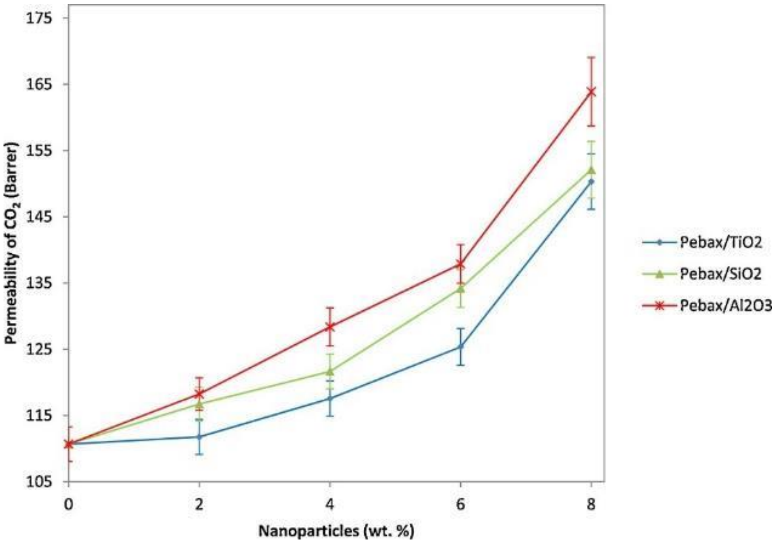

Figure 18 - Permeability of carbon dioxide with the loading of various nanoparticles [72]

In the morphological analysis, it was visible, as shown in Figure 19, that a good distribution of nanoparticles (TiO_2) was present in the cross-section imaging via FE-SEM. The balanced and well-dispersed nanoparticles are why the nanoparticles' loading helped the permeability and selectivity of the membranes [72].

In addition to other Pebax and gas sweetening studies, Sridhar et al. investigated the effect of 4A zeolite loading in Pebax 1657 mixed matrix membranes for gaseous separations. The membranes were fabricated via solution casting with various loadings from 5 to 30 wt.% in an ethanol/water solvent. With the loading of 4A zeolite, the permeability of carbon dioxide was enhanced from 71.4 to 155.7 Barrers, whereas methane’s permeability was enhanced from 2.2 to 19.6 and oxygens from 5.8 to 17.9. The ideal loading resulted in 10 wt.% of zeolite, improving carbon dioxide/methane selectivity from 54.1 to 94.2 [73].

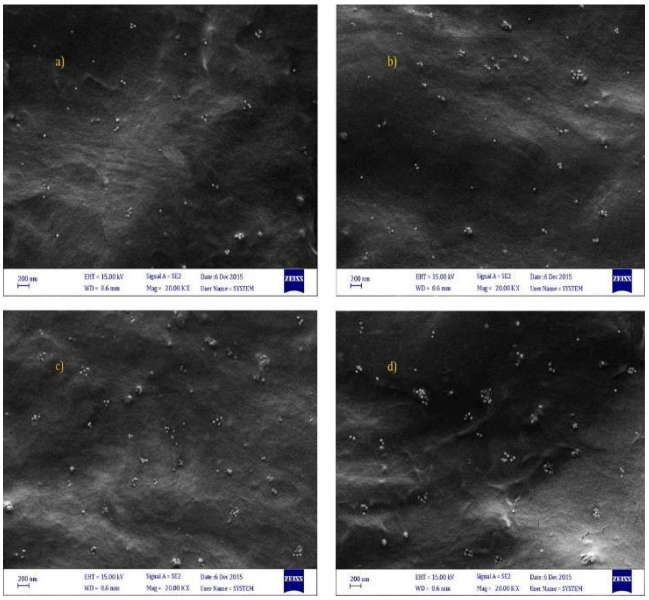

Figure 19 - Cross-section imaging of Pebax mixed matrix membranes with 2, 4, 6 & 8 wt.% loading [72]

Table 7 - Summary table of polyether amide membranes used for gas separation

Membrane Details	**Configuration**	**Testing Details**	**Morphology**	**Fabrication Technique**	**Performance**		**Ref.**
					Permeability	**Selectivity**	
PEBAX 1074 - Sulfonated PEEK	Block Copolymer Composite	T: 50 °C, P: 1 bar RH: 0-60% 1.5×10^6 STP/hr	N/A	Sulfonation of PEEK and PEBAX 1074	SPEEK: 490000 Barrer PEBAX 1074: 200000 Barrer	Water/Flue Gas	[20]
Pebax 1657 - 30 wt.% PEG-BOSS	Mixed Matrix Membrane	T: 30 °C P: 1 Bar	Roughness Max: 182 nm R-Square Mean: 18.1 nm	Solution Casting	150 Barrer	CO_2/N_2: 50	[71]
Pebax 2533 - 30 wt.% PEG-BOSS	Mixed Matrix Membrane	T: 30 °C P: 1 Bar	Roughness Max: 182 nm R-Square Mean: 18.1 nm	Solution Casting	300 Barrer	CO_2/N_2: 30	[71]
Pebax 1074 - TiO_2	Mixed Matrix Membrane	T: 30 °C P: 1 Bar	N/A	Solution Casting	Pebax: 110 Barrer 8 wt.% TiO_2: 147 Barrer	CO_2/N_2 Pebax: 11.09 8 wt.% TiO_2: 13.18	[72]
Pebax 1074 - Al_2O_3	Mixed Matrix Membrane	T: 30 °C P: 1 Bar	N/A	Solution Casting	8 wt.% Al_2O_3: 162 Barrer	CO_2/N_2 Pebax: 11.09 8 wt.% Al_2O_3: 14.24	[72]
Pebax 1074 - SiO_2	Mixed Matrix Membrane	T: 30 °C P: 1 Bar	N/A	Solution Casting	8 wt.% SiO_2: 152 Barrer	CO_2/N_2 Pebax: 11.09 8 wt.% SiO2: 12.28	[72]
Pebax 1657 - 4A Zeolite	Mixed Matrix Membrane	T: 30 °C P: 1 Bar	N/A	Solution Casting	CO_2: 155.7 Barrer CH_4: 19/6 O_2: 17.9	CO_2/CH_4 94.2	[73]

2.8 Graphene-Based Membranes

GO produced by Tour's method (Improved Hummers Method) shows enhanced performance as a separation material. Petukhov (2019) used spin-coated GO on porous anodic aluminum oxide to synthesize a membrane for dehumidification, as shown in the schematic of Figure 20.

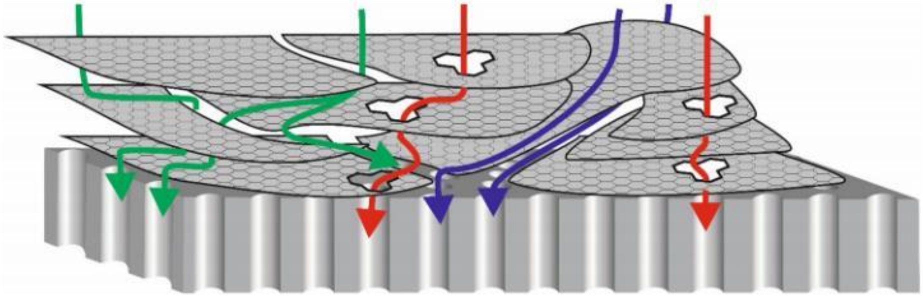

Figure 20 - Schematic drawing of GO dispersion on porous anodic aluminum oxide via spin coating [74]

Pethukhov reported excellent results for dehumidification at the most practical conditions of 80% relative humidity and nearing atmospheric pressure of about 1 Bar. Moreover, with large area membranes of 1400 cm^2 to 33000 cm^2, the ease of fabrication is highlighted with the possible upscaling. High selectivity of over 13000 with water permeance of 1.4 m^3/m^2hr was reported at 298 K and 1 Bar testing conditions. Pethukhov determined flake size to be a decisive factor in producing the best result, stating that medium-sized flakes of GO showcased the best performance. The morphology of the membranes was typical of that of flat-sheet membranes, with minimal roughness. The consistent pore forms visible in the cross-section predict why the membrane has good consistent performance across the membrane sheet, as seen in Figure 21 [74].

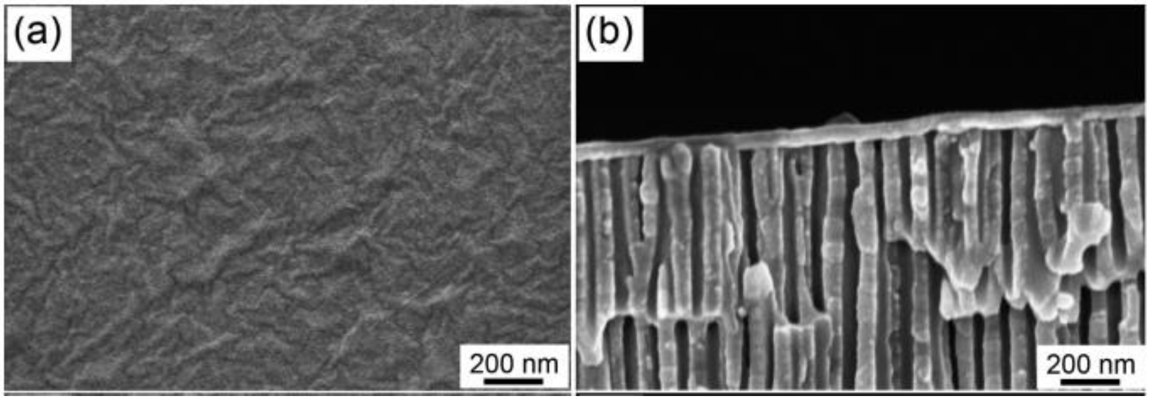

Figure 21 - Cross-sectional imaging via SEM of GO spin-coated membrane on porous aluminum oxide.

Another study of GO used as a nanofiller to enhance the properties of membranes was showcased by Baig et al., who incorporated GO and GO-TiO_2 (3:2) into polysulfone (PS) ultrafiltration membrane creating a mixed matrix membrane. The author determined the size of nanoparticles to be 70 nm using TEM and the contact angle to be around 72 for the GO-TiO_2 fillers and 53 to 88 for GO fillers. As the loading of GO increased, the contact angle decreased, causing hydrophilicity, whereas the GO-TiO_2 fillers had the opposite effect after two weight percent.

In terms of thermal stability, the initial degradation of both membrane sets was at 150 ℃, possibly due to the PS membrane. The H_2O permeance and H_2O/N_2 selectivity of both fillers were investigated. GO-TiO_2 nanofillers outshone the GO nanofillers in both categories; for selectivity, GO-TiO_2 had a higher selectivity of 910 compared to 690 of GO. For permeance, the GO-TiO_2 had higher permeance of 2820 GPU to GO fillers 2500 GPU. The varying nanomaterial concentration because of water vapor permeance was summarized in Figure 22. The permeance and selectivity were measured at 30 ℃, with the environment of the membrane completely dry before testing. The selectivity and permeability are somewhat lower than other organic and inorganic membranes, but the ease of replication and affordability of fabrication supported through characterization gives a strong validation for this work. Perhaps a study with other fillers incorporated with GO in a polymer mixed matrix could yield different promising results [67].

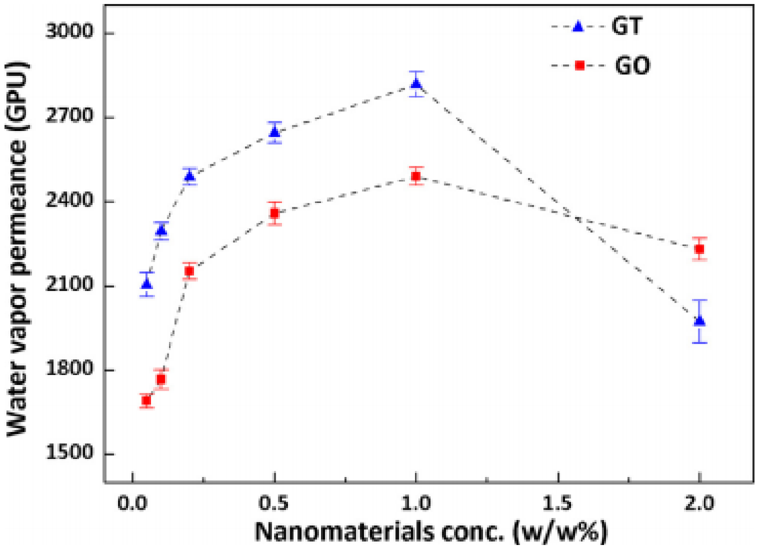

Figure 22 - Nanomaterial filler concentration of GO and TiO$_2$ in the membrane impacting water permeance [67]

Another study investigating the effect of GO in the performance of Pebax 1657-GO mixed matrix membrane (MMM) was conducted by Akhtar et al. The MMM was coated on polyacrylonitrile support with varying concentrations of GO loading from 0% to 2.0%. Moreover, two different thicknesses of a single layer and 5-layer sheets of MMM were tested. The results showed outstanding H_2O/N_2 selectivity of up to 80000 with the highest GO loading of 2.0 wt.% and 5-layer MMM. The permeability of $1.96x10^5\ Barrer$ was observed at its highest for a single layer membrane. The consequent trend between GO concentration, water permeability, and selectivity is shown in Figure 23 for 1-layer and 5-layer membranes. Despite these promising results, a further area of improvement regarding the preparation of GO could be done. Moreover, the lack of clarity of one single membrane optimal for both selectivity and permeability were missed. Hummer's method was used to synthesize GO. This outdated method produced GO with less oxygen content than the novel Tour's method, which would enhance the membrane performance [75].

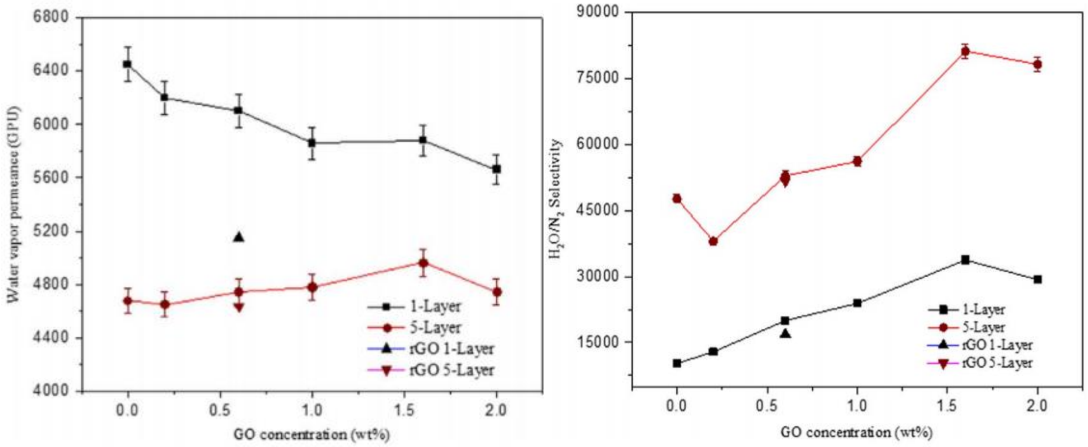

Figure 23: Effect of GO loading on permeance and water/nitrogen selectivity in single and five layers GO coating [75]

Table 8 - Graphene-based air-dehumidification membranes summary table.

Membrane Details	**Configuration**	**Testing Details**	**Morphology**	**Fabrication Technique**	**Membrane Performance**			**Ref.**
					Permeance	**Permeability**	**Selectivity**	
GO on Aluminum Oxide Support	Free Standing Membrane on Aluminum Oxide	T: N/A P: 1 Bar RH: 80%	N/A	Spin Coating and Pressure-assisted filtration	N/A	1.4 m^3/m^2h	H_2O/N_2	[74]
Pebax 1657 - GO Filler	Mixed Matrix Membrane	T: 20-35 °C Pressure: 1 Bar RH: N/A	Thermal Degradation: 150 °C	GO prepared by Hummers. Mixed matrix membranes: Dip coating of Pebax 1657	34000 GPU	196000 Barrer	H_2O/N_2 10,000 80,000	[75]
GO	Free Standing Membrane	T: 30 °C RH: 80%	Average Flake Size: 20-40 µm Membrane Thickness: 60 µm	GO: Improved Hummer's method Slurry spread out on a glass bar	1.82×10^5 GPU	N/A	H_2O/N_2 1.00×10^4	[58]
GO &GO/TiO_2 Filler - TFN on Polysulfone	MMM-Composite	T: 30 °C RH: Variable	70 nm NP, "Leaf life morphology" 669 nm roughness Contact angle GO: TiO_2-PS: 72° GO-PS: 88-53°	GO - Titanium Oxide 3:2 Ratio Composite: interfacial polymerized with Polysulfone	GO: TiO_2-PS: 2820 GPU GO-PS: 2500 GPU	N/A	H_2O/N_2 GO: TiO_2-PS: 910 GO-PS: 2500 69	[67]

2.9 Graphene Oxide (GO)

GO consists of planar sheets of graphene with the attached oxygen groups in the form of epoxy, hydroxy, and carboxyl groups on the edges and surface of the basal planes [21]. The structure of GO has been predicted to be repetitive and have a stackable nature, much like graphene and graphite. Recent studies have shown hydrogen bonding between these layers. The abundance of epoxy, hydroxy, and carboxyl groups enhances the hydrophilic properties of GO. The bonds in question to be investigated in a GO molecule can be typically found in the form of C-C, C-O, and O-C=O at 284.8, 286, and 288.5 eV, respectively in a high-resolution x-ray photoelectron spectroscopy (XPS) scan for carbon.

Similarly, for the high-resolution oxygen scan, C=O, C-O, and H-O-C peaks are commonly found at 540, 532, and 534 eV, respectively. These peaks can be shown in a typical high-resolution deconvoluted graph, as shown in Figure 24 [76]. The presence of such chemically reactive oxygen-based functional groups allows chemically functionalizing GO to enhance selected properties [77]. The existence of GO was first reported by Schafaeutl (1840), and over time the applications and synthesis techniques of GO from graphene have evolved [78]. GO has many modern-day applications, including transistors, sensors, polymer nanocomposites, and electrodes. These applications are helped by the base material graphite's excellent thermal and electrical properties [79].

2.9.1 Synthesis of GO

Brodie first introduced the chemical synthesis of GO in 1859. Brodie trained the synthesis of GO by preparing a slurry solution of graphite flakes in hot nitric acid, which is then oxidized after adding potassium chlorate [80]. In 1898 Staudenmaier improved the methodology by introducing sulfuric acid in the slurry solution, which enhanced the oxidation process. Another modification introduced by Staudenmaier was the drop-wise addition of potassium chlorate as opposed to the one-time addition. This oxidizes the graphite flakes at a higher rate [81]. In the 20th century, a revolutionary technique was introduced by Hummer (1958), which included the oxidation of graphite by potassium permanganate, sodium nitrate, and concentrated sulfuric acid. Hummer’s method was one of the most used methods for producing GO and reduced production costs. [82].

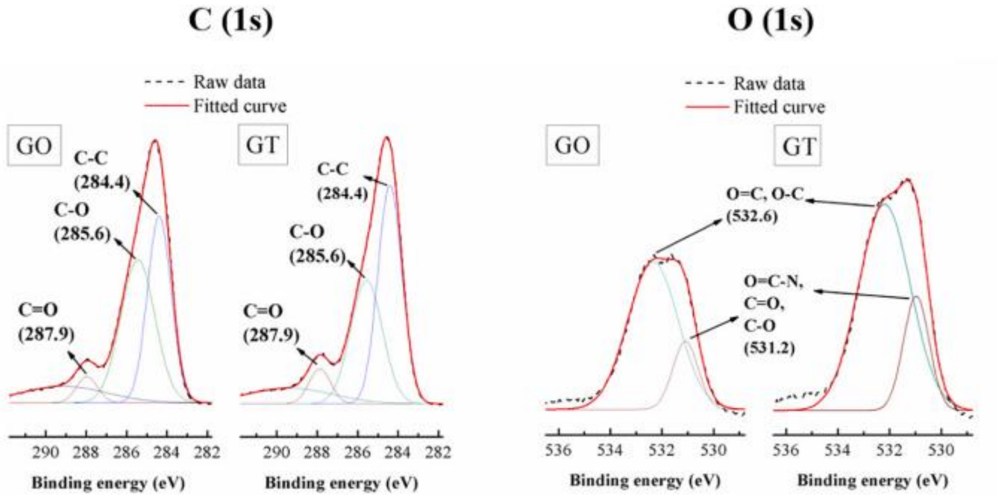

Figure 24 – High-resolution C1s and O1s scans of successfully synthesized GO [76].

The latest popular technique introduced was the improved Hummer's method, introduced by James Tour in 2010, introducing phosphoric acid instead of sodium nitrate. This change reduces the toxicity of the solution as toxic gasses such as nitrogen dioxide, dinitrogen tetroxide is released in the method introduced by Hummer, which is absent in the synthesis provided by Tour's approach. Moreover, it is also safer as combustible gasses such as chlorine dioxide are not released anymore [83]. The GO sheets' size is much larger than the Hummer's and modified Hummer's method, as shown in Figure 25.

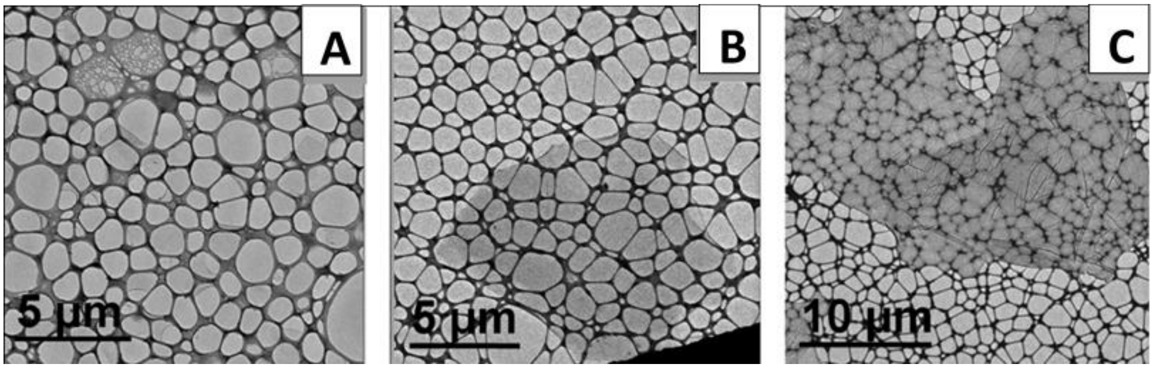

Figure 25 - Size of GO sheets produced by A) Hummer's Method B) Modified Hummer's Method and C) Improved Hummer's Method (Tour's) [83]

2.9.2 Functionalization of GO

The presence of oxygen-rich functional groups in hydroxyl, epoxy, and carboxyl groups allows the possibility of further chemically reacting GO and introducing new functional groups to enhance selected characteristics [77]. Adding fillers has proven to improve the performance of membranes; these fillers include GO and titanium dioxide. Moreover, the modifications of fillers by addition functional groups best suited for the application can improve the overall performance of the membrane. GO is a promising filler for membranes with water-based applications due to oxygen groups, improving hydrophilic properties in whichever matrix. GO can be further functionalized to enhance the properties of GO and enhance the performance of the filler.

2.9.3 Sulfonation of GO

Sulfonation of GO is a promising functionalization used to enhance the hydrophilicity of GO. The sulfone group consists of two oxygen bonds attached to sulfur between two different alkyl groups. The introduction of two oxygen bonds replacing a hydroxyl bond holds the potential to improve the hydrophilicity as the sulfone groups have more sites for hydrogen bonding to occur. Sulfonation of GO can be done in various ways; the three methodologies found in the literature were a) reacting GO with sulfanilic acid and sodium nitrate after reducing GO by sodium borohydride, b) reacting GO with sulfuric acid and methanol, and c) reacting GO with sulfanilic acid in a mixture with N-Hydroxy succinimide (NHS), 1-Ethyl-3-(3-dimethyl aminopropyl) carbodiimide (EDC) and Hydrochloric Acid (HCl).

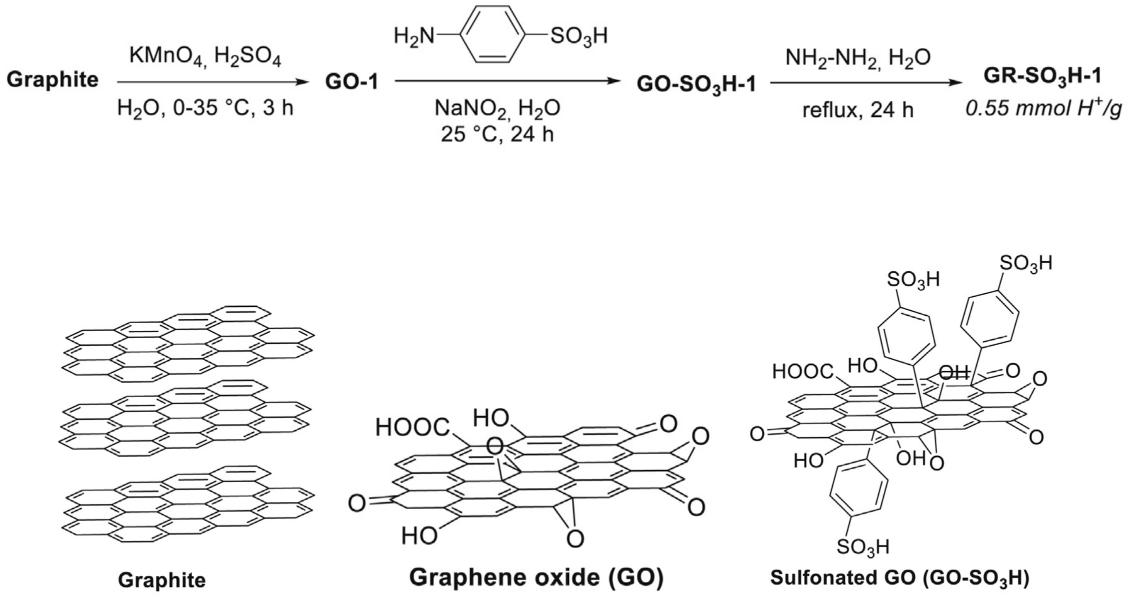

Figure 26 - Grafting of sulfanilic diazonium salt on GO adapted from Oger [76]

The reaction of GO with sulfanilic acid and sodium nitrate in the presence of sodium borohydride is the most popular and successful method for the sulfonation of GO. The mechanism of this sulfonation technique can be simplified to the grafting of the diazonium salt on the carbon ring. The sulfanilic acid and sodium nitrate make the diazonium salt, and the borohydride helps open the carbon rings and attach the sulfonate group. Typically, the dry GO solid is dissolved in water and sodium borohydride and is sonicated at a high frequency to separate the GO sheets. Next, the diazonium salt is mixed in 1M hydrochloric acid and is also sonicated. Later the GO solution and diazonium salt are mixed and sonicated at low temperatures, then left for mixing or bath sonication for 12 hours. In some instances, it was uncommon to find the addition of diazene dropwise over 3 hours. A schematic of this reaction can be seen in Figure 26 [84-86]. Although this process returns sulfonated GO, the initial step to reduce GO reduces the potential hydrophilicity. In a study by Oger et al., the sulfonation without sodium borohydride yielded a more hydrophilic product. Therefore, this should be the recommended methodology for the requirement of high water permeance [76].

The second methodology frequently used for the sulfonation of GO can be shown in work published by Kang et al. The reactants of 15mL of 0.5M sulfuric acid were mixed with 20mL of methanol to react with 1g of powdered GO. Next, the mixture was sonicated for 1 hour and was left to dry. The simplistic procedure grants much praise for this methodology as it promises repeatability and eventual upscaled production [87]. However, this methodology has demonstrated low yields of sulfonation.

A third methodology is described by Zhang *et al*., who utilized sulfanilic acid to sulfonate the GO. Zhang et al. followed a procedure where 200mg of GO was dissolved in dimethylformamide (DMF) and sonicated for 3 hours. In the mixture, 0.68 g of N-Hydroxy succinimide (NHS, 1.15 g of a 1-Ethyl-3-(3-dimethyl aminopropyl) carbodiimide (EDC) and Hydrochloric Acid (HCl) mixture were added and stirred for 2 hours. After the stirring was complete, 0.76g of sulfanilic acid was added and left to react for 24 hours. The entire process was done at room temperature. It did not use a lot of extreme temperatures or pressures, albeit the use of several reagents makes it a complex process to replicate. [88].

Several analysis techniques can be used to determine the success of sulfonation of GO, such as X-Ray Photoelectron Spectroscopy, X-Ray Diffraction (XRD), and Fourier Transform Infrared (FT-IR) and Raman scan. To confirm the successful sulfonation by XRD, Vinothkannan *et al.* and Brahmayya *et al.* showed that the peak shift could determine a successful sulfonation of GO. Initially, the GO is shown to have a peak at ~ 12.7 (2θ), whereas the sulfonated GOs peak occurs later after 26.5 (2θ). The XRD pattern of both substances will indicate possible sulfonation. Moreover, via XPS, a successful sulfonation can be determined in the atomic percentage of sulfur determined by elemental analysis of the scanning electron microscope's energy-dispersive x-ray spectroscopy analysis. A significant atomic percentage of sulfur indicates successful sulfonation. Brahmayya et al. reported 8.2%. Another aspect of XPS that can be used to determine the success of sulfonation can be described by Zhang et al., where the XPS showed a peak at 167.75 eV on the survey scan, showing a presence of sulfur-2p bonding.

Moreover, bonding at 286 eV in the high-resolution carbon scan showed a CN bond and at 289 eV of C(O)N. The inclusion of these peaks broadened the peaks of the high-resolution carbon scans compared to the non-functionalized GO. It can determine if the GO is functionalized or not. With FT-IR, Kang et al. and Zhang *et al*. determined if GO was successfully functionalized. Zhang *et al.* used FT-IR analysis to confirm the peaks at 1173, 1123, and 1036 cm^{-1} which showed the presence of sulfonic groups and, therefore, a successful functionalization of GO. Moreover, with Raman scan, Kang et al. used the Raman scan to confirm the sulfonation of GO, confirming a shift in the D and G band from 1352 and 1598 cm^{-1} to 1341 and 1595 cm^{-1}. The high Id/Ig ratios of 0.997 and 0.999 of GO and SGO, respectively, show that the GO structure was not impaired.

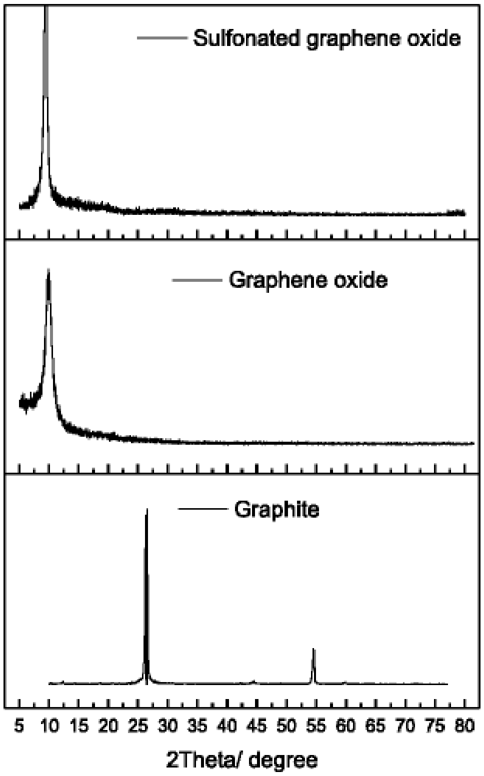

Figure 27 - Typical XRD result for GO, Functionalized GO, and Graphite [76]

2.9.4 Amine functionalization of GO

The functionalization of GO with amine groups introduces the possibility of adding nitrogen atoms, which should increase GO's hydrophilicity as water can form hydrogen bonding with oxygen and nitrogen. Several methods and materials containing amine groups can help with the functionalization of GO. These include but are not limited to various forms of urea and polyamines.

Amine functionalization of GO by urea has succeeded in enhancing the hydrophilic properties of GO. A method used by Naser et al. entailed dispersing 0.5 g of GO in DMF followed by sonication for the separation of the GO sheet separation. 0.6 g of 10 mM of urea was added shortly after, and the solution was sonicated at a high frequency for 30 mins for better initiation [89]. Moreover, Zheng et al. proposed a methodology where the urea was added to the GO slurry and resorcinol, which is left for stirring until a homogenous solution is achieved. Next, a dropwise addition of hydrochloric acid was followed until the solution pH was between 2 or 3. The solution was then reacted at 60 °C for 3 hours [90].

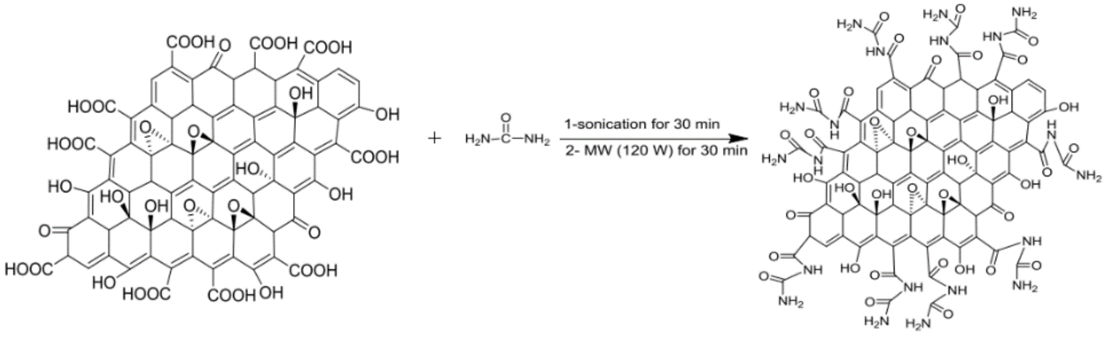

Figure 28 - Chemical Reaction of GO Reaction to form Amine-Functionalized GO, adapted from Naser et al. [89]

Another methodology of adding amine groups to GO consisted of adding polyamines. Xu et al. (2010) report their method synthesizing poly dopamine-GO functionalization by adding mg dopamine hydrochloride to 100 mg solid GO in 200 mL of 10 mM tris-Cl solution. The solution was followed by ultrasonication to separate the GO sheets and then reacted at 60 degrees Celsius for 24 hours [91].

Identifying the functionalization of GO by the addition of amine groups can be determined by various analysis methods. The Raman spectra widely reported in the literature that the functionalized GO has the 2D bands at 2915.83 and 2935.05 cm^{-1} for the amine-functionalized and thiourea functionalized GO. Previously, the GO D and G bands were present at 1359.57, and 1602.48 cm$^{-1,}$ respectively which shifted back to 2340.35 and 1592.87 cm^{-1} for the amine-functionalized GO and 1349.96 and 1592.87 cm^{-1} for the urea functionalized GO.

Another technique used to analyze the functionalization of GO was the energy dispersive x-ray analysis (EDX), where about 4.27 atomic percentage of nitrogen was found in the f-GO. For Urea, the atomic percentage of nitrogen found was 4.30 %, with 3.83 atomic % of sulfur. In XRD, the amine-functionalized GO showed new peaks at 25.10 (2θ) and 24.43 for the urea-functionalized GO. Using Scherrer's equation, the calculated crystalline size of the amine-functionalized GO and urea-functionalized GO was 2.77, and 0.48 nm compared to the 7.28 nm GO crystal, proving the de-stacking of GO upon grafting [90].

2.10 Conclusions

While looking at the membrane-based air-dehumidification modules, vacuum sweep dehumidification due to its simplistic design, easy application high COP performance proved to be the best. Vacuum-based air-dehumidification modules were up to 97% efficient, providing a maximum energy savings of 26.2% compared to other modules. Moreover, high water permeance of 11900 GPU has also been reported, making it ideal for membrane-based air-dehumidification cooling (
Table 2). On the other hand, the high maintenance and specific application of proton-exchange membranes made it challenging to adapt to the purpose of air-cooling. Moreover, desiccant-based systems showed to be slightly poorer in performance, with low water removal and a comparable efficiency of 30%. However, their use of liquid desiccants is a deterrent due to the possible health issues and complexity of handling associated with the desiccants.

Next, the air-dehumidification membranes showed high permeance as the key factor, where graphene-based and Pebax-based membranes had high permeances of up to 34000 GPU. In addition, the incorporation of nanofillers such as GO enhanced the membrane's properties and, consequently, improved its performance. Similarly, the possibility of functionalizing nanofiller, such as GO, to make them more hydrophilic enhances the overall air-dehumidification performance. Thus, adding sulfone groups is highly recommended. Moreover, another alternative like functionalizing with amine groups is also an added possibility.

CHAPTER III

3. Research Objectives and Methodology

3.1 Research Objectives

This thesis aims to fabricate, characterize, and test novel polymeric air-dehumidification membranes for air-cooling applications. Both freestanding and supported composite membranes will be developed. Polyether block amide will be used as the matrix of the active layer to fabricate free-standing and supported mixed matrix membranes containing sulfonated GO as hydrophilic filler.

The following steps are executed to achieve such an objective:

1. Synthesis and sulfonation, and characterization of GO
2. Membrane Fabrication and characterization
    a) PES-MMM containing SGO.
    b) Freestanding Pebax and Pebax-MMM containing SGO.
    c) Pebax and Pebax-SGO supported on PES-MMM.
3. Performance testing under air-dehumidification conditions.

3.2 Research Methodology

The multi-step process of fabricating membranes consists of preparing the fillers, the membrane matrix, and their respective composites. Initially, GO is identified as the main filler to be investigated. GO is synthesized using the Tour's method introduced by Tour et al. GO functionalized by adding sulfone and amine groups to enhance the fillers hydrophilic properties. The GO and functionalized GO are thoroughly characterized and assessed on the success of the intended functionalization. The nanofiltration matrix of the PES membrane was prepared with various f-GO loadings. These fabricated membranes are tested for water permeance and water/nitrogen separation.

Figure 29 - Flow diagram of research methodology

3.3 Materials

To synthesize GO and sulfonated GO, 100 µm graphite flakes, 98% concentrated sulfuric acid, 95% phosphoric acid, 35% hydrochloric acid, ethanol, n-methylpyridine, potassium permanganate, sodium nitrite, and sulfanilic acid were procured from Sigma-Aldrich. Other chemicals such as 35% hydrogen peroxide and butanol were acquired from Merck Millipore. The polymer for the support membrane, i.e., PES, was supplied by Snyder Filtration in powder form. A hydrophilic grade of polyether block amide (Pebax 1074) was purchased from Arkema, the leading commercial manufacturer of Pebax.

3.4 Synthesis of GO

GO is synthesized using the improved Hummers method or Tour's method presented by James Tour et al., where about 1 gram of graphite flakes are added to a 120/13.5 mL mixture of concentrated sulfuric acid and phosphoric acid. The mixture is left to reach a natural exotherm while stabilizing the temperature around 40 °C. After the natural exotherm is reached and stabilized after approximately 60 minutes, potassium permanganate is added, producing another exotherm. Twelve hours after adding potassium permanganate and controlled temperature at 50 °C, the GO solution is cooled to room temperature before being quenched on 200 mL deionized water ice. After the solution has been quenched, hydrogen peroxide is added dropwise until the color of the solution changes. Next, the mixture is washed twice with 30% hydrochloric acid, followed by two washes of 30% ethanol. The washing with DI water, followed by centrifugation at 4000 RPM for 4 hours, continues until the pH of the supernatant reaches the DI water pH, i.e., ~7. The solution is freeze-dried for optimum use.

3.5 Functionalization of GO

The prepared GO is functionalized by grafting sulfone groups to enhance GO hydrophilicity. The sulfonation was carried out by reacting diazonium salt of sulfanilic acid and sodium nitrate, where the grafting occurs with the help of the borohydride catalyst. GO of 6 mg/mL in DI water was dissolved with 1g sodium nitrite for 280 mg GO with 800 mg of sulfanilic acid. The mixture is heated up to 60 °C and left for a reaction for 12 hours. After the reaction is complete, it is left to cool down to room temperature, and thorough washing with DI water and centrifugation is done until the pH of the solution is above 6. The sulfonated GO solution is freeze-dried.

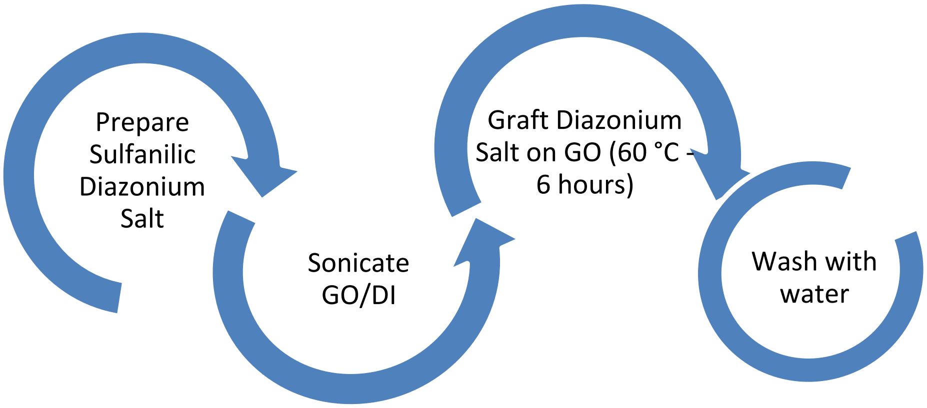

Figure 30 - Simplified process diagram of sulfonation of GO

3.6 Material Characterization

The synthesized and functionalized GO are characterized to see graphite flakes' successful oxidation and functionalized GO. The characterization techniques used to characterize the functionalized GO are discussed in the following sections.

3.6.1 Crystal Structure of GO

XRD allows investigating the complete sample throughout its volume with specific relation to the crystal structures, including the lattice spacing, the crystals' size, the crystals' orientation, and possible defects. The scan over a range of 5° to 70° at a set wavelength [92].

The XRD of the GO prepared by Trour's should have a peak at $2\theta = 11$, corresponding to the (001) plane, whereas any reduced GO would cause the peak to be broadened and shifted to $2\theta = 25$. Similarly, all functionalized GO tends to have the same initial peak (001) at $2\theta = 11$, although broadening, indicating exfoliation and smaller crystal size [92, 93].

The interplanar distance (d) known as d-spacing between the particle can be calculated by Bragg’s law which is given by:

$$2d\sin(\theta) = n\lambda \tag{11}$$

Where the lambda is the x-ray wavelength, and theta are the angle where the peak is observed. The interplanar distance of the graphite from its raw material to its form in GO should increase up to at least 7Å [94].

Moreover, the distance of the crystallite size can be found using several equations. One of these models that tend to be more accurate with organic mimicking crystals is Scherrer’s equation given by [95]:

$$L = \frac{K\lambda}{\beta\cos(\theta)} \tag{12}$$

3.6.2 Elemental Analysis of GO

X-ray photoelectron spectroscopy is an analysis technique that can identify elemental components present on the surface. XPS analysis has a limitation of only being able to characterize the sample's surface as the penetration of the x-rays is limited to 2-5 nm deep. In XPS, the sample is exposed to a continuous array of electrons with x-rays, which leads to excite the surface and, as a result, emits photoelectrons. A detector absorbed these photoelectrons, which indicated the respective binding energies associated with different elements and their respective states. A combination of such drawn an ability to quantify the elements present on the sample's surface [96].

In GO and functionalized GO, the contents may vary slightly depending on the attached functional group. In a low-resolution survey scan, a carbon C1s and oxygen O1s ratio measurement should allow for quantification. The deconvoluted higher resolution scans on the carbon C1s region and oxygen O1s region enable further investigation of which bonds are present and prove the successful synthesis of the desired product.

3.6.3 Surface and Cross-Sectional Imaging

SEM is an imaging surface characterization technique that allows analysis of the sample morphology. In addition, using energy dispersive x-ray scattering (EDX), SEM also uses electron beams under the vacuum, which bounce off the material's surface and are detected back as an image [97]. The surface structure and layering sizes can visually characterize the differences between GO and functionalized GO. Using a diluted sample of GO in a volatile solvent can visualize the lateral size of the said GO sheets. The sheet sizes of GOs successfully synthesized using Tour's method are large, therefore, more significant than 200 nm to 500 nm in size [98].

3.7 Fabrication of PES Mixed Matrix Membranes

The PES MMM are fabricated with different loading of the f-GOs. The PES solution itself consists of 17.5 weight % PES, 5 weight % PVP, and the balance of NMP. All are added and left for mixing till a homogenous solution is achieved for 48 hours. Different loadings are determined by adding f-GO over the polymer weight from 0 to 0.2% loadings, including intervals at 0.05, 0.1, and 0.15%. 15mL of each loading of f-GO is prepared and are transferred in 20mL small bottles. The f-GO – PES solution is stirred until a homogenous solution is achieved for 24 hours. The solution is then probe sonicated for 15 minutes, followed by 15 minutes of degassing.

The f-GO-PES solutions are ready to be cast. A water bath of about 1L of DI water is prepared, and a two-compartment knife of the thickness 150 µm is used. The solution is poured into the knife compartment on a clean glass plate and spread evenly using a membrane casting machine at 1 m/min speed. After 30 seconds, the glass plate is immersed into a water bath to fabricate the membranes via phase inversion. The fabricated membranes are rolled up carefully and placed in containers filled with DI water which is replaced every day for three days to ensure all pores are formed completely.

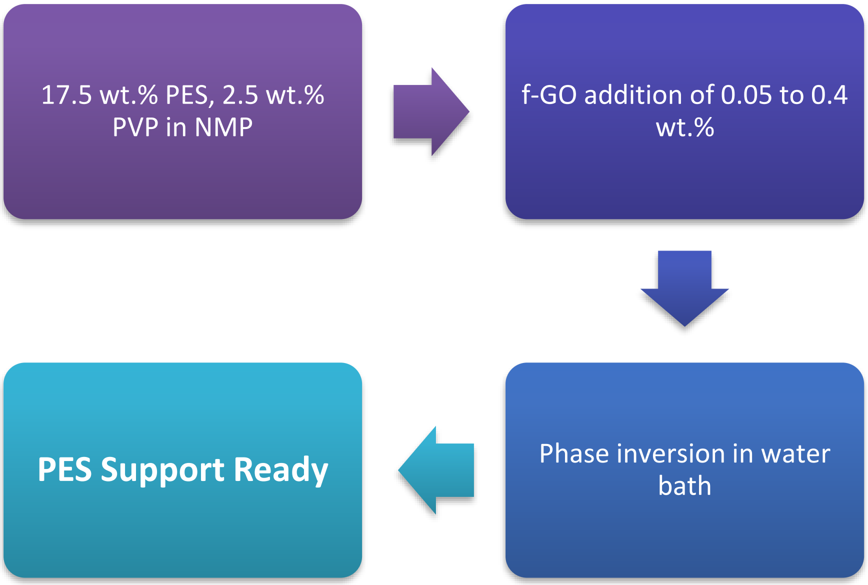

Figure 31 - Simplified process of making PES membrane.

3.8 Fabrication of Free Standing and Supported Pebax Membranes

3.8.1 Fabrication of Free Standing Pebax Membranes

Free-standing or dense Pebax membranes were prepared via solution casting. A 5 wt.% Pebax solution is prepared by drying the Pebax 1074 pellets in the oven at 60 °C for 8 hours to remove any adsorbed moisture and dissolved in butanol at 80 °C for 4 hours until a homogenous solution is obtained. Then the Pebax and S-GO/Pebax solutions are cast on a PVA-Teflon plate using a casting knife thickness of 250 µm.

3.8.2 Fabrication of Asymmetric Pebax Membranes

Using the hydrophilic grade of polyether block amine (Pebax-1074), the film composite membrane is prepared. The preparation starts with drying the Pebax 1074 pellets in the oven at 60 °C for 8 hours to remove any captive moisture. Next, the dried pellets are mixed in a 0.5-weight percent solution in a round bottom flask with 100% 1-Butanol solution are mixed under reflux at 80 °C for 4 hours until a uniform solution is obtained.

The previously fabricated mixed matrix membrane of polyether sulfone – functionalized GO is secured on a Teflon plate by taping the edges. Then, the Pebax 1074 solution prepared in butanol is air-sprayed onto the secured PES-MMM, giving it two coats. The dried result yields a composite membrane to be used for air-dehumidification.

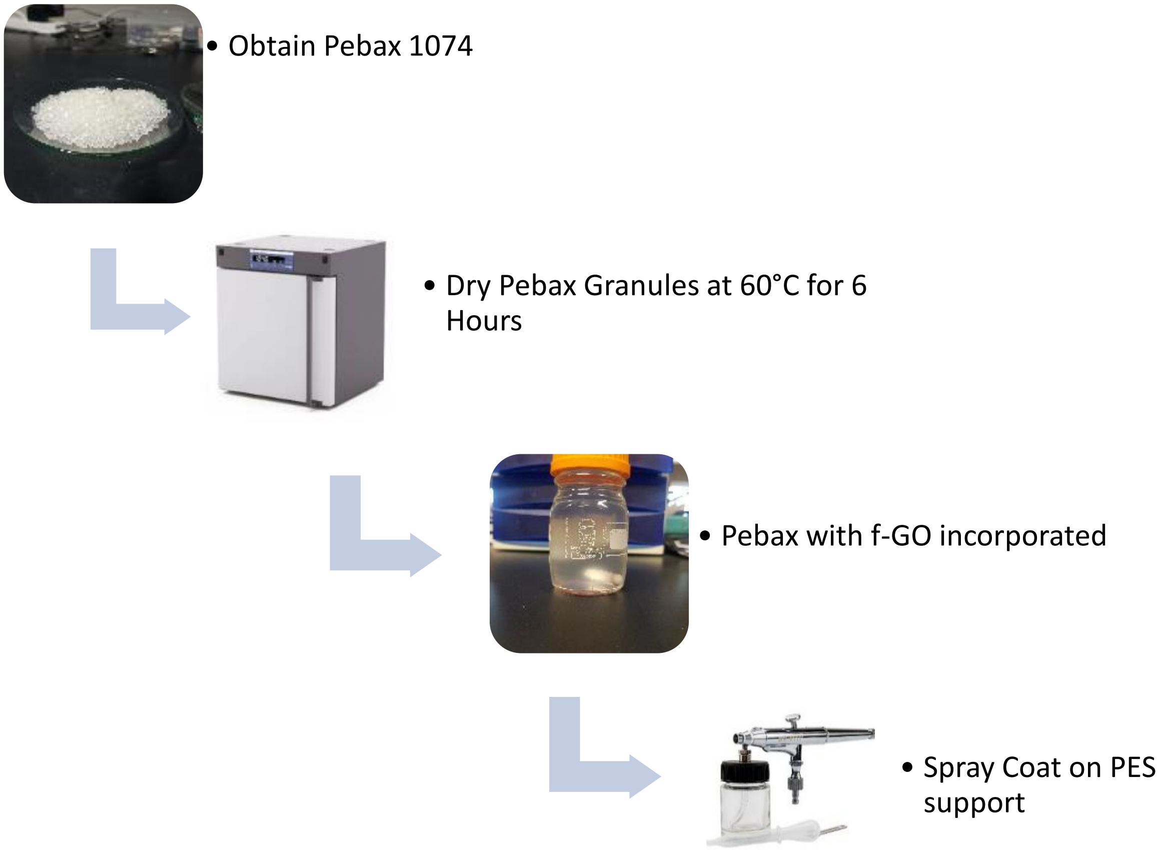

Figure 32 - Process diagram of applying Pebax 1074 on PES support to produce the TFC membrane.

3.9 Membrane Characterization

The membrane characterization is necessary to observe the morphology and characteristics of the membrane and their relation to the application. Membranes for air dehumidification require membranes with smooth surfaces, hydrophilic properties, and good mechanical properties. For these investigations, the following characterization is undertaken.

3.9.1 Membrane hydrophilicity and wettability

The contact angle measurement allows investigating the angle of a water droplet at the surface of the membrane. Hydrophilic membranes produce smaller contact angle, therefore predicting that the membrane surface is water friendly. This is an early indicator of how the membrane would result in the tests such as water permeance and fouling. The contact angle is conducted by cutting equal strips of the membrane and are attached to the microscope slide by carbon tape. The contact angle machine disperses a drop of water on the membrane surface, and a camera captures the image and the angle. The measurements are repeated for different strips, and the averages and standard deviations are calculated. A hydrophilic air-dehumidification membrane should have very low contact angle. A contact angle of 53° was obtained by incorporating GO in the polysulfone matrix [67].

3.9.2 Membrane Topography and Surface Roughness

The AFM is a technique that investigates the surface topography of the membrane. The analysis provides 3D imaging of the surface structure, which indicates how smooth the surface of the membrane is. The surface's roughness resonates with the membrane's hydrophilic properties and fouling tendencies [99].

3.10 Performance Testing

Testing the performance of air membranes is carried by measuring the water and nitrogen permeance and the corresponding selectivity.

3.10.1 Water Permeance and Selectivity

The air dehumidification performance of the membrane is tested at specific relative humidity with selected pressures of the inlet feed. The whole setup consists of an air dehumidification module with a humidity controller. The module follows the process developed by Culp [8]. The inlet air is humidified and enters the membrane cell. The membrane cell rejects the dry air, and the water vapor passes through the permeate side, which is helped by the vacuum pump, as shown in Figure 33.

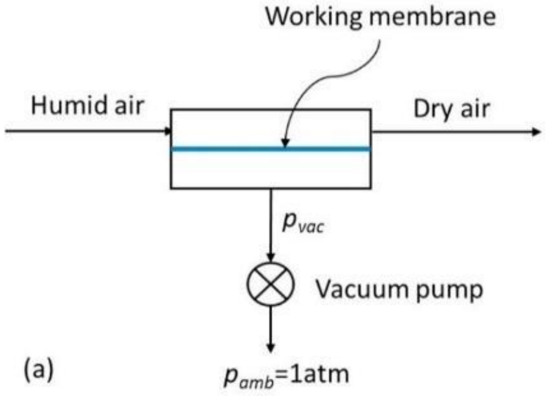

Figure 33 - Vacuum-Dehumidification set up flow diagram adapted from Bui et al [11]

The water permeance in the membrane can be calculated by the difference in the relative humidity in and permeate, respective to in inlet water content. Permeance j has the units of $\frac{mol}{m^2 sPa}$ and can be calculated from equation 5:

$$j_{H2O} = \frac{\dot{N}_{\mathrm{H2O}}}{A \cdot (\Delta P_{\mathrm{H2O}})_{lm}} \tag{5}$$

Moreover, another critical parameter that translates a membrane's performance is the separation factor between water and air, comparing the amount of water and air in the permeate side against the retentate side. This can be calculated from equation 6:

$$S = \left(\frac{\dot{N}_{\mathrm{H2O,p}}}{\dot{N}_{\mathrm{H2O},R}}\right)\left(\frac{\dot{N}_{\mathrm{air,R}}}{\dot{N}_{\mathrm{air,P}}}\right) \tag{6}$$

3.10.2 Nitrogen Permeance

Nitrogen permeance demonstrates the ability of air to permeate through the membrane sample, indicating if the separation between water and air is possible. As one-half of selectivity, nitrogen permeance can be calculated through the time-lag method while using a dead-end cell and pressure gauge.

As per the constant volume-variable time calculations, the dead-end cell connected to a nitrogen cylinder will be pressurized to 4 bars; the permeation of nitrogen over time will be noted with a closed supply. The calculations of the nitrogen permeance can be given by equation 10:

$$\bar{P}_{M_{N_2}} = \frac{V}{A}\frac{1}{RT}\frac{1}{P_t - P_p}\frac{dP_t}{dt} \quad \left[\frac{mol}{m^2.bar.s}\right] \tag{13}$$

Chapter IV

4. Results and Discussion

4.1 Characterization of GO and Functionalization of GO

4.1.1 Elemental and Chemical Composition Analysis

The elemental composition and chemical structure of GO and sulfonated GO were characterized via XPS and EDX. The quantification of the elemental composition of GO and f-GO confirms the successful synthesis and functionalization.

Table 9 provides the atomic composition of the GO synthesized via the Tour's method (GO-T) with carbon to oxygen ratio of 7:4 (63.6% C to 36.3% O). Moreover, compared to Hummer's GO (GO-H), the carbon to oxygen ratio is slightly higher, where the carbon to oxygen atomic composition is 65.1 to 34.9, respectively. The extent of sulfonation of GO in the two different methods shows a higher yield of the sulfur component when GO is reduced (SRGO), at 1.5%. In comparison to 0.3% when GO is not reduced before the sulfonation (SGO). Especially when translated into carbon to sulfur ratios, where for SRGO, the ratio is 49.066 compared to 224.67 for SGO. This shows 4.5x more functionalization when the reduction takes place. Although the extent of functionalization is much greater, a significant loss in the overall oxygen content is observed, which is counterproductive to the final goal. Especially when considering that each sulfone atom consists of 3 oxygen atoms and 1 sulfur atom. This ratio further reflects that 4.5% of the overall oxygen atomic composition in SRGO contributed from the sulfonation, leaving only 20.4% from the original GO.

Table 9 - Atomic Composition of GO, SRGO, SGO determined by EDAX

	Atomic Composition%		
Compound	**Carbon**	**Oxygen**	**Sulfur**
GO (Hummer's)	65.1	34.9	0.0
GO (Tour's)	63.6	36.4	0.0
Sulfonated Reduced GO	73.6	24.9	1.5
Sulfonated GO	67.4	32.3	0.3

Figure 34 shows the high-resolution scans of carbon and oxygen show the presence of carbon-carbon (C-C) bonds at 284.8 eV and two variants of oxygen attached to carbon in the form of C-O-C at 286.7 eV and O-C=O at 288.5 eV. Preliminarily, these show the successful synthesis of GO from graphite due to the abundance of oxygen-based functional groups attached to the carbon. Moreover, two specific groups of epoxy and carboxylic functional groups can be noted. For the oxygen spectra, oxygen attached to carbon in the form of C=O and C-O are visible at 531.4 eV and 533 eV, respectively. Additionally, this allows the estimation that a hydroxy and carbonyl group are also present.

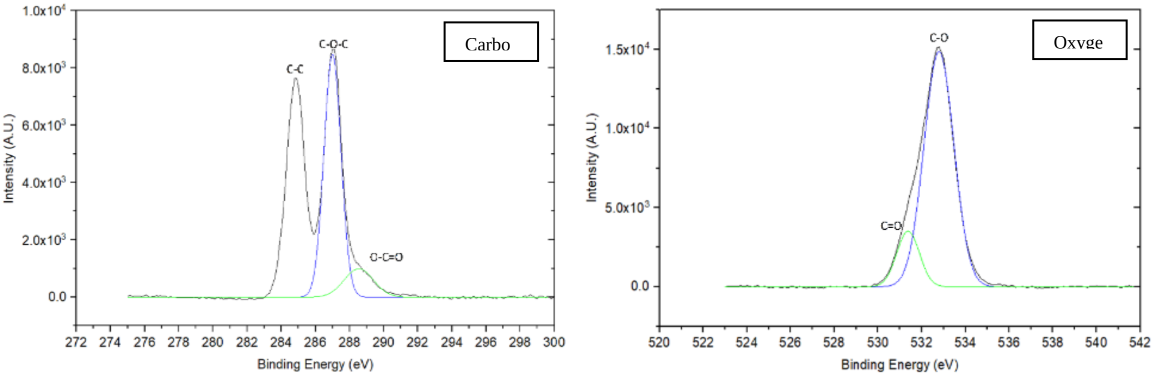

Figure 34 - Carbon and Oxygen high-resolution XPS scan deconvoluted for GO

Figure 35 provides the high-resolution carbon and oxygen spectra. The spectra of GO and fGO are similar, confirming that the skeleton structure of GO remains intact. This may also be due to the small extent of sulfonation that takes place. Besides, the high resolution of nitrogen and sulfur scans show the structure change and how the grafting of sulfanilic acid occurs. Via the high-resolution nitrogen scan, nitrogen attached to carbon as an amine group can be observed at 398 eV, whereas nitrogen attached to a phenyl group can be observed at 400.5 eV. Lastly, the presence of the nitrite group is shown at ~405 eV. The nitrile and amine groups presence show the residue of sodium nitrite and sulfanilic acid used in the synthesis reaction. However, the nitrogen attached to the phenyl ring allows us to conclude that successful sulfonation of GO has occurred. The high-resolution sulfur scan does not confirm the presence of sulfanilic acid in the sulfonated GO as sulfanilic acid is grafted onto the carbon ring.

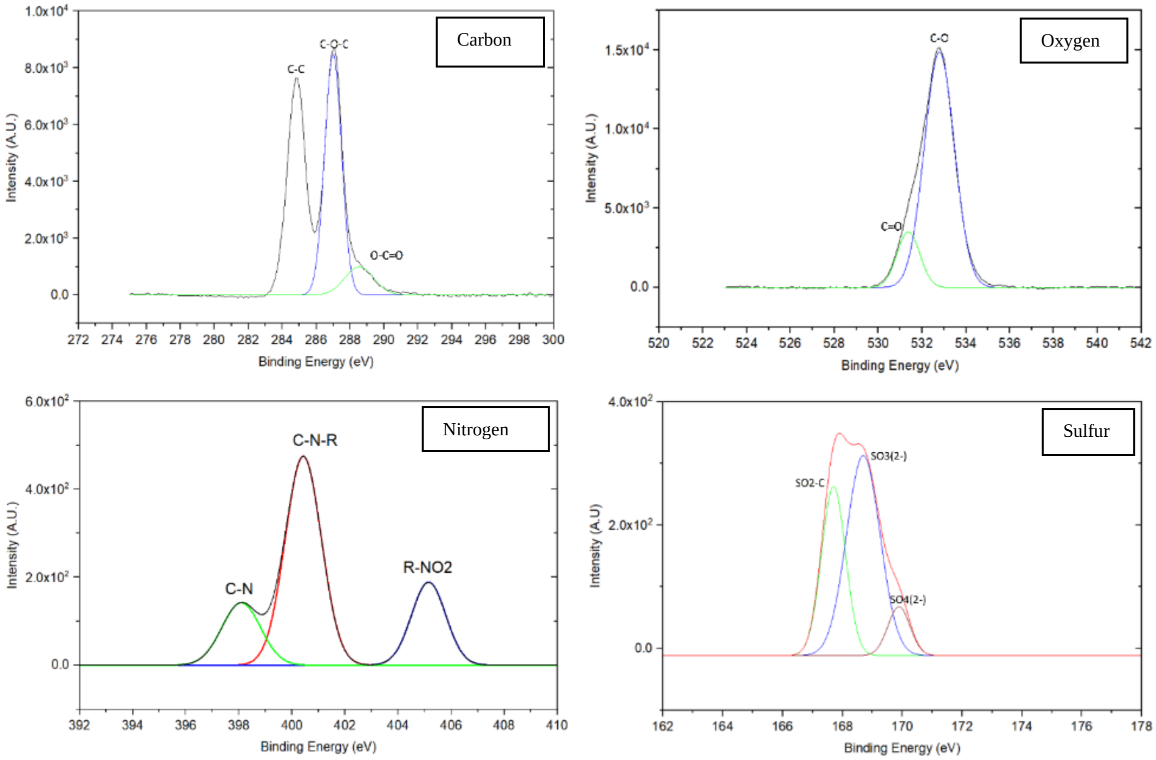

Figure 35 - Carbon, Oxygen, Nitrogen, and Sulfur high-resolution XPS scans deconvoluted for sulfonated GO

4.1.2 Crystal Structure of GO and f-GO

X-ray diffraction (XRD) is used to determine the stacking properties, d-spacing, and crystallite size. Measured in the 2θ range of 5 to 60°, the XRD patterns can be seen in Figure 36. GO (GO) shows a peak at $2\theta = 9.54$, whereas sulfonated GO (SGO) and sulfonated reduced GO (SRGO) showed a slight peak shift at $2\theta = 9.98$, and 10.18. SRGO shows peak broadening, suggesting a smaller crystallite size and a significant reduction in the material's structure. On the contrary, SGO shows an increase in peak heigh and narrowing of the peak, suggesting an increase in crystallite size.

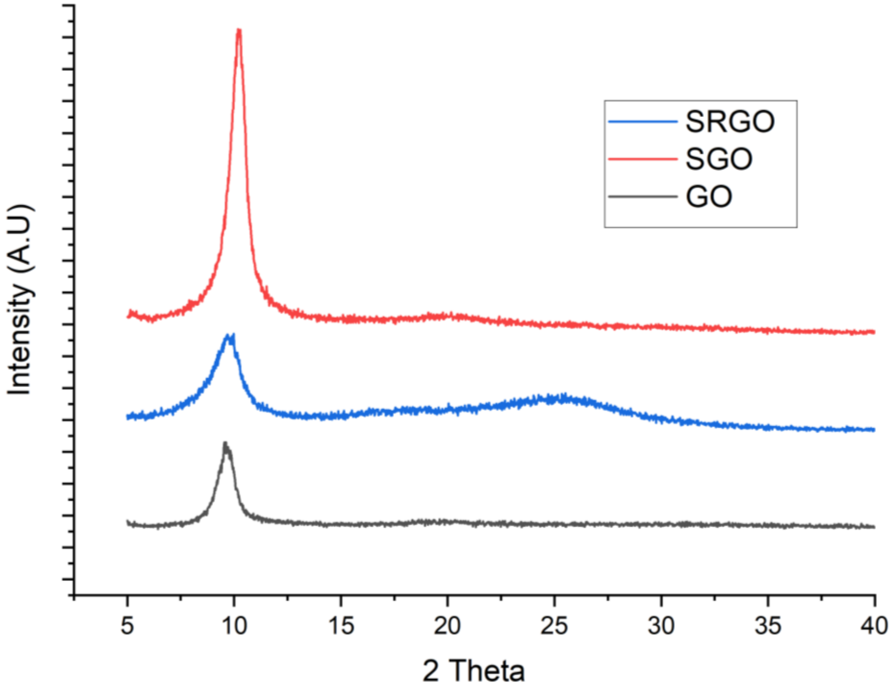

Figure 36 - XRD analysis on GO, sulfonated, and sulfonated reduced GO

The d-spacing calculated by Bragg's law (Equation 8) shows the space between two parallel planes of atoms. The computed results tabulated in Table 10 show that the d-spacing reduces very slightly when GO undergoes any sulfonation attempt. The d spacing of GO, calculated using XRD data, was 0.93 nm (9.3 Å), whereas, for SGO and SRGO, the d spacing values were 0.89 nm (8.9Å) and 0.87 nm (8.7Å), respectively.

Moreover, using Scherrer's equation (Equation 9), the crystallite size can be determined. The crystallite size is conventionally used to determine the crystallite size; however, in the case of GO and f-GO, the change in crystallite size can determine functionalization.

Scherrer's equation calculated that the increase in crystal size from 8.86 nm for GO to 9.06 nm shows that the grafting of the sulfanilic salt has been done successfully. This is also corroborated with literature results as presented by Oger et al. [84].

Table 10: The crystal structure parameters for GO and f-GO

Material	Peak Intensity at 2Theta	Corresponding Intensity	Crystal Size (nm)	d-spacing nm
GO	9.54	567	**8.86**	**0.93**
SGO	9.98	1949	**9.06**	**0.89**
SRGO	10.18	649	**4.39**	**0.87**

4.1.3 Wettability Analysis

The nanofiller's wettability properties help increase the mixed-matrix membranes' hydrophilic properties. To conduct and observe which fillers' wettability properties are superior, a contact analysis was performed. The fillers in contention include GO – Tour's (GO-T), GO – Hummer's (GO-H), sulfonated GO (SGO), and sulfonated reduced GO (SRGO).

As seen in figures Figure 37 and Figure 38 , the contact angle for GO synthesized via Tour's method shows a lower contact angle of about 5.8°. In contrast, the contact angle between the functionalized fillers shows that SRGO loses a lot of hydrophilic properties due to the reduction step and gives a high contact angle of 76.9°, which is more hydrophobic than the starting compound of GO. The increased hydrophobicity is not suitable for water permeating membranes.

On the other hand, the contact angle of SGO is 24.5°, an improvement of 13° from GO (GO-T). The addition of sulfone groups without the reduction step allows the replacement of hydroxyl groups to be replaced with sulfone groups, which helps increase they hydrophilicity greatly without a high sulfone loading. The SGO filler is ideal for water permeating membranes.

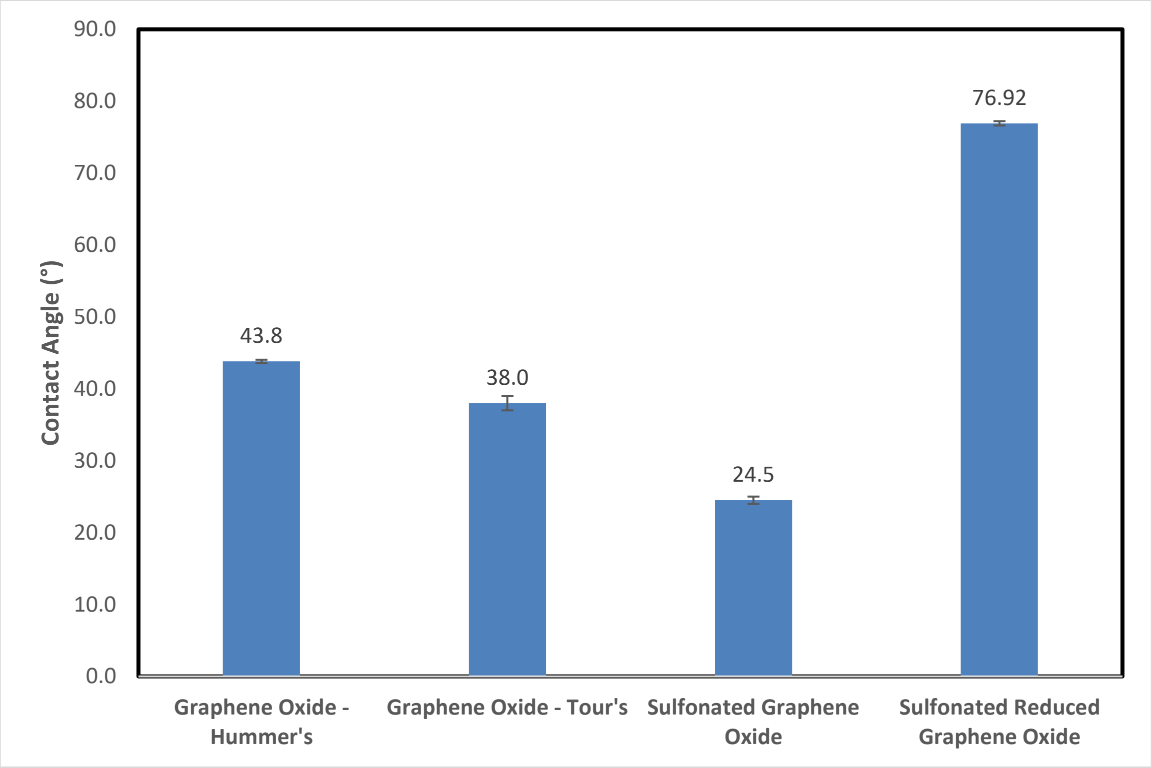

Figure 37 - Contact angle analysis for variants of GO

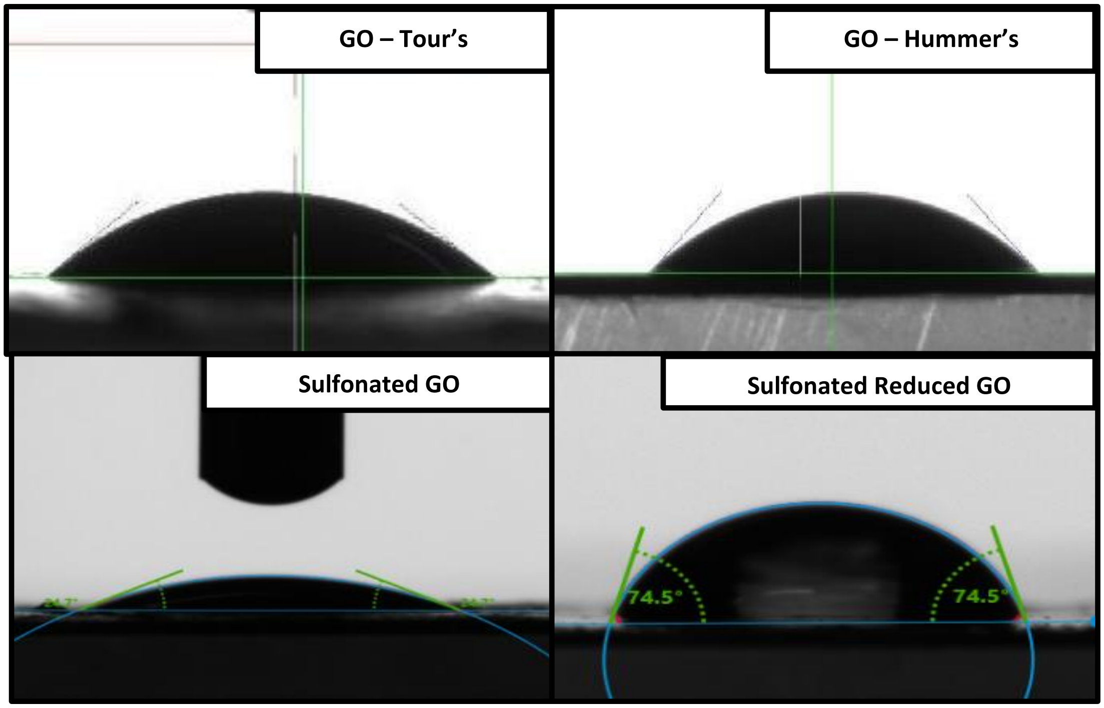

Figure 38 - Contact angle imaging of GO and functionalized GO variants

4.2 The Effect of Sulfonated GO on PES Mixed Matrix Membranes

4.2.1 Surface and Cross-Sectional Imaging

The imaging of the scanning electron microscopy shows the decrease in pore size with the addition of SGO. As seen in Figure 39, the control polyether sulfone membrane has a pore size of ~400 nm, which decreases to 200 and then 150 nm with the loading of 0.20 and 0.40 polymeric weight percent of SGO. The distribution of the pores and the overall porosity are challenging to be judged by these images.

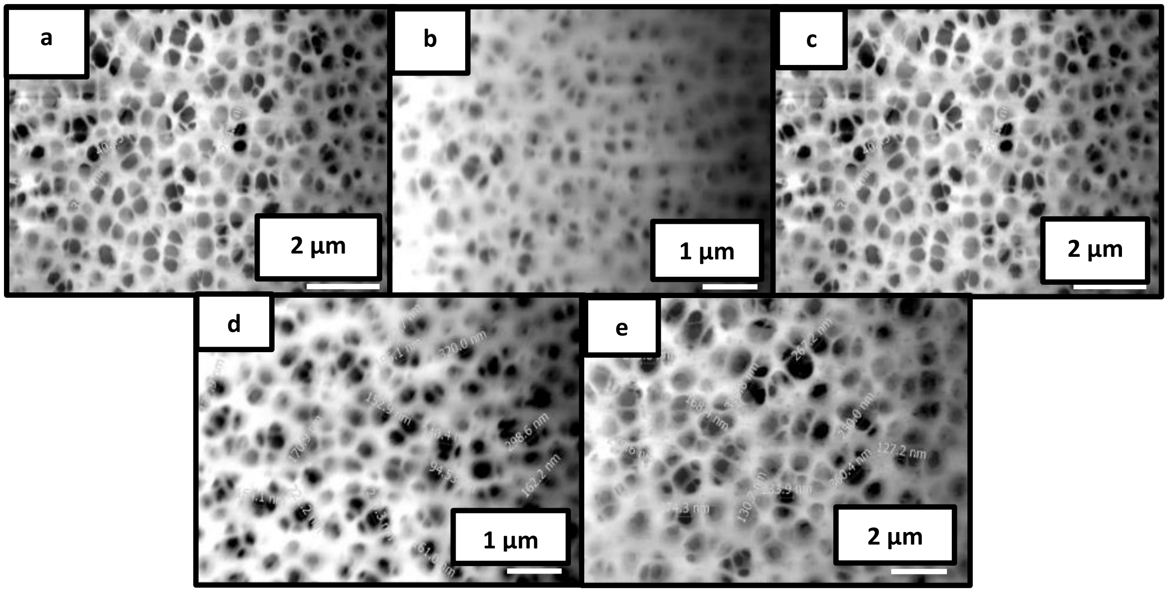

Figure 39 – Surface SEM imaging of PES mixed matrix membranes containing a) PES Control, b) 0.05 wt.% SGO, c) 0.10 wt.% SGO, d) 0.20 wt.% SGO and e) 0.40 wt.% SGO

The cross-sectional images shown in Figure 40 reveal the channels and active layer of the polyether sulfone mixed matrix membranes. Although the channel structure is not affected by the SGO loading, an increase in the thickness of the dense layer is observed with the SGO addition.

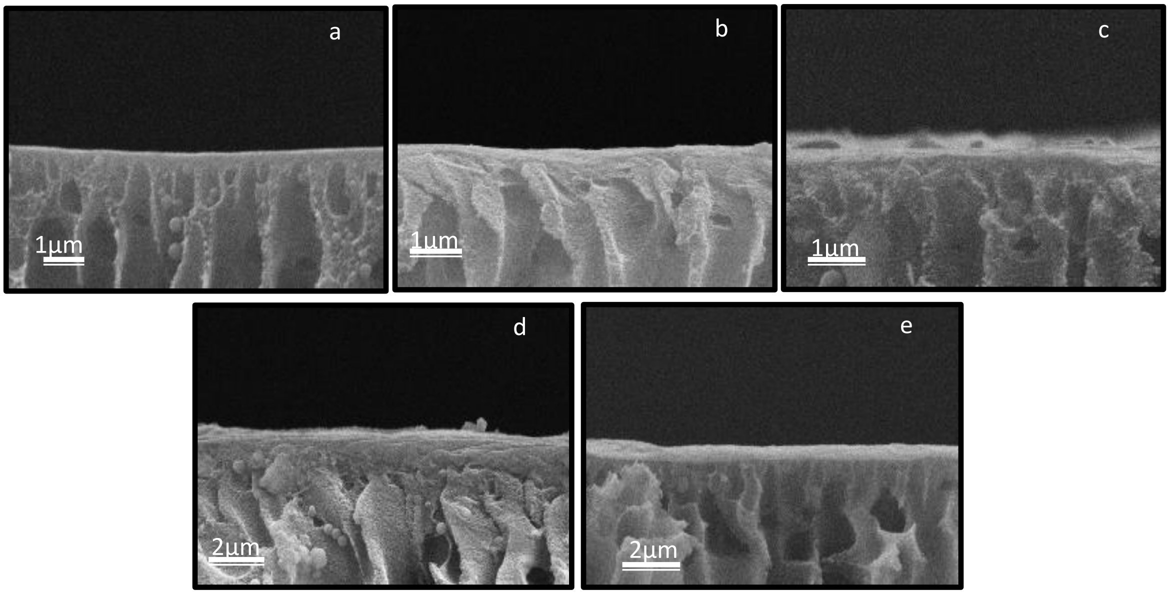

Figure 40 - Cross section SEM imaging of PES mixed matrix membranes containing a) PES control, b) 0.05 wt.% SGO, c) 0.10 wt.% SGO, d) 0.20 wt.% SGO and e) 0.40 wt.% SGO

4.2.2 Topography and Roughness

Figure 41 shows the AFM images of PES-MMM, revealing a decrease in roughness with SGO loading. This could be corroborated with the thickening of the dense layer, as seen in Figure 40. The control membrane had a root-square mean roughness of 23 nm and a maximum roughness of 242 nm, which decreases to 18 and 108 nm with the loading of 0.05 weight percent of SGO. After adding 0.10 weight percent SGO, the maximum and root-square mean roughness level off, as seen in Figure 42. This could suggest that any loading after 0.10 weight percent of SGO may not impact the roughness of the PES matrix.

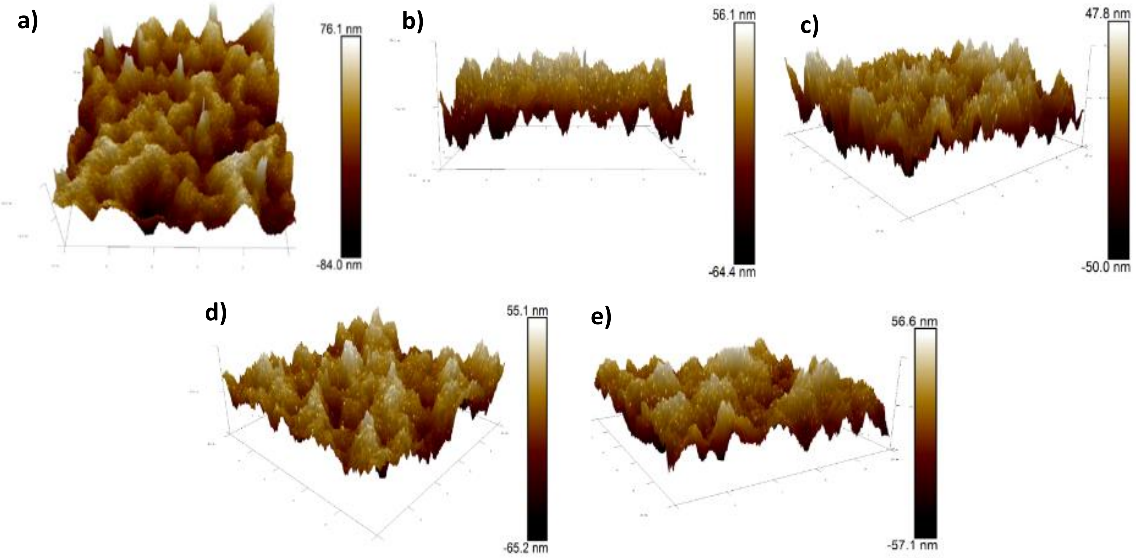

Figure 41 - 3D AFM imaging of PES mixed matrix membranes including a) PES control, b) 0.05 wt.% SGO, c) 0.10 wt.% SGO, d) 0.20 wt.% SGO and e) 0.40 wt.% SGO

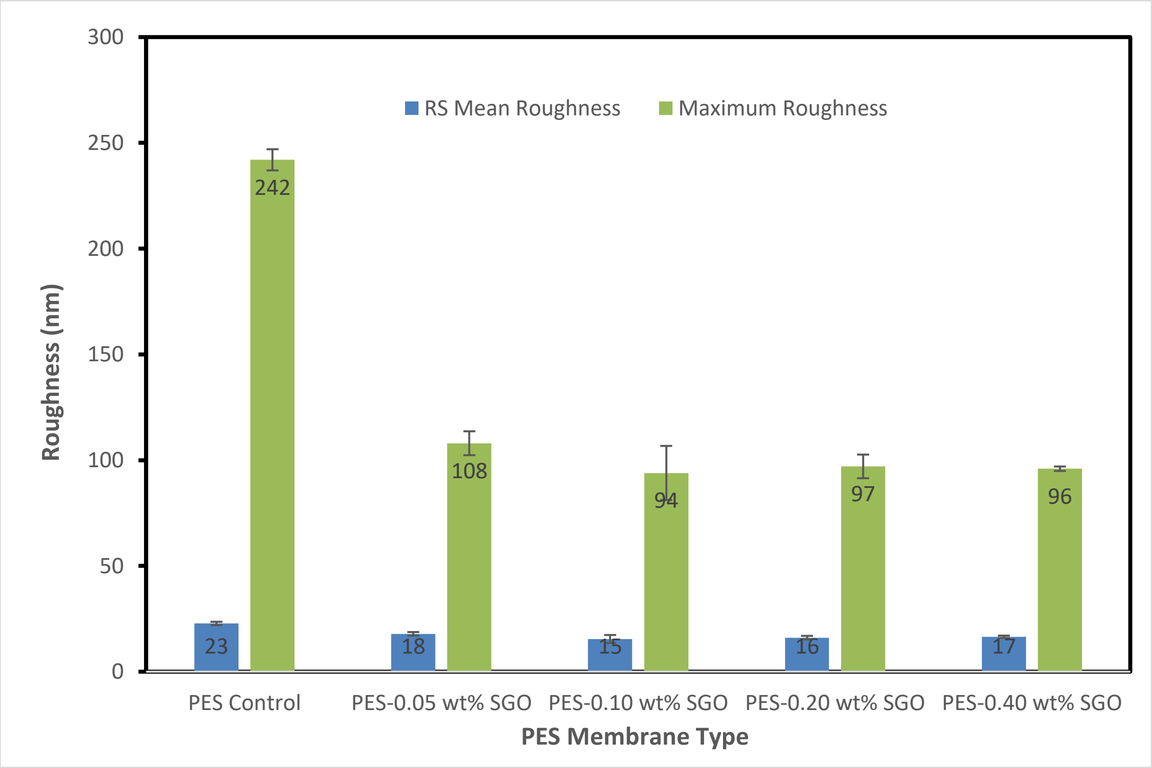

Figure 42 - AFM of polyether sulfone mixed matrix membranes

4.2.3 Wettability

The hydrophilicity of the mixed matrix membrane support is an essential parameter for the water vapor to adsorb onto the surface. Commonly, hydrophilicity or wettability of a membrane is determined through the contact angle analysis, where the lower the contact angle, the more hydrophilic the substrate is. The main influences in wettability remain to be the intermolecular forces between water and the substrate. The stronger the intermolecular forces between them, the more hydrophilic material is.

The wettability is analyzed by measuring the water contact angle. It indicates a contact angle of 70.6°, which may be hydrophilic, although it has potential improvement. The addition of sulfonated GO loading showed a trend of a decreasing contact angle, as can be seen in Figure 43 and Figure 44. This can be explained as a result of SGOs affinity of water during the phase inversion fabrication process. The significant difference in the hydrophilic properties between the SGO and PES results in SGO forming a dense layer at the surface of the membrane. Therefore, a larger cluster of SGO is present with a higher loading, reducing the contact angle further. The significant effect with the increase in hydrophilicity occurs between the control and 0.20 weight percent loading, as the mean contact angle decreases from 70.6° to 60.6°. Whereas the mean contact angle continues to decline to 59.9° for 0.40 weight percent SGO loading, it is not considerable. There is significant overlap with error bars with the 0.20 weight percent samples. Therefore, 0.20 weight percent loading of SGO in PES shows to be the most effective concentration in decreasing the contact angle.

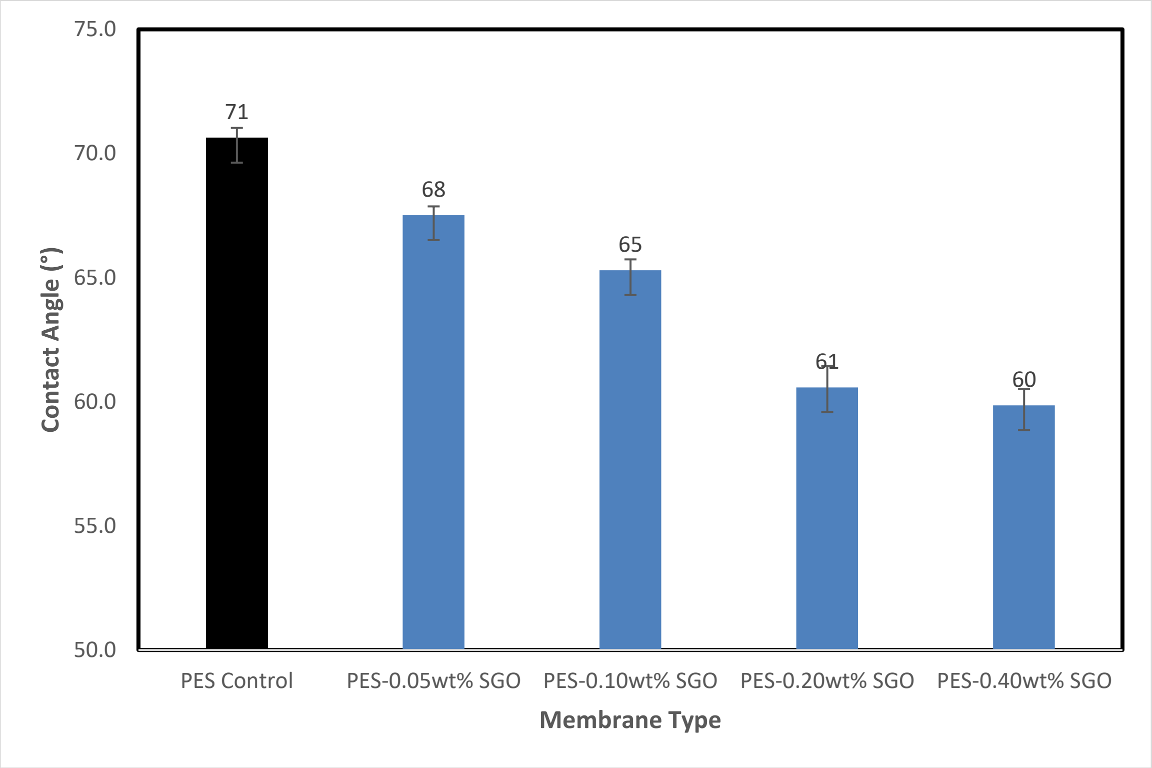

Figure 43 - Contact angle analysis graph for PES mixed matrix membranes

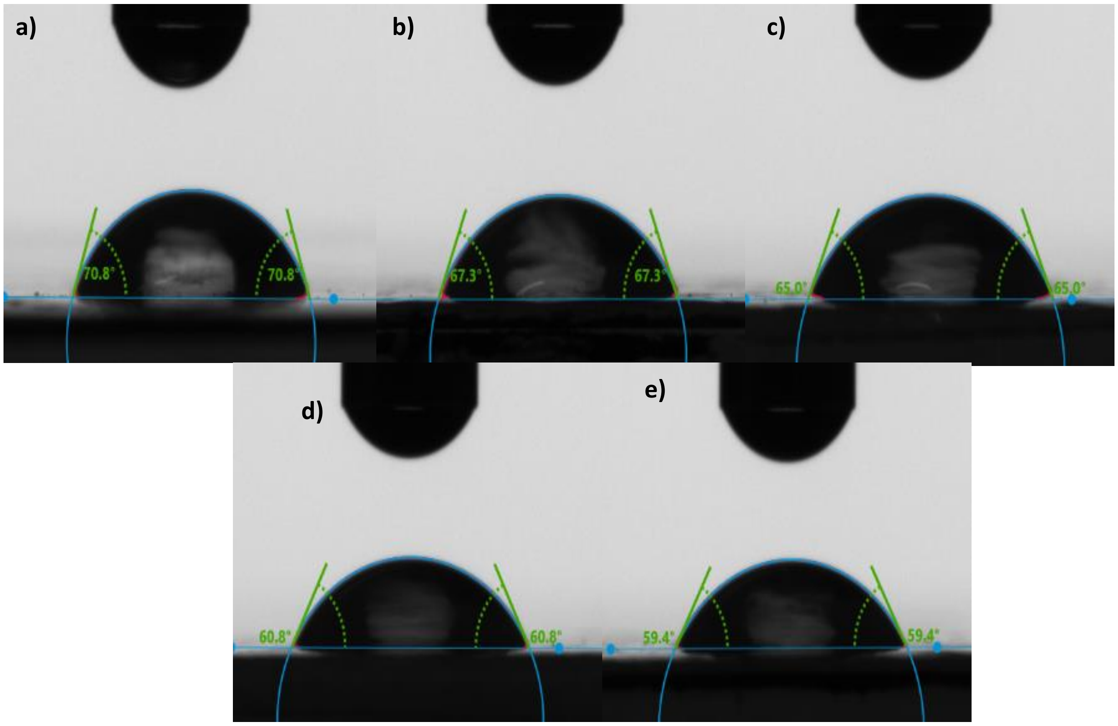

Figure 44 - Contact angle analysis imaging for PES mixed including a) PES Control, b) 0.05 wt.% SGO, c) 0.10 wt.% SGO, d) 0.20 wt.% SGO and e) 0.40 wt.% SGO

4.3 Characterization of Free-Standing Pebax Membranes

4.3.1 Surface and Cross-Sectional Imaging

The Pebax membranes fabricated through solution casting were visualized using SEM to study the surface and the cross-sectional morphology. On the surface of the free-standing Pebax membrane, visible random patterns can be observed. There cannot be a specific estimate of the roughness of the surface of Pebax membranes. However, it is comprehensible that the surface of the Pebax membrane is not smooth. Moreover, the effect of GO can be studied as, with the addition of 0.5 wt.% sulfonated GO, the same patterns and roughness are amplified, as seen in Figure 45. Therefore, via SEM, we can qualitatively determine that the surface roughness of the Pebax membranes increases significantly with the addition of sulfonated GO.

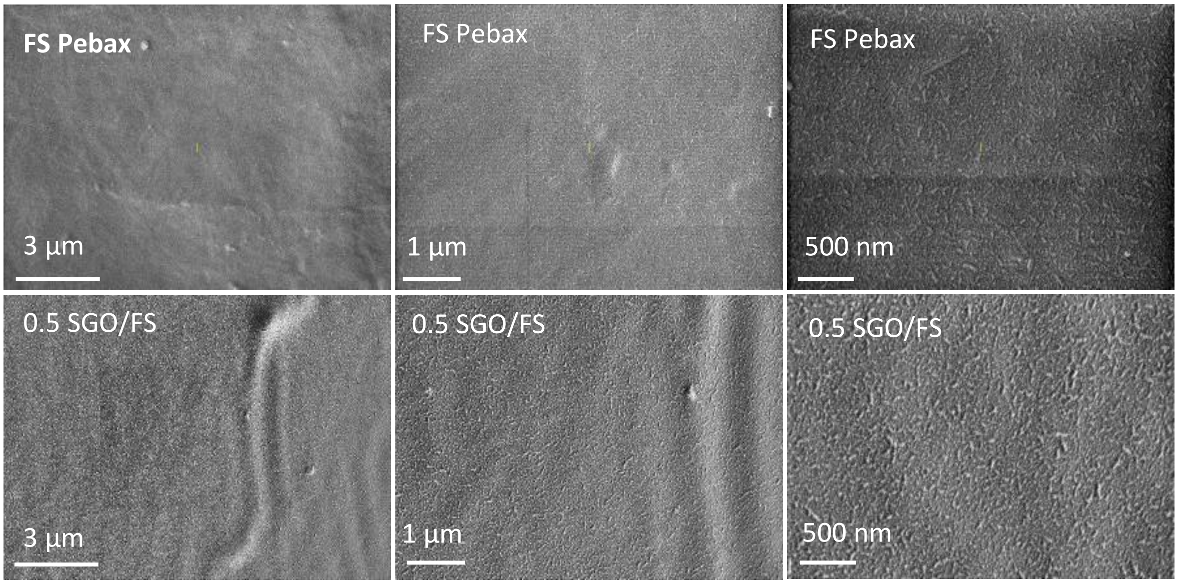

Figure 45 – SEM surface images of the free-standing Pebax membranes

Moreover, imaging of the cross-section allowed the determination of the overall membrane thickness. As seen in Figure 46, the thickness of the free-standing Pebax membrane and its mixed matrix, which included 0.5 wt.% sulfonated GO, was about 11 to 12 µm. The expected thickness of a 5 wt.% Pebax solution and casting with a 250 µm casting knife is expected to gain around a 12.5 µm thin film. While considering the approximate error through image measurements can be corroborated.

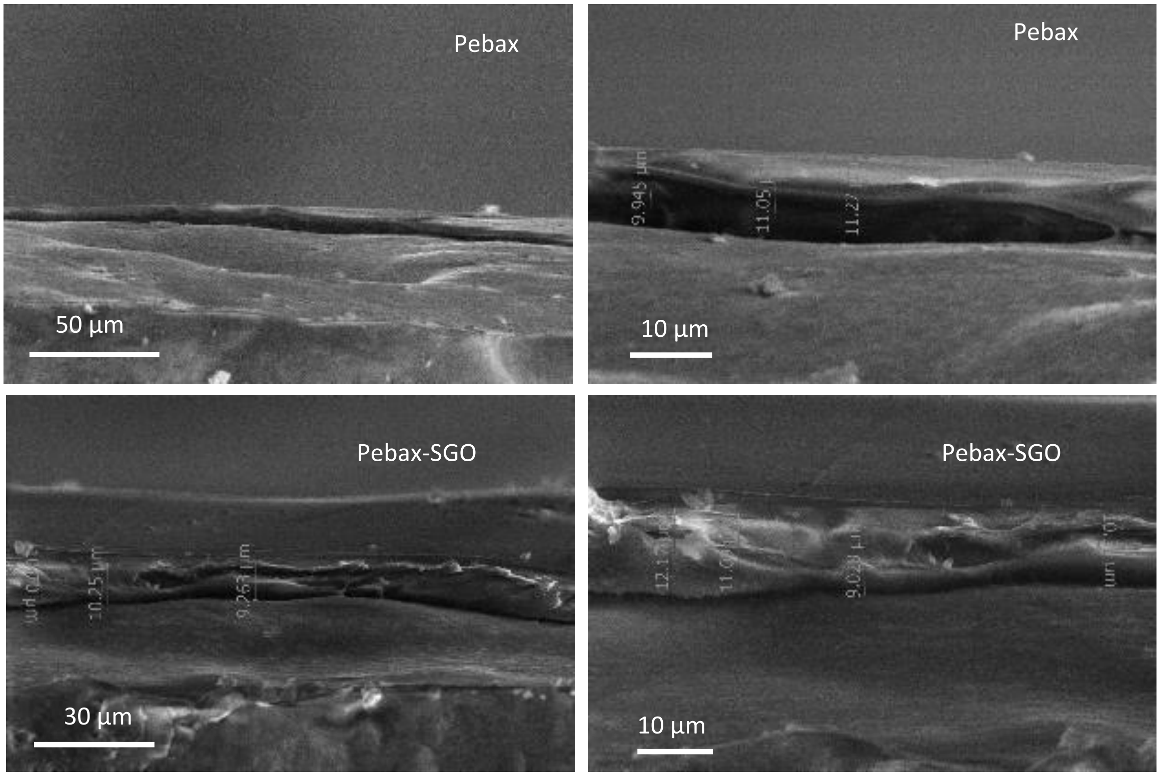

Figure 46 - Cross-sectional imaging of free-standing Pebax membranes

4.3.2 Topography and Roughness

The roughness of a membrane surface indicates how prone it can be to fouling. Generally, with gas separation membranes, fouling can be considered crucial as the performance of the membrane can be affected severely. In Figure 47, the atomic force microscopy shows the topography of the free-standing Pebax membrane and its mixed matrix containing 0.5 wt.% of loading. With the 0.5 wt.% of loading, the roughness can be seen to have increased significantly with more immediate color changes present in the 3D diagram, as well as the large-scale bar present. When quantified, the root square means the roughness of the free-standing Pebax membrane is quantified at around 8.5 nm. In comparison, the MMM containing 0.5 wt.% has a root-square mean roughness of 18.9 nm. The quantified roughness of the surface of the membrane has more than doubled with the addition of 0.5 wt.% sulfonated GO. Moreover, the maximum roughness relays how deep the valleys in the surface are compared to the peaks. While the free-standing Pebax membrane yields 53.4 nm for the maximum roughness, the MMM containing 0.5 wt.% SGO nearly triples the value to about 143.8 nm.

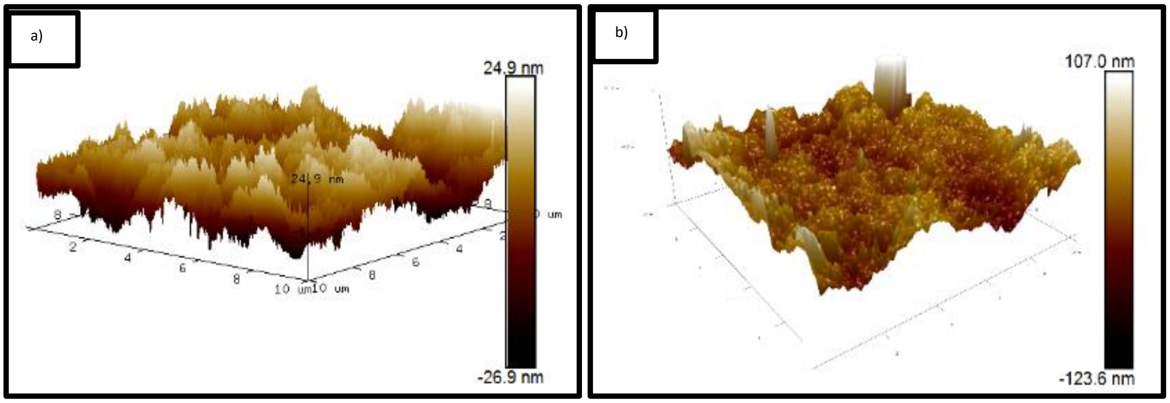

Figure 47 - Topography of a) free standing Pebax membrane and b) 0.5wt% SGO-Pebax MMM

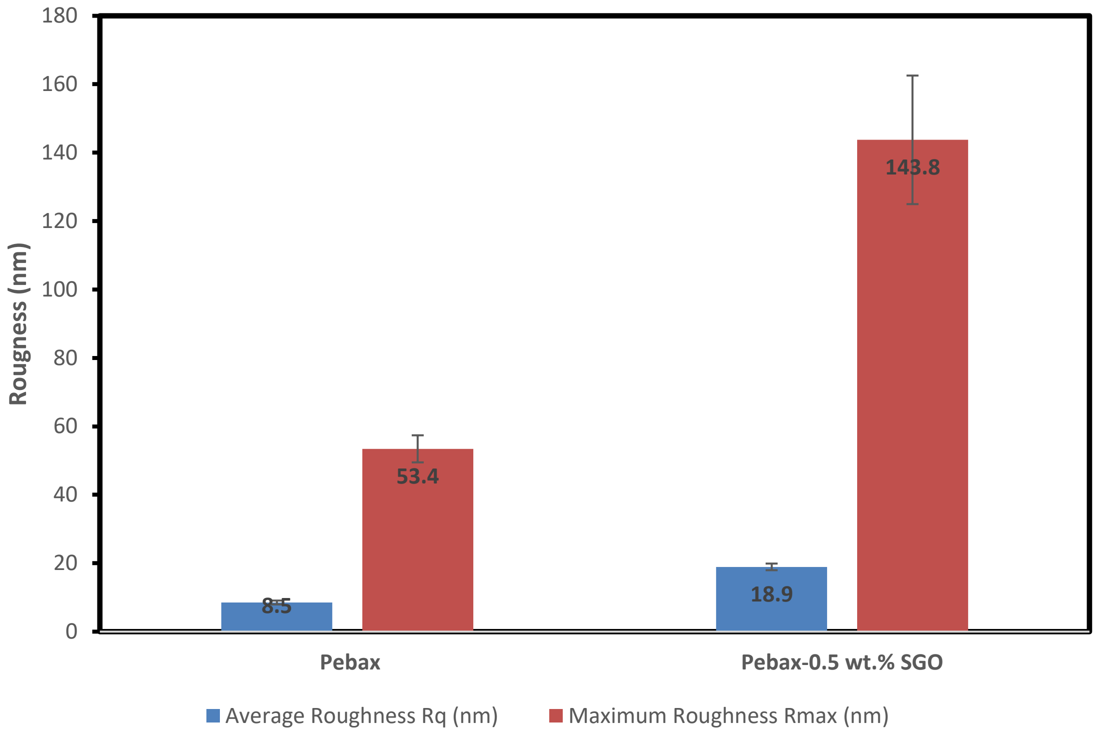

Figure 48 - AFM analysis data for free standing Pebax membranes

4.3.3 Wettability

The wettability analysis for gas separation membranes aiming to permeate water indicates how favorable the diffusion of water from the bulk concentration may be onto the surface membrane. Although Pebax 1074 is a hydrophilic and breathable grade of polyether block amide, it still produces a water contact angle of 74.2°. With the addition of 0.5wt.% SGO, the contact angle decreases to a mean of 72.1°, as shown in Figure 49. The decrease in 2.1° can be attributed to the hydrophilic sulfonated GO present in the dense mixed matrix membrane. While the SGO is present in the MMM, more water-friendly functional groups are present that improve the effect of the intermolecular forces with the water drop. The addition of various hydroxy, carboxyl, and sulfone groups from the SGO assist in doing so, which is the reason for the reduced water contact angle.

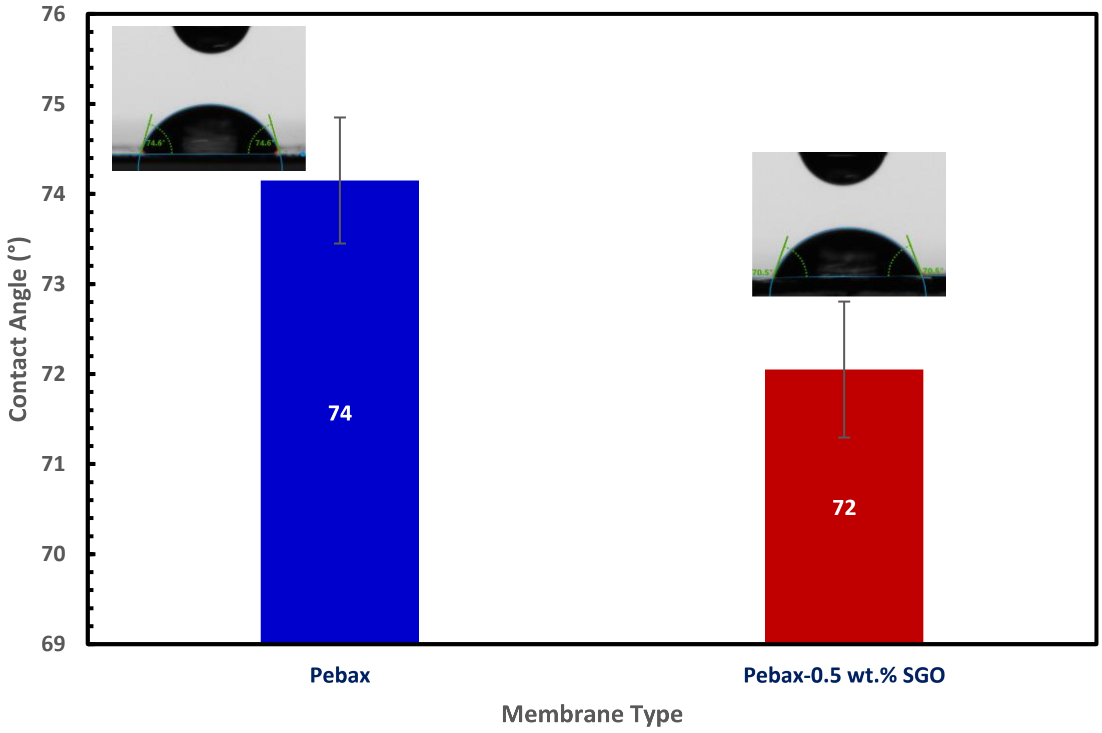

Figure 49 - Contact angle data of Pebax and SGO-Pebax free-standing membranes

4.4 Characterization of Asymmetric Pebax Membranes Supported on PES-SGO MMM

4.4.1 Cross-sectional Imaging

The cross-sectional imaging of the asymmetric Pebax membrane supported on PES and PES-0.2% SGO can determine the thickness of the active layer, as the PES-0.2% SGO support has a thick, dense layer of SGO embedded, which makes it more difficult to distinguish the thickness of the Pebax and SGO-Pebax dense layers. Therefore, the easiest method to identify the thickness of the active layer fabricated by spray coating various layers while using a 0.5 wt.% Pebax solution is to use the PES control membrane.

From Figure 50, we can see that the asymmetric membranes fabricated on the PES support using a coat of 0.5 wt.% Pebax are between 200-300 nm. In contrast, membranes fabricated using two coats of 0.5 wt.% Pebax came around 400-500 nm. The thickness of the active layer determines the transport properties of the membrane, so an initial assumption would predict that the asymmetric Pebax membranes prepared with 2 coats of 0.5wt% Pebax would have poorer transport properties.

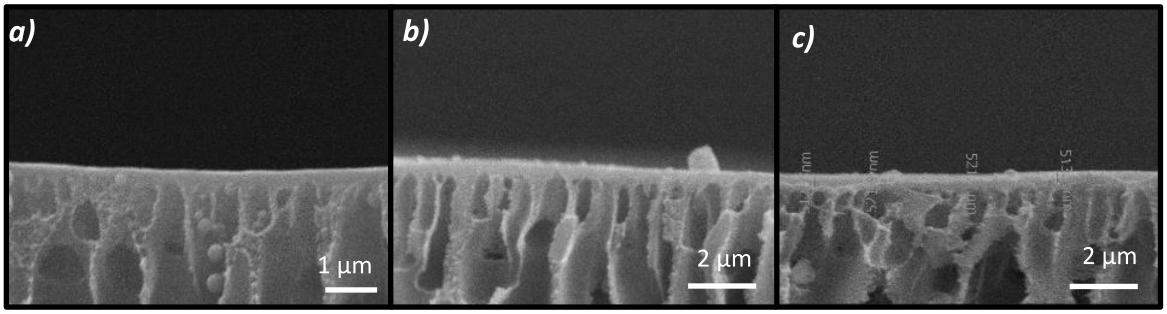

Figure 50 - Cross-section SEM of a) PES coated using 0.5 wt.% Pebax with b) one coating layer and c) two coating layers

4.4.2 Topography and Roughness

The topography and surface roughness for asymmetric Pebax membranes fabricated with coating once or twice with 0.5 wt.% Pebax and 0.5 wt.% Pebax-0.5% SGO were investigated using AFM using tapping mode. The roughness of the asymmetric membranes can help us indicate the gas adsorption patterns and predict possible fouling characteristics of the membrane. In Figure 51, it is observable that the surface roughness in images a) and d) are comparable; however, after being coated twice, it is noticeable that the membrane on the PES support tends to be rougher than on the PES-0.2% SGO Support. This trend continues when the coating is done with 0.5 wt.% Pebax-0.5 wt.% SGO.

In Figure 52, an interesting pattern emerges where the number of coats to fabricate the active layer does not affect the PES control support. The 0.5 wt.% Pebax coats yield a root-square mean roughness of 11.3 nm, and 0.5 wt.% Pebax-0.5%SGO coats yield a root-square mean roughness of about 12.2 nm. This may also be due to the starting roughness of the PES control membrane being slightly lower at 16.6 nm. Since the surface topography of the membrane is relatively smooth, a single or double coat does not influence the final roughness.

Moreover, as previously observed in Figure 50, the coating thickness of 1 coat and two coats are at least 200 and 400 nm thick. Therefore, the coating method of spray coating may significantly influence the final topography of the membrane. In addition, the effect of the number of coats is visible in Figure 53, where the PES-0.2% SGO support where the 2nd coats of 0.5 wt.% Pebax and 0.5 wt.% Pebax-0.5% SGO are smoother at 9.1 and 8.6 nm, respectively, compared to the single coat of 14.3 and 10.5 nm.

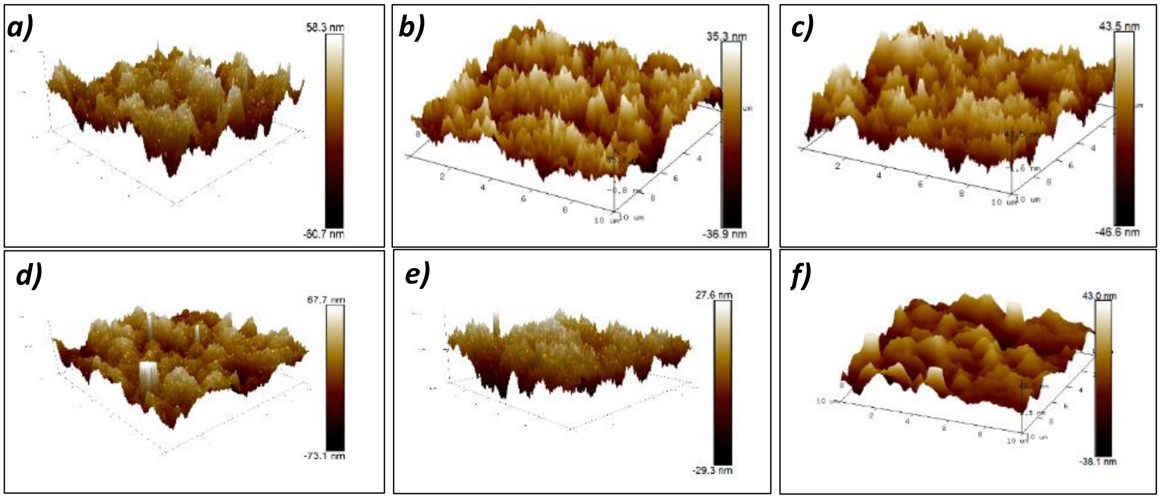

Figure 51: 3D AFM image of a) PES support, coated twice with b) 0.5 wt.% Pebax and c) 0.5 wt.% Pebax-0.5%SGO on PES and d) PES-0.20 sGO coated with twice with e) 0.5 wt.% and f) 0.5 wt.% Pebax-0.5%SGO

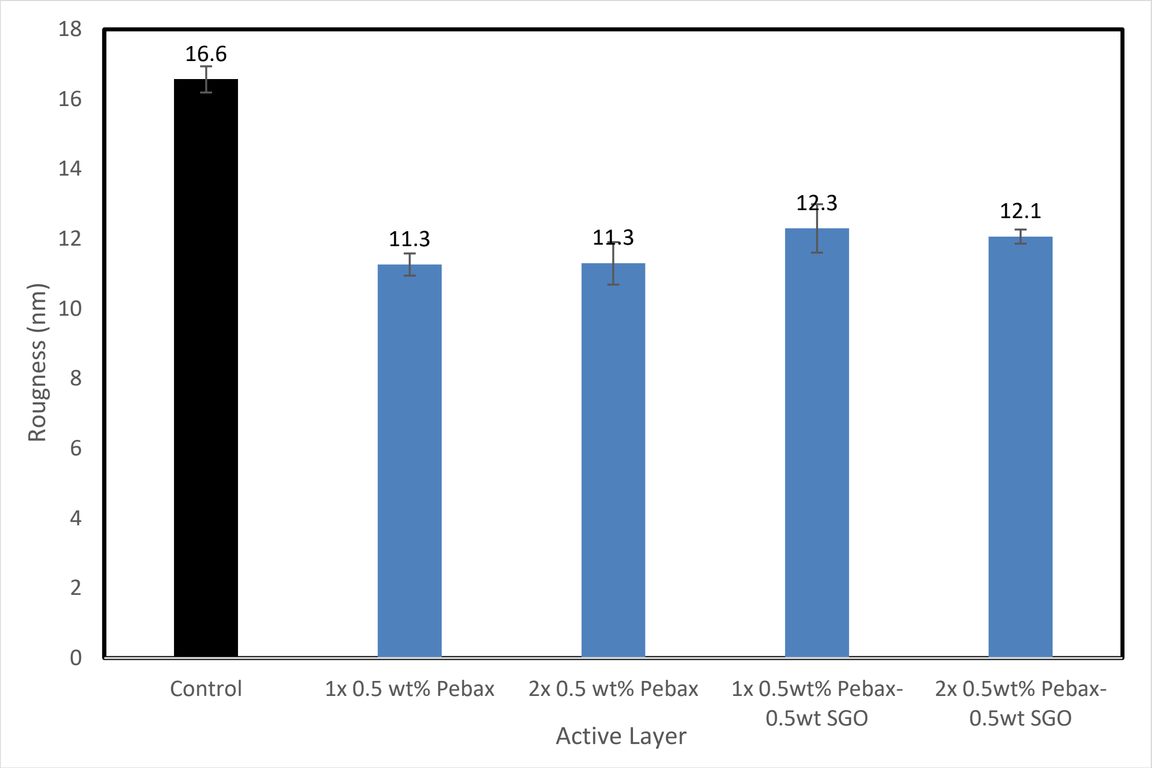

Figure 52 - AFM roughness analysis for Pebax supported membranes with active layers fabricated with different coatings methods on PES

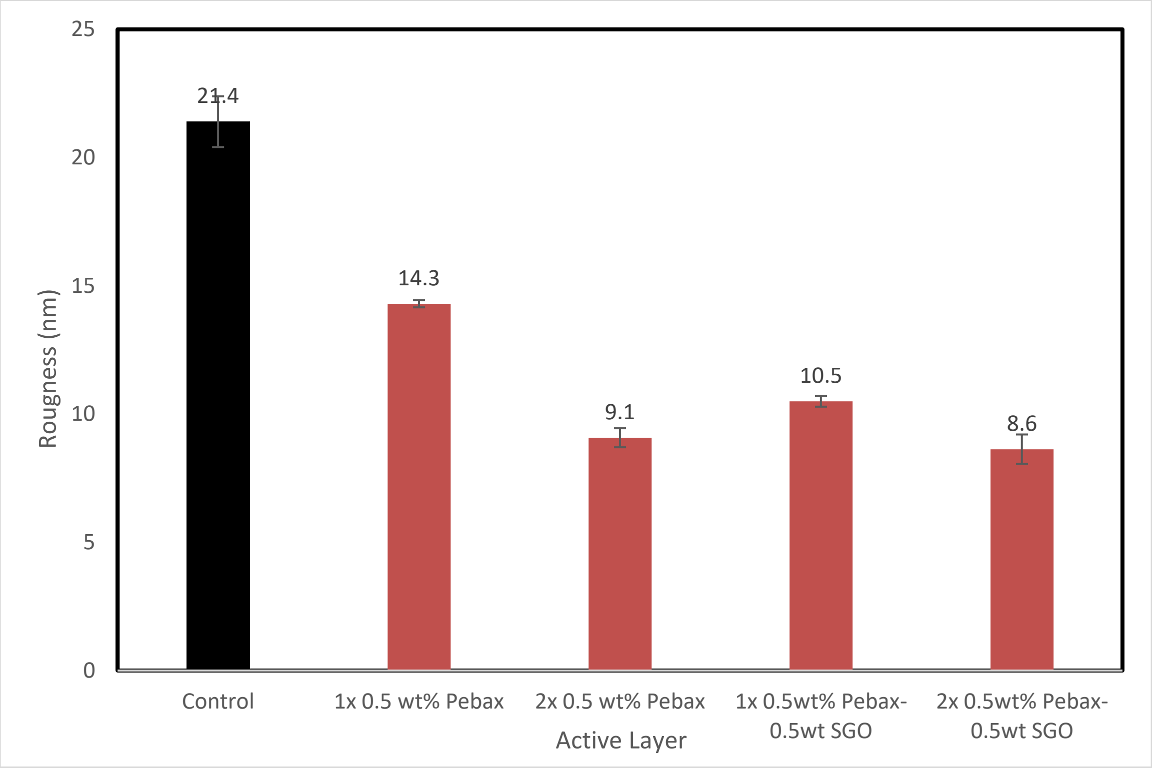

Figure 53 - AFM roughness analysis for Pebax supported membranes with active layers fabricated with different coatings methods on PES-0.2SGO MMM

4.4.3 Wettability

The wettability analysis of the supported Pebax membranes provided showed unexpected results. As the most hydrophilic grade of polyether block amide, Pebax 1074, was used in conjunction with a hydrophilic filler of SGO on hydrophilic support of PES, the results were unanimously more hydrophobic in comparison with all the materials used. Consistently, regardless of support type or the active layer fabrication method, the angle in the result retained to be around 80°. As visible in Figure 54 and Figure 55, the contact angle for the asymmetric membranes remains constant between 79 to 81° without a clear trend.

As far as the addition of 0.5 wt.% SGO in 0.5 wt.% Pebax for one of the coating methods, the lack of influence of the hydrophilic SGO is understandable as the overall amount of SGO present in the active layer is very low. This may cause a suggestion of increasing the SGO filler amount to a more significant amount, which may influence the hydrophilic properties of the asymmetric Pebax membranes.

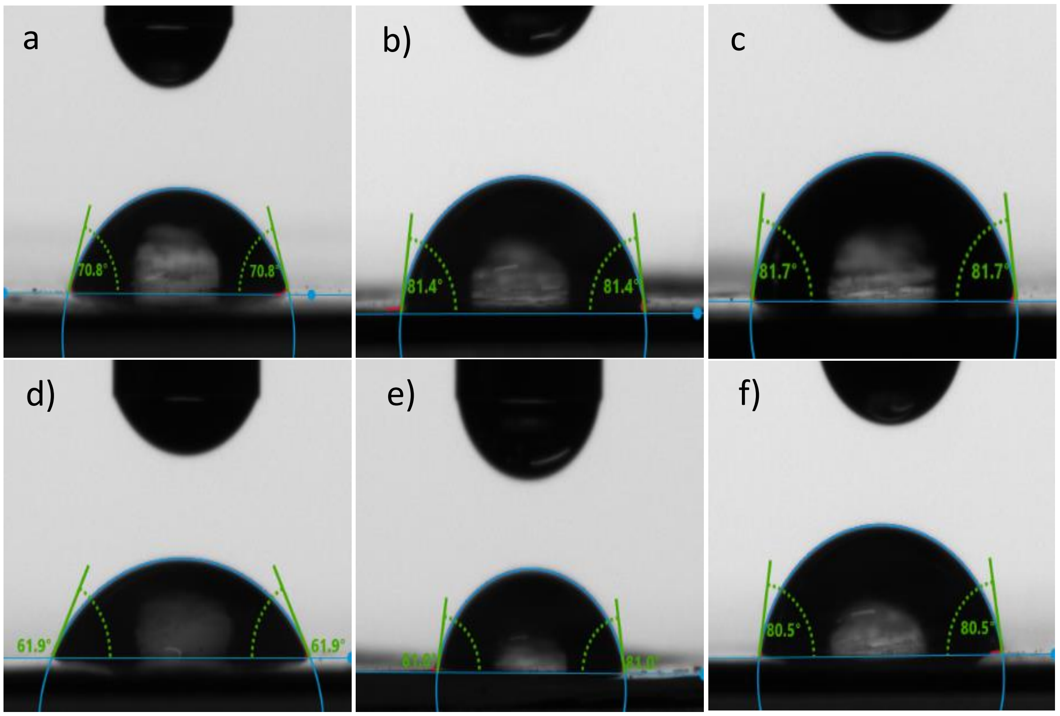

Figure 54 - Contact angle imaging of supported Pebax membranes fabricated on a) PES Control support with coatings of 0.5 wt.% Pebax and 2x 0.5 wt.% Pebax (b,c) and on a PES-0.2%SGO support d), coated with 0.5 wt.% Pebax and 2x 0.5 wt.% Pebax (e,f)

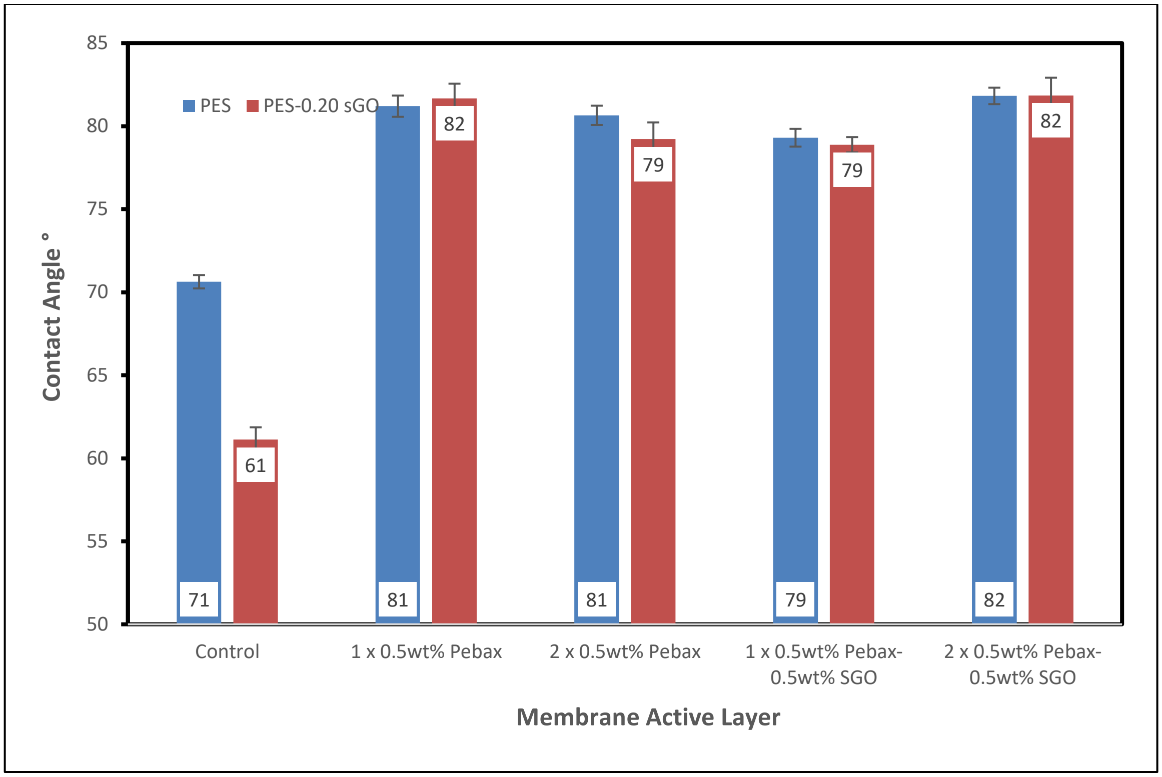

Figure 55 - Contact angle data for asymmetric Pebax membranes

4.5 Performance Testing

The permeance of nitrogen can predict how good a membrane's selectivity property can be. Although the PES-MMM fabricated are not for gas separation, it is interesting to see their behavior for nitrogen permeation with the loading of SGO. As the loading of SGO increases during the phase inversion fabrication process, the denser the top layer of the membrane becomes. Therefore, there should be an effect of nitrogen permeance. This is observable in Figure 56, where the loading of SGO decreases the permeance and permeability of nitrogen through the PES-MMM. More interestingly so, with a 0.05 wt.% loading, the nitrogen permeance under pressure decreases over 30 times. With additional loading, the rejection permeance of nitrogen is limited to around 27 GPU or 2500 Barrers under pressure and 300 GPU and 3300 Barrers under vacuum for the 0.20 wt.% loading. As seen before, this may be the point where the dense layer of the PES matrix becomes saturated with SGO. As PES is an ultrafiltration membrane, the gas transport properties are exceptional. However, this also may mean that there is little to no selectivity.

The permeance of nitrogen under pressure is primarily exaggerated and not aligned with the permeation results under pressure. This may be due to two factors. The first factor may account for leaks in the system. In contrast, the second factor may be mechanical degradation of the pores under vacuum suction.

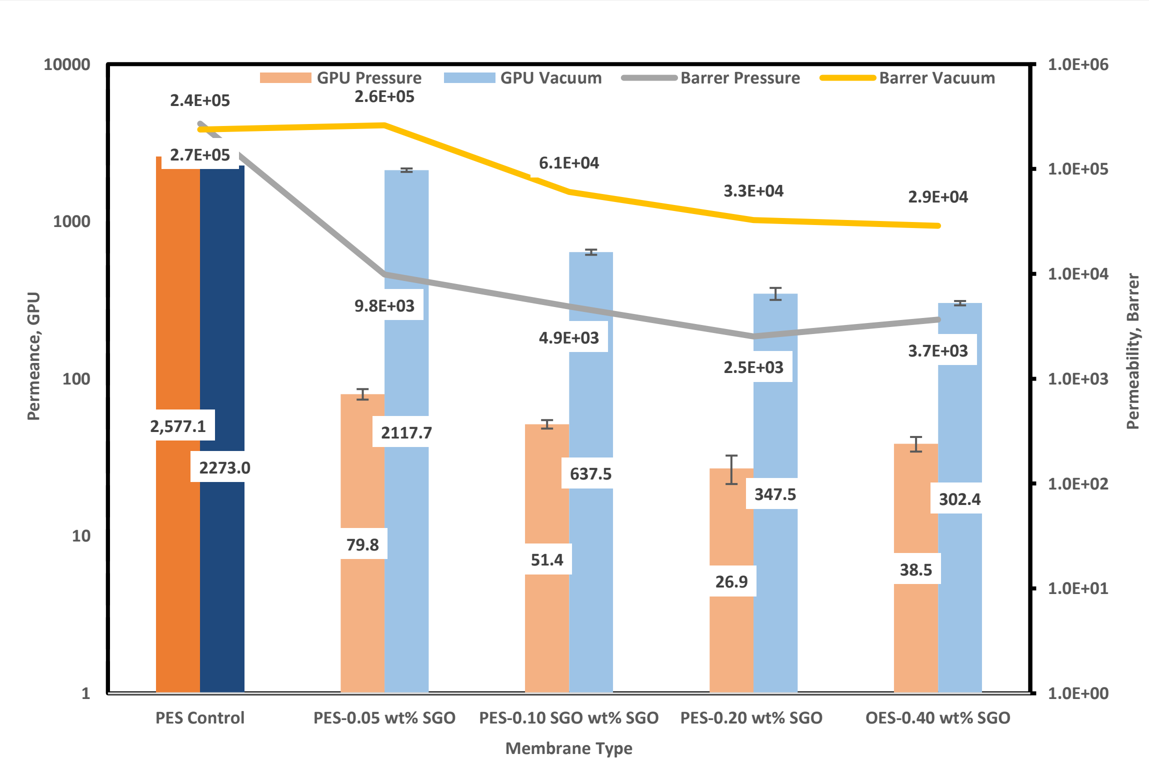

Figure 56 - Nitrogen permeance performance testing for PES-SGO MMM

The nitrogen permeance performance testing becomes interesting when the air-dehumidification membranes are discussed. The first is the asymmetric membranes supported on PES as shown in Figure 57. A single coating of 0.5 wt.% Pebax to fabricate a thin film of an active layer can reduce the nitrogen permeance from 2577 to 386 GPU. Moreover, a second coating to form a thicker layer increases the rejection of nitrogen to yield permeance of 42 GPU under pressure. Interestingly, the coating substrate of Pebax inclusive of 0.5 wt.% SGO also provided similar nitrogen permeance and permeability results. More so, the effect of the permeance was primarily decided by the number of coating layers or the thickness of the active Pebax layer.

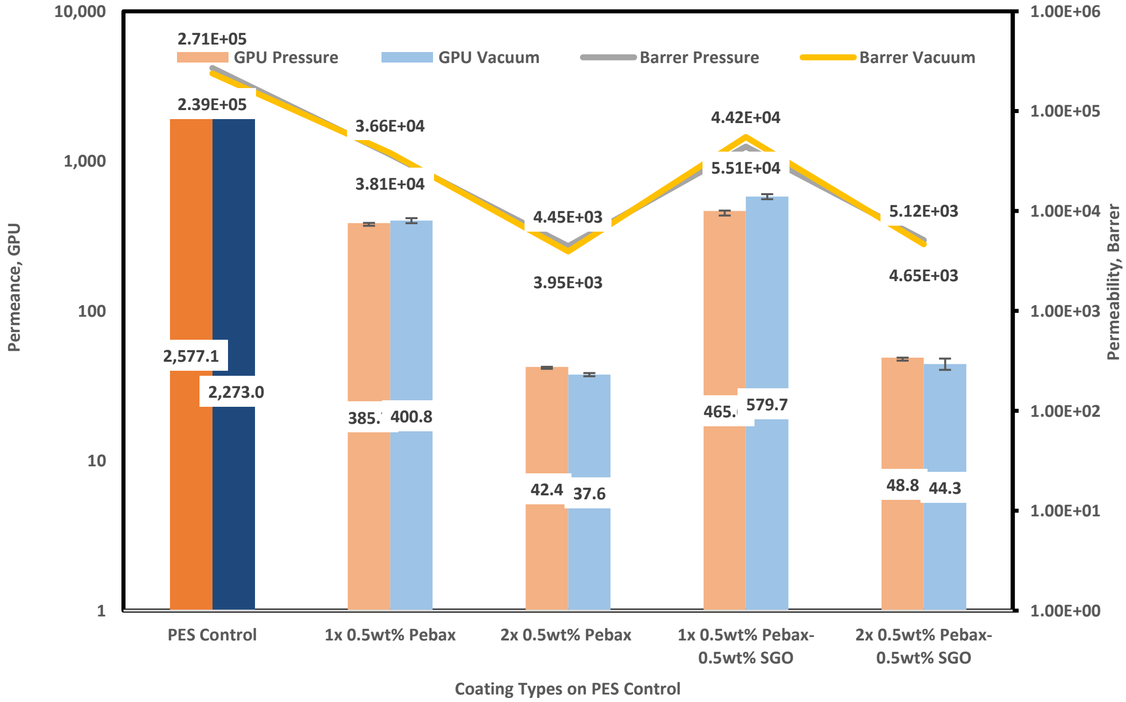

Figure 57 - Nitrogen permeance on asymmetric Pebax membranes on PES Control support

The next set of gas separation membranes testing the permeance of nitrogen are asymmetric membranes supported on 0.20 wt.% SGO/PES. Unsurprisingly, at first glance, the thickness of the active layer has a decisive effect on the permeance and permeability of nitrogen, as observed in Figure 58. However, a key observation is that due to the 0.20 wt.% loading of SGO in the PES matrix, there is a more significant rejection of nitrogen.

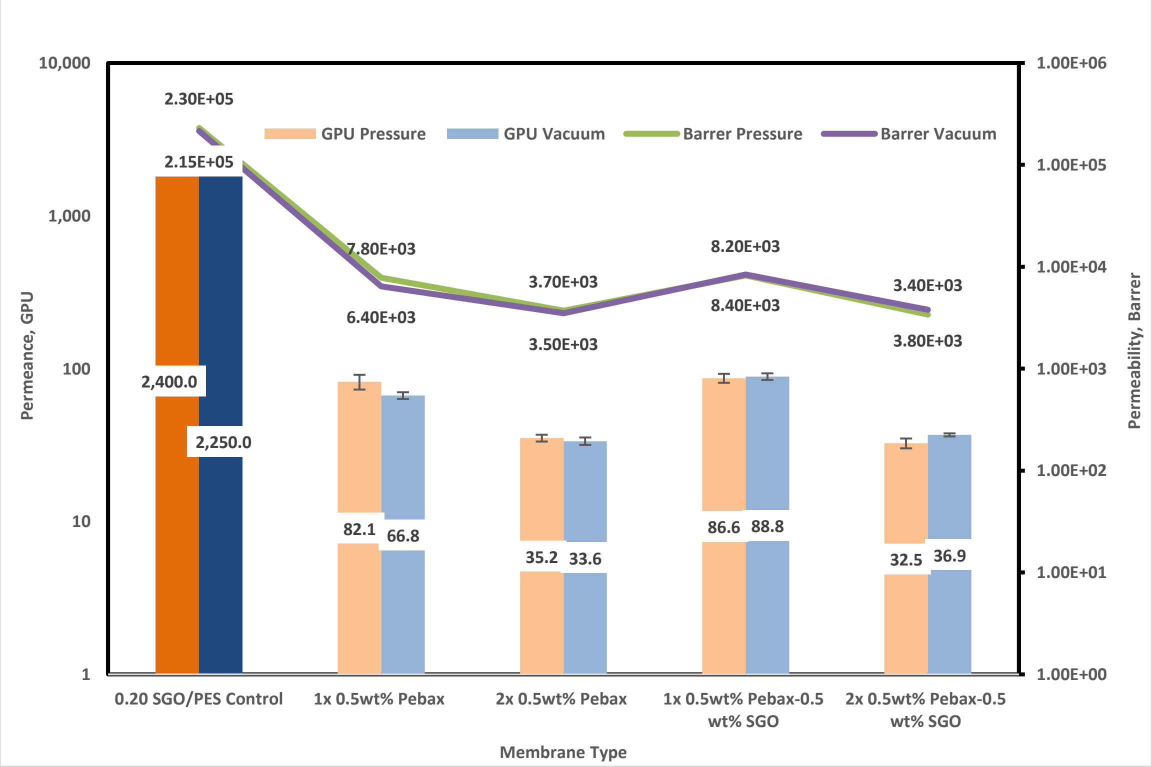

Figure 58 - Nitrogen permeance on asymmetric Pebax membranes on PES-0.2%SGO support

The performance analysis of the free-standing dense Pebax membranes showed that that with the addition of 0.5 wt.% SGO, nitrogen's permeance and permeability of nitrogen increase 5-fold, as shown in Figure 59. In the free-standing Pebax membrane, the only transport path for nitrogen is through the rotation of the soft and flexible polyether block. In contrast, the polyamide block remains rigid and does not allow much movement for nitrogen passing. Whereas with the addition of SGO, the overall roughness of the membrane had been increased tremendously. With a more significant number of active sites, the adsorption of nitrogen to permeate through increases likewise. Therefore, inducing SGO in dense Pebax membrane matrices does help overcome the challenge of poor transport properties. However, there is nothing to say of its effect on selectivity.

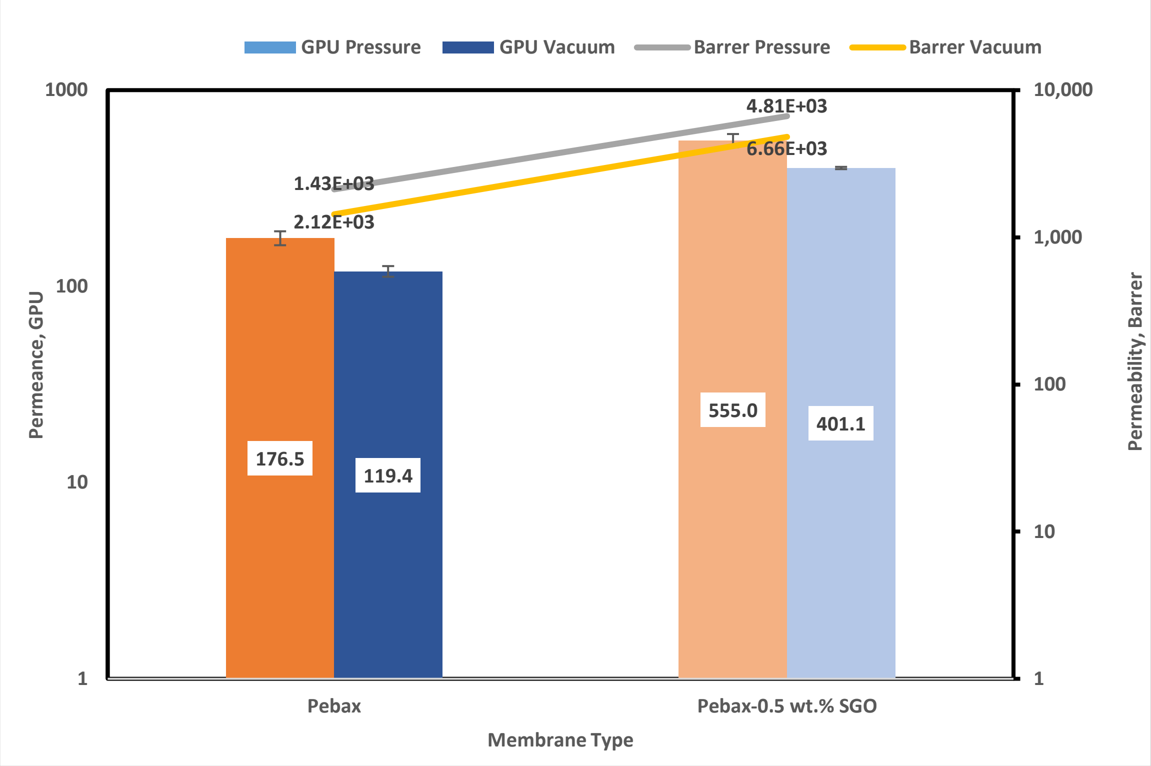

Figure 59 - Nitrogen permeance on free-standing Pebax and its mixed matrix membrane

Chapter V

5. Conclusions and Future Recommendations

5.1 Conclusions

In the initial part of this work, the successful synthesis of GO was commenced following Tour's method, which resulted in consisting of carbon to oxygen ratio of 1.5:1, with the presence of carboxyl, hydroxy, and ether functional groups determined by the chemical structure through the high-resolution scan of XPS. The presence of polar functional groups allows the possible functionalization of GO, which was undertaken by grafting sulfanilic diazonium salt prepared by the sonication of sulfanilic acid and sodium nitrite in DI water. The XPS analysis confirmed the successful grafting as indicated by nitrogen attached to a phenyl ring. Additionally, a 0.3 atomic weight percent of sulfur was detected in the elemental analysis of SGO through the quantification of the XPS analysis. Moreover, the XRD analysis showed that the d-spacing of both SGO and SRGO was reduced to 0.89 and 0.87 nm from 0.93 nm of GO. However, while calculating the crystal size through Scherrer's equation, it was observable that the crystal size of SGO had increased to 9.06 nm from 8.86 after the attempted sulfonation of GO. The growth in crystal size is corroborated in the literature with the successful functionalization of GO. An increase in hydrophilicity was observed from the sulfonation of GO as the contact angle dropped from 38° to 26°. This shows the effectiveness of the sulfonation of GO and its promise in future work

Two paths were undertaken to overcome the challenge of poor transport properties of dense polymer gas separation films. The first was to fabricate free-standing membranes incorporating SGO to improve the transport properties. The second was to fabricate asymmetric Pebax membranes supported on an ultrafiltration PES membrane. The PES membranes were fabricated at 17.5 wt.% of PES via phase inversion with loading 0.05, 0.10, 0.20, and 0.40 wt.%. The characterization of the PES-MMM yielded that with the loading of SGO, the dense layer of PES became thicker. This was concluded to be due to the rapid immigration of SGO to the water interface during the phase inversion fabrication process. Also, as confirmed by imaging, the pore size becomes smaller with increasing the loading of SGO from 0 to 0.20 wt.%.

Moreover, based on the wettability analysis, the optimum SGO concentration in the PES matrix was revealed to be 0.2 wt.% as the contact angle was reduced from 70.6 for the PES membrane to 60.6° for the PES-0.2 SGO MMM. Although the contact angle stayed ~ 59.6° with 0.40 wt.% loading, the error bars and tradeoff for twice the filler amount did not prove conclusive enough to use 0.40 wt.% SGO/PES as the support membrane.

Two sets of gas separation membranes were fabricated; the free-standing Pebax membrane, including SGO as a filler in the mixed matrix, and a supported asymmetric Pebax membrane on PES and PES-0.2 wt.% SGO supports. The thin-film fabrication on the ultrafiltration support was done using coats of 0.5 wt.% via air spray. The cross-sectional and surface imaging showed that the free-standing Pebax membrane resulted in being about 11 µm thin. Furthermore, the qualitative surface imaging showed that adding 0.50 wt.% of SGO in the Pebax matrix resulted in a much rougher surface. The topography of the free-standing Pebax membranes was studied through AFM in the tapping mode where the average roughness of free-standing Pebax was 8.5 nm, whereas the 0.5 wt.% SGO/Pebax membrane had an average roughness of 18.4 nm. Lastly, the wettability analysis to study the hydrophilicity of the free-standing Pebax membranes showed that with the addition of 0.5 wt.% SGO, the dense Pebax membrane's contact angle decreased from 74° to 72°.

The second set of gas separation membranes were membranes fabricated by being coated on the supports of PES and PES-0.2 wt.% SGO with 0.5 wt.% Pebax and 0.5 wt.% Pebax-0.5 wt.% SGO substrates. The cross-sectional imaging showed that each coat of 0.5 wt.% Pebax added about 200 nm of a thin active Pebax layer. The topography of these membranes left much to be desired as there were no visible effects between the number of coats for the asymmetric Pebax membranes supported on PES. The resulting roughness averaged around to be 11.3 nm for coatings with 0.5 wt.% substrate and 12.2 nm for coatings with 0.5 wt.% Pebax-0.5 wt.% SGO substrates. A difference of a nanometer can be concluded with the incorporation of SGO to form the active layer in the asymmetric membrane. Moving on, the topography of the Pebax supported PES-0.2%SGO membranes showed a reduction in roughness with each coat for each substrate.

Lastly, the nitrogen performance test was conducted on the PES-MMM, the two sets of asymmetric membranes, and the free-standing Pebax-SGO MMM. The PES-MMM showed significant rejection of nitrogen with the addition of SGO, where the PES-0.2%SGO showed the least permeation and best rejection of nitrogen. Moreover, the performance analysis of Pebax supported on PES and PES-MMM showed that with a thicker active layer, the nitrogen permeance decreases significantly. The difference is 0.5w.% Pebax and 0.5 wt.% Pebax-0.5%SGO were unidentifiable in either of their uses for nitrogen permeance signifying the most critical parameter in transport properties for a thin film composite is the thickness of the active layer. Lastly, the dense free-standing Pebax membranes saw a 5-fold increase in nitrogen permeance and permeability with the addition of 0.5 wt.% SGO. This is justifiable with the significant increase in roughness, which increases the active sites for nitrogen adsorption.

5.2 Recommendation and Future Work

Polyether block amide is a promising material candidate for the application of gas separation. However, this work remains incomplete without thoroughly testing water permeance and water/nitrogen selectivity results. Moreover, there is a significant shortcoming in the lack of investigation regarding various loadings of SGO in both the free-standing Pebax membranes and the supported Pebax membranes, as only one loading of 0.5 wt.% SGO is consistently used.

For future work, apart from adhering to the recommendations, it may be suitable to dry other polymers that have shown excellent water/nitrogen separation properties like sulfonated polyether ketone, which may work well with sulfonated GO. Moreover, various other fillers should be investigated, and perhaps a more novel and higher loading of sulfonation should be attempted as 0.3% of sulfur had significant effects. Still, it may be possible to improve on that to enhance the filler properties even further.

6. References

[1] P. C. Change, "Global warming of 1.5° C," *Geneva, Switzerland: World Meteorological Organization*, 2018.

[2] IEA. "The Future of Cooling." (accessed.

[3] B. Zhao, N. Peng, C. Liang, W. F. Yong, and T.-S. Chung, "Hollow fiber membrane dehumidification device for air conditioning system," *Membranes,* vol. 5, no. 4, pp. 722-738, 2015.

[4] G. F. Hundy, A. R. Trott, and T. C. Welch, "Chapter 3 - Refrigerants," in *Refrigeration and Air-Conditioning (Fourth Edition)*, G. F. Hundy, A. R. Trott, and T. C. Welch Eds. Oxford: Butterworth-Heinemann, 2008, pp. 30-40.

[5] B. Kim, S. H. Lee, D. Lee, and Y. Kim, "Performance comparison of heat pumps using low global warming potential refrigerants with optimized heat exchanger designs," *Applied Thermal Engineering,* vol. 171, p. 114990, 2020/05/05/ 2020, doi: https://doi.org/10.1016/j.applthermaleng.2020.114990.

[6] W. Goetzler, R. Shandross, J. Young, O. Petritchenko, D. Ringo, and S. McClive, "Energy savings potential and RD&D opportunities for commercial building HVAC systems," Navigant Consulting, Burlington, MA (United States), 2017.

[7] B. Yang, W. Yuan, F. Gao, and B. Guo, "A review of membrane-based air dehumidification," *Indoor and Built Environment,* vol. 24, no. 1, pp. 11-26, 2015.

[8] D. E. Claridge *et al.*, "A new approach for drying moist air: The ideal Claridge-Culp-Liu dehumidification process with membrane separation, vacuum compression and sub-atmospheric condensation," *International Journal of Refrigeration,* vol. 101, pp. 211-217, 2019.

[9] M.-G. Ham, W.-J. Jeon, H.-J. Kim, C.-u. Bak, and Y.-D. Kim, "Performance and viability of absorptive dehumidification module using flat-sheet polytetrafluoroethylene/polypropylene composite membranes," *Energy Conversion and Management,* vol. 205, p. 112393, 2020.

[10] N. Fumo and D. Y. Goswami, "Study of an aqueous lithium chloride desiccant system: air dehumidification and desiccant regeneration," *Solar Energy,* vol. 72, no. 4, pp. 351-361, 2002/04/01/ 2002, doi: https://doi.org/10.1016/S0038-092X(02)00013-0.

[11] T. Bui, Y. Wong, M. Islam, and K. Chua, "On the theoretical and experimental energy efficiency analyses of a vacuum-based dehumidification membrane," *Journal of Membrane Science,* vol. 539, pp. 76-87, 2017.

[12] N. Zhang, S.-Y. Yin, and H.-H. Yang, "Transient performance of coupled heat and mass transfer in cross-flow hollow fiber membrane module for air dehumidification," *International Journal of Refrigeration,* vol. 108, pp. 190-199, 2019.

[13] Q. Chen and X. Zhang, "Modeling and data analysis of multistory flat plate quasi-counter-flow membrane dehumidifier," *Applied Thermal Engineering,* vol. 128, pp. 837-848, 2018.

[14] A. A. Bukshaisha and B. M. Fronk, "Simulation of membrane heat pump system performance for space cooling," *International Journal of Refrigeration,* vol. 99,

pp. 371-381, 2019.

[15] J. R. Werber, C. O. Osuji, and M. Elimelech, "Materials for next-generation desalination and water purification membranes," *Nature Reviews Materials*, vol. 1, no. 5, pp. 1-15, 2016.

[16] R. Ciora and P. K. Liu, "Ceramic membranes for environmental related applications," *Fluid/Particle Separation Journal*, vol. 15, no. 1, pp. 51-60, 2003.

[17] X. Cheng *et al.*, "Water-selective permeation in hybrid membrane incorporating multi-functional hollow ZIF-8 nanospheres," *Journal of Membrane Science*, vol. 555, pp. 146-156, 2018/06/01/ 2018, doi: https://doi.org/10.1016/j.memsci.2018.03.024.

[18] N. L. Le and S. P. Nunes, "Materials and membrane technologies for water and energy sustainability," *Sustainable Materials and Technologies*, vol. 7, pp. 1-28, 2016.

[19] N. Song, X. Gao, Z. Ma, X. Wang, Y. Wei, and C. Gao, "A review of graphene-based separation membrane: Materials, characteristics, preparation and applications," *Desalination*, vol. 437, pp. 59-72, 2018.

[20] H. Sijbesma, K. Nymeijer, R. van Marwijk, R. Heijboer, J. Potreck, and M. Wessling, "Flue gas dehydration using polymer membranes," *Journal of Membrane Science*, vol. 313, no. 1-2, pp. 263-276, 2008.

[21] K. A. Mkhoyan *et al.*, "Atomic and electronic structure of graphene-oxide," *Nano letters*, vol. 9, no. 3, pp. 1058-1063, 2009.

[22] R. Qi, C. Dong, and L.-Z. Zhang, "A review of liquid desiccant air dehumidification: From system to material manipulations," *Energy and Buildings*, vol. 215, p. 109897, 2020.

[23] Z. Chen, J. Zhu, H. Bai, Y. Yan, and L. Zhang, "Experimental study of a membrane-based dehumidification cooling system," *Applied Thermal Engineering*, vol. 115, pp. 1315-1321, 2017.

[24] G. Annadurai, S. Tiwari, and M. Maiya, "Experimental performance comparison of adiabatic and internally-cooled membrane dehumidifiers," *International Journal of Low-Carbon Technologies*, vol. 13, no. 3, pp. 240-249, 2018.

[25] R. Qi, D. Li, and L.-Z. Zhang, "Performance investigation on polymeric electrolyte membrane-based electrochemical air dehumidification system," *Applied Energy*, vol. 208, pp. 1174-1183, 2017.

[26] P. Scovazzo and R. MacNeill, "Membrane module design, construction, and testing for vacuum sweep dehumidification (VSD): Part I, prototype development and module design," *Journal of membrane science*, vol. 576, pp. 96-107, 2019.

[27] D. Mohshim, H. Mukhtar, Z. Man, and R. Nasir, "Latest Development on Membrane Fabrication for Natural Gas Purification: A Review," *Journal of Engineering*, vol. 2013, 12/04 2012, doi: 10.1155/2013/101746.

[28] Y. Yampolskii, "1.3 Basic Aspects of Gas Transport in Membranes," in *Comprehensive Membrane Science and Engineering*: Elsevier Oxford, 2017, pp. 57-64.

[29] Y. Yampolskii, "Polymeric gas separation membranes," *Macromolecules*, vol. 45, no. 8, pp. 3298-3311, 2012.

[30] P. Pandey and R. Chauhan, "Membranes for gas separation," *Progress in Polymer Science*, vol. 26, no. 6, pp. 853-893, 2001.

[31] B. Zhu *et al.*, "Functional zeolitic framework membranes for water treatment and desalination," Wiley Online Library, 2013.

[32] B. Zhu *et al.*, "Short Review on Porous Metal Membranes—Fabrication, Commercial Products, and Applications," *Membranes*, vol. 8, no. 3, 2018, doi: 10.3390/membranes8030083.

[33] T. Leiknes, H. Myklebust, and H. Ødegaard, "Metal membranes for drinking water treatment," *Membrane Technology*, vol. 2005, no. 4, pp. 6-10, 2005/04/01/ 2005, doi: https://doi.org/10.1016/S0958-2118(05)00346-0.

[34] S. M. Samaei, S. Gato-Trinidad, and A. Altaee, "The application of pressure-driven ceramic membrane technology for the treatment of industrial wastewaters – A review," *Separation and Purification Technology*, vol. 200, pp. 198-220, 2018/07/12/ 2018, doi: https://doi.org/10.1016/j.seppur.2018.02.041.

[35] C. Li, W. Sun, Z. Lu, X. Ao, and S. Li, "Ceramic nanocomposite membranes and membrane fouling: A review," *Water Research*, vol. 175, p. 115674, 2020/05/15/ 2020, doi: https://doi.org/10.1016/j.watres.2020.115674.

[36] N. F. Ishak, N. A. Hashim, M. H. D. Othman, P. Monash, and F. M. Zuki, "Recent progress in the hydrophilic modification of alumina membranes for protein separation and purification," *Ceramics International*, vol. 43, no. 1, Part B, pp. 915-925, 2017/01/01/ 2017, doi: https://doi.org/10.1016/j.ceramint.2016.10.044.

[37] K. P. Lee, T. C. Arnot, and D. Mattia, "A review of reverse osmosis membrane materials for desalination—Development to date and future potential," *Journal of Membrane Science*, vol. 370, no. 1, pp. 1-22, 2011/03/15/ 2011, doi: https://doi.org/10.1016/j.memsci.2010.12.036.

[38] D. Rana and T. Matsuura, "Surface modifications for antifouling membranes," *Chemical reviews*, vol. 110, no. 4, pp. 2448-2471, 2010.

[39] S. F. Anis, R. Hashaikeh, and N. Hilal, "Reverse osmosis pretreatment technologies and future trends: A comprehensive review," *Desalination*, vol. 452, pp. 159-195, 2019.

[40] B. Chakrabarty, A. K. Ghoshal, and M. K. Purkait, "Preparation, characterization and performance studies of polysulfone membranes using PVP as an additive," *Journal of Membrane Science*, vol. 315, no. 1, pp. 36-47, 2008/05/01/ 2008, doi: https://doi.org/10.1016/j.memsci.2008.02.027.

[41] K. S. Kim, K. H. Lee, K. Cho, and C. E. Park, "Surface modification of polysulfone ultrafiltration membrane by oxygen plasma treatment," *Journal of Membrane Science*, vol. 199, no. 1, pp. 135-145, 2002/04/30/ 2002, doi: https://doi.org/10.1016/S0376-7388(01)00686-X.

[42] A. Lee, J. W. Elam, and S. B. Darling, "Membrane materials for water purification: design, development, and application," *Environmental Science: Water Research & Technology*, vol. 2, no. 1, pp. 17-42, 2016.

[43] A. Bétard and R. A. Fischer, "Metal–Organic Framework Thin Films: From Fundamentals to Applications," *Chemical Reviews*, vol. 112, no. 2, pp. 1055-1083, 2012/02/08 2012, doi: 10.1021/cr200167v.

[44] W. Li, "Metal–organic framework membranes: Production, modification, and applications," *Progress in Materials Science,* vol. 100, pp. 21-63, 2019/02/01/ 2019, doi: https://doi.org/10.1016/j.pmatsci.2018.09.003.

[45] I. Ullah Khan *et al.*, "Status and improvement of dual-layer hollow fiber membranes via co-extrusion process for gas separation: A review," *Journal of Natural Gas Science and Engineering,* vol. 52, pp. 215-234, 2018/04/01/ 2018, doi: https://doi.org/10.1016/j.jngse.2018.01.043.

[46] A. Constantinou, S. Barrass, and A. Gavriilidis, "CO2 Absorption in Polytetrafluoroethylene Membrane Microstructured Contactor Using Aqueous Solutions of Amines," *Industrial & Engineering Chemistry Research,* vol. 53, no. 22, pp. 9236-9242, 2014/06/04 2014, doi: 10.1021/ie403444t.

[47] Y.-T. Jia, J. Gong, X.-H. Gu, H.-Y. Kim, J. Dong, and X.-Y. Shen, "Fabrication and characterization of poly (vinyl alcohol)/chitosan blend nanofibers produced by electrospinning method," *Carbohydrate Polymers,* vol. 67, no. 3, pp. 403-409, 2007/02/01/ 2007, doi: https://doi.org/10.1016/j.carbpol.2006.06.010.

[48] Y. T. Jia, H. Y. Kim, J. Gong, and D. R. Lee, "Electrospun nanofibers of block copolymer of trimethylene carbonate and ϵ-caprolactone," *Journal of applied polymer science,* vol. 99, no. 4, pp. 1462-1470, 2006.

[49] J. M. Gohil and P. Ray, "A review on semi-aromatic polyamide TFC membranes prepared by interfacial polymerization: Potential for water treatment and desalination," *Separation and Purification Technology,* vol. 181, pp. 159-182, 2017/06/30/ 2017, doi: https://doi.org/10.1016/j.seppur.2017.03.020.

[50] J. F. Kim, G. Szekely, M. Schaepertoens, I. B. Valtcheva, M. F. Jimenez-Solomon, and A. G. Livingston, "In Situ Solvent Recovery by Organic Solvent Nanofiltration," *ACS Sustainable Chemistry & Engineering,* vol. 2, no. 10, pp. 2371-2379, 2014/10/06 2014, doi: 10.1021/sc5004083.

[51] Z. Liu, Z. Cui, Y. Zhang, S. Qin, F. Yan, and J. Li, "Fabrication of polysulfone membrane via thermally induced phase separation process," *Materials Letters,* vol. 195, pp. 190-193, 2017.

[52] A. Figoli *et al.*, "Towards non-toxic solvents for membrane preparation: a review," *Green Chemistry,* vol. 16, no. 9, pp. 4034-4059, 2014.

[53] C.-Y. Kuo, H.-N. Lin, H.-A. Tsai, D.-M. Wang, and J.-Y. Lai, "Fabrication of a high hydrophobic PVDF membrane via nonsolvent induced phase separation," *Desalination,* vol. 233, no. 1, pp. 40-47, 2008/12/15/ 2008, doi: https://doi.org/10.1016/j.desal.2007.09.025.

[54] R. W. Baker, *Membrane technology and applications*. John Wiley & Sons, 2012.

[55] J. M. Gohil and R. R. Choudhury, "Chapter 2 - Introduction to Nanostructured and Nano-enhanced Polymeric Membranes: Preparation, Function, and Application for Water Purification," in *Nanoscale Materials in Water Purification*, S. Thomas, D. Pasquini, S.-Y. Leu, and D. A. Gopakumar Eds.: Elsevier, 2019, pp. 25-57.

[56] M. ASAEDA, L. D. DU, and K. IKEDA, "Experimental studies of dehumidification of air by an improved ceramic membrane," *Journal of chemical engineering of Japan,* vol. 19, no. 3, pp. 238-240, 1986.

[57] Y. Liu, Y. Wei, J. Su, L. Zhang, X. Cui, and L. Jin, "Surface-modified PVA/PVDF

hollow fiber composite membrane for air dehumidification," *Journal of Materials Science*, vol. 55, no. 13, pp. 5415-5430, 2020/05/01 2020, doi: 10.1007/s10853-020-04373-4.

[58] Y. Shin *et al.*, "Graphene oxide membranes with high permeability and selectivity for dehumidification of air," *Carbon*, vol. 106, pp. 164-170, 2016/09/01/ 2016, doi: https://doi.org/10.1016/j.carbon.2016.05.023.

[59] N. Tanihara, S. Nakanishi, and T. Yoshinaga, "Gas and vapor separation through polyimide membranes," *Journal of the Japan Petroleum Institute*, vol. 59, no. 6, pp. 276-282, 2016.

[60] C. Z. Liang and T.-S. Chung, "Robust thin film composite PDMS/PAN hollow fiber membranes for water vapor removal from humid air and gases," *Separation and Purification Technology*, vol. 202, pp. 345-356, 2018/08/31/ 2018, doi: https://doi.org/10.1016/j.seppur.2018.03.005.

[61] P. G. Ingole, W. K. Choi, G. B. Lee, and H. K. Lee, "Thin-film-composite hollow-fiber membranes for water vapor separation," *Desalination*, vol. 403, pp. 12-23, 2017/02/01/ 2017, doi: https://doi.org/10.1016/j.desal.2016.06.003.

[62] L.-Z. Zhang, Y.-Y. Wang, C.-L. Wang, and H. Xiang, "Synthesis and characterization of a PVA/LiCl blend membrane for air dehumidification," *Journal of Membrane Science*, vol. 308, no. 1, pp. 198-206, 2008/02/01/ 2008, doi: https://doi.org/10.1016/j.memsci.2007.09.056.

[63] Y.-R. Lee, J. Kim, and W.-S. Ahn, "Synthesis of metal-organic frameworks: A mini review," *Korean Journal of Chemical Engineering*, vol. 30, no. 9, pp. 1667-1680, 2013.

[64] O. Tanskyi, "Zeolite Membrane Water Vapor Separation for Building Air-Conditioning and Ventilation Systems," 2015.

[65] R. Xing *et al.*, "Advanced thin zeolite/metal flat sheet membrane for energy efficient air dehumidification and conditioning," *Chemical Engineering Science*, vol. 104, pp. 596-609, 2013.

[66] K.-H. Song, J.-W. Seol, S.-S. Kim, and K.-R. Lee, "Dehumidification of Air by the Hydrophilic Composite Membrane using Hydrophilic Polymer on Inorganic Substrate," (in English), *Journal of Polymer Engineering*, vol. 29, no. 1-3, pp. 15-26, 01 Mar. 2009 2009, doi: https://doi.org/10.1515/POLYENG.2009.29.1-3.15.

[67] M. I. Baig, P. G. Ingole, J.-d. Jeon, S. U. Hong, W. K. Choi, and H. K. Lee, "Water vapor transport properties of interfacially polymerized thin film nanocomposite membranes modified with graphene oxide and GO-TiO2 nanofillers," *Chemical Engineering Journal*, vol. 373, pp. 1190-1202, 2019/10/01/ 2019, doi: https://doi.org/10.1016/j.cej.2019.05.122.

[68] X. An, P. G. Ingole, W. K. Choi, H. K. Lee, S. U. Hong, and J.-D. Jeon, "Enhancement of water vapor separation using ETS-4 incorporated thin film nanocomposite membranes prepared by interfacial polymerization," *Journal of Membrane Science*, vol. 531, pp. 77-85, 2017.

[69] R. Eustache, "Poly (ether-b-amide) thermoplastic elastomers: Structure, properties, and applications," *Handbook of condensation thermoplastic elastomers*, pp. 263-281, 2006.

[70] W. Li, Z. Chang, L. Lin, and X. Xu, "Effect of montmorillonite on PEBAX® 1074-based mixed matrix membranes to be used in humidifiers in proton exchange membrane fuel cells," *e-Polymers,* vol. 20, no. 1, pp. 171-184, 2020.

[71] M. M. Rahman *et al.*, "PEBAX® with PEG functionalized POSS as nanocomposite membranes for CO2 separation," *Journal of Membrane Science,* vol. 437, pp. 286-297, 2013/06/15/ 2013, doi: https://doi.org/10.1016/j.memsci.2013.03.001.

[72] N. Azizi, T. Mohammadi, and R. Mosayebi Behbahani, "Comparison of permeability performance of PEBAX-1074/TiO2, PEBAX-1074/SiO2 and PEBAX-1074/Al2O3 nanocomposite membranes for CO2/CH4 separation," *Chemical Engineering Research and Design,* vol. 117, pp. 177-189, 2017/01/01/ 2017, doi: https://doi.org/10.1016/j.cherd.2016.10.018.

[73] R. S. Murali, A. Ismail, M. Rahman, and S. Sridhar, "Mixed matrix membranes of Pebax-1657 loaded with 4A zeolite for gaseous separations," *Separation and Purification Technology,* vol. 129, pp. 1-8, 2014.

[74] D. I. Petukhov *et al.*, "Thin graphene oxide membranes for gas dehumidification," *Journal of Membrane Science,* vol. 577, pp. 184-194, 2019/05/01/ 2019, doi: https://doi.org/10.1016/j.memsci.2019.01.041.

[75] F. H. Akhtar, M. Kumar, and K.-V. Peinemann, "Pebax® 1657/Graphene oxide composite membranes for improved water vapor separation," *Journal of membrane science,* vol. 525, pp. 187-194, 2017.

[76] D. Yang *et al.*, "Chemical analysis of graphene oxide films after heat and chemical treatments by X-ray photoelectron and Micro-Raman spectroscopy," *Carbon,* vol. 47, no. 1, pp. 145-152, 2009/01/01/ 2009, doi: https://doi.org/10.1016/j.carbon.2008.09.045.

[77] D. R. Dreyer, S. Park, C. W. Bielawski, and R. S. Ruoff, "The chemistry of graphene oxide," *Chemical society reviews,* vol. 39, no. 1, pp. 228-240, 2010.

[78] C. Schafhaeutl, "LXXXVI. On the combinations of carbon with silicon and iron, and other metals, forming the different species of cast iron, steel, and malleable iron," *The London, Edinburgh, and Dublin Philosophical Magazine and Journal of Science,* vol. 16, no. 106, pp. 570-590, 1840.

[79] Y. Zhu *et al.*, "Graphene and graphene oxide: synthesis, properties, and applications," *Advanced materials,* vol. 22, no. 35, pp. 3906-3924, 2010.

[80] B. C. Brodie, "XIII. On the atomic weight of graphite," *Philosophical Transactions of the Royal Society of London,* no. 149, pp. 249-259, 1859.

[81] L. Staudenmaier, "Verfahren zur darstellung der graphitsäure," *Berichte der deutschen chemischen Gesellschaft,* vol. 31, no. 2, pp. 1481-1487, 1898.

[82] W. S. Hummers and R. E. Offeman, "Preparation of Graphitic Oxide," *Journal of the American Chemical Society,* vol. 80, no. 6, pp. 1339-1339, 1958, doi: 10.1021/ja01539a017.

[83] D. C. Marcano *et al.*, "Improved synthesis of graphene oxide," *ACS nano,* vol. 4, no. 8, pp. 4806-4814, 2010.

[84] N. Oger, Y. F. Lin, C. Labrugère, E. Le Grognec, F. Rataboul, and F.-X. Felpin, "Practical and scalable synthesis of sulfonated graphene," *Carbon,* vol. 96, pp.

342-350, 2016.

[85] M. Brahmayya, S.-Y. Suen, and S. A. Dai, "Sulfonated graphene oxide-catalyzed N-acetylation of amines with acetonitrile under sonication," *Journal of the Taiwan Institute of Chemical Engineers,* vol. 83, pp. 174-183, 2018.

[86] M. Vinothkannan, A. R. Kim, and D. J. Yoo, "Sulfonated graphene oxide/Nafion composite membranes for high temperature and low humidity proton exchange membrane fuel cells," *RSC advances,* vol. 8, no. 14, pp. 7494-7508, 2018.

[87] Y. Kang, M. Obaid, J. Jang, M.-H. Ham, and I. S. Kim, "Novel sulfonated graphene oxide incorporated polysulfone nanocomposite membranes for enhanced-performance in ultrafiltration process," *Chemosphere,* vol. 207, pp. 581-589, 2018.

[88] L. Zhang, T. Shi, S. Wu, and H. Zhou, "Sulfonated graphene oxide: the new and effective material for synthesis of polystyrene-based nanocomposites," *Colloid and Polymer Science,* vol. 291, no. 9, pp. 2061-2068, 2013.

[89] A. A. Naser, H. Z. Al-Sawaad, and A. S. Al-Mubarak, "Novel graphene oxide functionalization by urea and thiourea, and their applications as anticorrosive agents for carbon steel alloy in acidic medium," *J. Mater. Environ. Sci.,* vol. 11, pp. 404-420, 2020.

[90] H. Zheng, M. Guo, Y. Shao, Y. Wang, B. Liu, and G. Meng, "Graphene oxide–poly(urea–formaldehyde) composites for corrosion protection of mild steel," *Corrosion Science,* vol. 139, pp. 1-12, 2018/07/15/ 2018, doi: https://doi.org/10.1016/j.corsci.2018.04.036.

[91] L. Q. Xu, W. J. Yang, K.-G. Neoh, E.-T. Kang, and G. D. Fu, "Dopamine-induced reduction and functionalization of graphene oxide nanosheets," *Macromolecules,* vol. 43, no. 20, pp. 8336-8339, 2010.

[92] L. Stobinski *et al.*, "Graphene oxide and reduced graphene oxide studied by the XRD, TEM and electron spectroscopy methods," *Journal of Electron Spectroscopy and Related Phenomena,* vol. 195, pp. 145-154, 2014/08/01/ 2014, doi: https://doi.org/10.1016/j.elspec.2014.07.003.

[93] H. Hou, X. Hu, X. Liu, W. Hu, R. Meng, and L. Li, "Sulfonated graphene oxide with improved ionic performances," *Ionics,* vol. 21, no. 7, pp. 1919-1923, 2015/07/01 2015, doi: 10.1007/s11581-014-1355-1.

[94] H. Saleem, M. Haneef, and H. Y. Abbasi, "Synthesis route of reduced graphene oxide via thermal reduction of chemically exfoliated graphene oxide," *Materials Chemistry and Physics,* vol. 204, pp. 1-7, 2018/01/15/ 2018, doi: https://doi.org/10.1016/j.matchemphys.2017.10.020.

[95] A. Monshi, M. R. Foroughi, and M. R. Monshi, "Modified Scherrer equation to estimate more accurately nano-crystallite size using XRD," *World journal of nano science and engineering,* vol. 2, no. 3, pp. 154-160, 2012.

[96] R. Al-Gaashani, A. Najjar, Y. Zakaria, S. Mansour, and M. Atieh, "XPS and structural studies of high quality graphene oxide and reduced graphene oxide prepared by different chemical oxidation methods," *Ceramics International,* vol. 45, no. 11, pp. 14439-14448, 2019.

[97] X. Zhou and Z. Liu, "A scalable, solution-phase processing route to graphene

oxide and graphene ultralarge sheets," *Chemical Communications,* vol. 46, no. 15, pp. 2611-2613, 2010.

[98] K. Krishnamoorthy, M. Veerapandian, K. Yun, and S. J. Kim, "The chemical and structural analysis of graphene oxide with different degrees of oxidation," *Carbon*, vol. 53, pp. 38-49, 2013/03/01/ 2013, doi: https://doi.org/10.1016/j.carbon.2012.10.013.

[99] M. M. A. Shirazi, D. Bastani, A. Kargari, and M. Tabatabaei, "Characterization of polymeric membranes for membrane distillation using atomic force microscopy," *Desalination and Water Treatment*, vol. 51, no. 31-33, pp. 6003-6008, 2013.